University of Coimbra

Faculty of Sciences and Technology - Department of Physics

Swept Source Optical Coherence Tomography for Small Animals - Performance Parameters and Optic Modelling

Master's Degree in Physics Engineering

André Filipe Lopes Pedrosa

September 2015

University of Coimbra

Faculty of Sciences and Technology - Department of Physics

Swept Source Optical Coherence Tomography for Small Animals - Performance Parameters and Optic Modelling

Thesis submitted for obtaining the degree of Master in Physics Engineering

Advisor:

Doctor José Paulo Pires Domingues

André Filipe Lopes Pedrosa

September 2015

Acknowledgements

First of all, I would like to express my gratitude to my advisor, Doctor José Paulo Domingues, for all the help and guidance provided, particularly, with the OCT system optical alignment and also, with the structure of this master thesis. Your availability and patience demonstrated during this project was very important for its conclusion and therefore, my sincere thanks.

Besides my adviser, I would like to acknowledge all the help provided by the Professor António Miguel Morgado, specially, for all the suggestions and encouragement given regarding the optical aspects of the system.

I would also like to thank my labmate, Susana Silva, who helped me with Zemax and gave me endless advices during this master thesis. A special thanks to my colleague, João Rodrigues, who spent many hours working with me on the OCT.

Finally, but not less important, I would like to express my deepest tanks to my parents, for all the financial effort and continuous support given, which made possible to proceed my studies. Also, to all my friends, with whom I spent six years of my life, thank you.

Abstract

Optical coherence tomography (OCT) is a non-invasive biomedical imaging technique that provides high speed and high resolution three dimensional and cross sectional images of biological samples, *in vivo*. Over the last twenty years, optical coherence tomography has experienced a fast growth, offering a wide range of applications, achieving clinical acceptance and being the focus of numerous researches. Many of these researches are related to OCT applications on small animals, whose studies have allowed the development of new medical techniques and instruments, which have improved diseases diagnosis and treatments.

In this dissertation, a review of the fundamental principles of an OCT system have been made, as well as the theoretical treatment of several OCT techniques.

After a theoretical approach to the system performance parameters, a presentation of the swept source OCT system experimental layout was performed, including a careful look to its elements.

With the presented swept source OCT system, we were able to achieve performance parameters that meet the minimum requirements to image small animals retina. A system sensitivity of $112dB$ and a roll-off performance of $3dB/mm$ combined with an axial resolution of $9\mu m$, point us to the right direction. However, special attention should be given to the system optical dispersion imbalance, in order to improve its performance.

Finally, I have conducted several optical simulations, on Zemax OpticStudio 15, where I was able to demonstrate the possibility of imaging the rat's retina with the scanning objective lenses present on the SS-OCT experimental layout. However, the image quality achieved is not on point and other elements should be studied to cancel the rat's eye spherical aberration.

Sumário

Tomografia por coerência ótica (OCT), é uma modalidade biomédica que possibilita a obtenção de imagens seccionais e tridimensionais com elevada resolução em amostras biológicas, *in vivo*, sem a necessidade de ser invasivo. A tomografia por coerência ótica foi alvo de uma rápida evolução ao longo dos últimos vinte anos, oferecendo um alargado leque de aplicações, conquistando elevada aceitação em ambiente médico e sendo o foco de um elevado número de pesquisas. Muitos dos estudos relacionados com o OCT, têm em vista, aplicações em pequenos animais que permitem testar e desenvolver novas técnicas e procedimentos que viabilizam um melhor diagnóstico e tratamento de doenças.

Nesta dissertação de mestrado foi elaborada uma revisão dos princípios de funcionamento de um sistema OCT em conjunto com o tratamento teórico de diversas técnicas OCT.

Após uma abordagem teórica aos parâmetros de performance de um sistema OCT, foi apresentada a montagem experimental final do sistema swept source OCT utilizado, incluindo a descrição dos seus componentes.

Para o sistema swept source OCT apresentado, foram alcançados parâmetros de performance que vão ao encontro dos padrões mínimos requeridos que permitem adquirir imagens da retina de pequenos animais. Uma sensibilidade de $112dB$ e um roll-off de $3dB/mm$ combinados com uma resolução axial de $9\mu m$ são indicadores da qualidade do sistema. No entanto, é essencial adotar métodos para corrigir a dispersão presente no sistema.

Por fim, foram efetuadas diversas simulações da ótica do sistema, no ambiente de programação Zemax OpticStudio 15. Estas simulações permitiram revelar a capacidade do sistema SS-OCT em obter imagens da retina do rato. No entanto, a qualidade da imagem adquirida é insatisfatória e outros elementos óticos carecem de ser estudados de forma a compensar a aberração esférica do olho do rato.

Contents

CONTENTS

List of Figures

LIST OF FIGURES

List of Tables

LIST OF TABLES

Chapter 1

Introduction

This master thesis was conducted on the Institute for Biomedical Imaging and Life Sciences (IBILI) facilities under supervision of my advisor, Doctor José Paulo Domingues.

This project arises from the previous work made by the master students, João Oliveira and José Agnelo, whose final goal was to develop a swept source optical coherence tomography system for imaging small animals retina.

Therefore, the main objectives of my master thesis were to optimize the previous SS-OCT system, in order to improve its performance parameters and also to study the ability of the OCT system to image the rat's retina with the current optical setup. The development of working skills in group and the integration in an engineering project that requires constant communication, mutual help and discussion are qualities that should be part of an engineer and than objectives to be achieved.

Optical coherence tomography (OCT) is a non-invasive biomedical technique providing high speed and high resolution three dimensional and cross sectional images of biological samples, *in vivo*. In the past twenty years, OCT has advanced to be one of the most innovative optical imaging modalities and being the subject of numerous researches, achieving great economic impact as well as clinical acceptance. It has a wide range of applications, specially, in medicine providing new equipments and procedures that allows better diseases diagnosis and treatment. Over the past year, OCT has been the focus of my work and the base subject that sustains my master thesis.

On the second and third chapters of this dissertation, the basic principles of

an OCT system were explained. Also, a mathematical treatment for the two main OCT modalities, time domain OCT and Fourier domain OCT was applied as well as the comparison of several imaging techniques. Afterwards, some of the most impactful OCT applications were discussed and compared. A theoretical treatment was applied to the SS-OCT performance parameters, where the minimum system requisites were specified and an experimental approach for its determination was suggested.

On chapter 4, a description of the final swept source OCT experimental layout was presented, including an explanation of its operation. This chapter also includes a description of all the system components, where relevant specifications were stressed.

On chapter 5 an analysis and discussion of the system performance parameter results and experimental procedures for its determination was performed. A critic analysis of the results was executed followed with methods and tests to improve and find problems affecting the current setup.

On the last chapter of this dissertation several optical simulations on Zemax OpticStudio 15 were performed. First, a brief introduction to the schematic of the rat's eye model used on the simulations was required. The followed optical simulations were performed, in order to determine the system ability to image the rat's retina. An analysis of the results was made and suggestions were presented regarding further work.

Chapter 2

Revision of Optical Coherence Tomography

Optical coherence tomography (OCT) is a non-invasive biomedical technique that provides high speed and high resolution three dimensional and cross sectional images of biological samples, *in vivo*. It has a wide range of applications specially in medical diagnosis and can perform "optical biopsy" in tissues like the eye or arteries, where standard biopsy is hazardous or impossible. OCT can still provide guidance for a wide number of medical procedures like endoscopy and several kind of surgeries.

This chapter provides an overview of OCT technology development and its applications, where a theoretical treatment is applied for better understanding of the different approaches. We also discuss the coherence property of the light and its implications in an OCT system. At the end of this chapter, several comparisons between different approaches are made, where some advantages and disadvantages are exposed.

2.1 OCT - Basics

OCT can be compared to ultrasound technique, where the principle of operation is based on time delay measurement of backscattered sound waves. However, this cannot be applied in an OCT system, because OCT is based on light, which has a much higher speed than sound waves. It is currently impossible for electronic devices, determine time delays as small as few dozens of femtoseconds. Thus, it was necessary to adopt a different approach to allow the optical path length of light measurement. Once it is not possible to directly measure the time delay of backscattered light, because of the high speed of light, an interferometric approach is required.

2.1.1 Concept of Coherence

Before we go any further, we need to understand the concept of coherence. Coherence is a property of waves that indicates the ability of waves to interfere with each other. Two waves, which are coherent, can be combined to produce an unmoving distribution of constructive and destructive interference (a visible interference pattern) depending on the relative phase of the waves at their meeting point. Waves that are incoherent, when combined produce rapidly moving areas of constructive and destructive interference and therefore do not produce a visible interference pattern. In order to obtain a good and stable interference pattern, the two beams must have nearly the same frequency. Thus, any significant frequency difference between the beams would result in a rapidly varying time dependent phase difference, which would cause the interference pattern to average to zero during the detection interval [1].

A wave can also be coherent with itself, a property known as temporal coherence. If a wave is combined with a delayed copy of itself, the duration of the delay over which it produces visible interference is known as the coherence time of the wave Δt_c. Thus, a corresponding coherence length l_c, can be estimated as:

$$l_c = c \times \Delta t_c \tag{1}$$

where c is the speed of the light wave.

We can conclude that in an interferometric approach, interference will always

occur when the optical path difference between two waves is less than the coherence length of the source. So, the coherent length can be described as a function of the light source bandwidth and can be calculated by:

$$l_c = \frac{4\ln(2)}{\pi} \cdot \frac{\lambda_0^2}{\Delta\lambda} \tag{2}$$

where $\lambda_0 = \frac{2\pi}{k_0}$ is the center wavelength of the light source and $\Delta\lambda$ is its wavelength bandwidth, defined as the FWHM (full width at half the maximum) of its wavelength spectrum [2][3].

2.1.2 Early OCT

As referred above, it was necessary to find a way to measure the optical path length of the light, in comparison to ultrasound. With this in mind, in 1971, Duguay *et al.* in their work *Ultrahigh Speed Photography of Picosecond Light Pulses and Echoes* [4], first proposed a solution to this problem. Using an experimental setup based on the Kerr effect, they were able to see through biological tissue and were the first to recognize the possible medical applications of this technique.

In 1986, Fujimoto *et al.* [5] demonstrated that femtosecond optical ranging could be applied for investigating the optical proprieties and internal structure off biological systems, as a non-invasive technique. Their experimental arrangement, where femtosecond laser pulses and non-linear optical cross correlation are applied for investigate the cornea in rabbit eyes, *in vivo*. Although reasonable axial resolution has been obtained, the sensitivity was still too short to achieve high quality images of biological systems.

We all know different kinds of tomography imaging techniques like ultrasound, X-ray and magnetic resonance, but was in November 1991 that optical coherence tomography technique was applied to obtain cross sectional images of biological tissues, for the first time, by Huang *et al.* [6].

On their work, *Optical coherence tomography* [6], they have improved the previous technique of low coherence interferometry, first applied by Fercher *et al.* [7]. Low coherence interferometry, which is based on the coherence property of light uses a low coherence light source and a reference arm. Therefore, the light that is backscattered from the sample and reference arm originates an interference signal. This signal provides information that allows different layers, from the sample, to be

distinguished. However, this technique only enables retrieve information on a single axis scan.

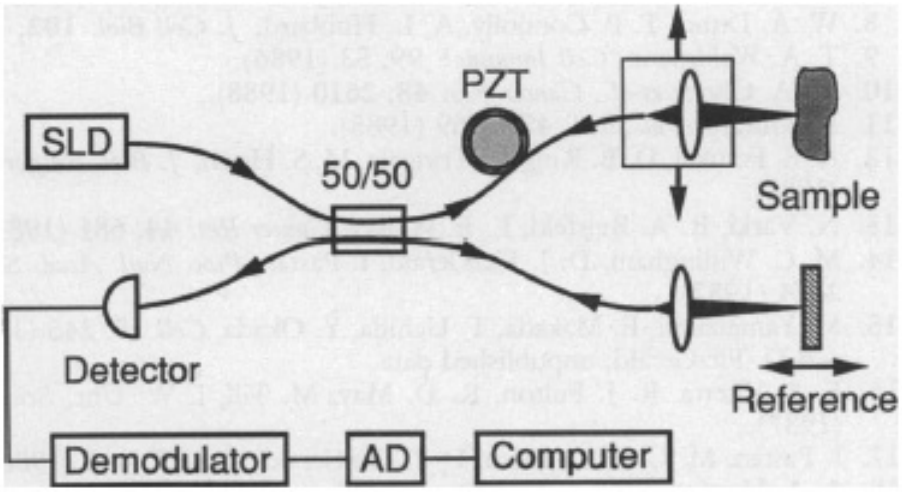

Figure 1: Schematic of the OCT scanner used by Huang *et al.* [6]. SLD - Super luminescence diode; PZT - piezoelectric transducer.

The huge improvement made by Huang *et al.* on their experimental setup, shown in figure 1 was the capability of combine multiple single axial scans into a two dimensional image, which allowed to obtain cross sectional images of a biological sample.

Thus, a basic scheme of an OCT system is based on a Michelson interferometer (figure 2), which uses a low coherence light source.

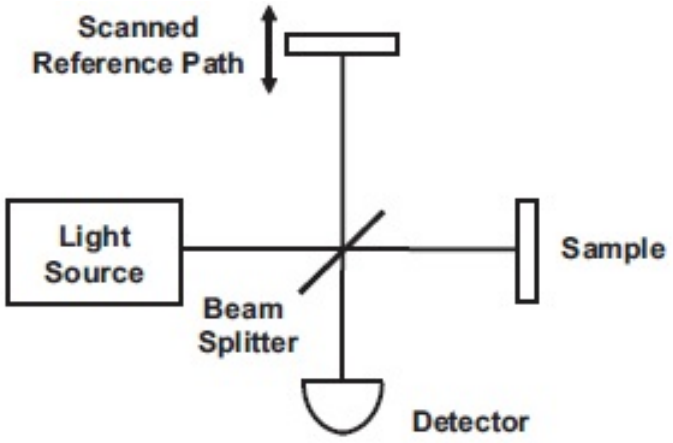

Figure 2: Scheme of an OCT system based on a Michelson interferometer [8].

The incident beam E_{in} from the light source is divided, by a beam splitter, into a reference beam E_r and a signal beam E_s. The split beam travels in a reference path, reflecting from a reference mirror, and also in a sample path where it is reflected by the sample. Thus, the interference signal E_{out} due to the recombination of the optical beams from reference and sample arms can be measured by a detector. The detector measures the intensity of the interference signal, which is proportional to the square of the total field and is given by the following equation:

$$I \sim \mid E_r \mid^2 + \mid E_s \mid^2 + 2E_r E_s \cos(2k\Delta L) \tag{3}$$

where ΔL is the path length difference between the sample and reference arms of the interferometer. As we can observe on figure 3, when low coherence light is used, interference between the optical fields is only observed when the reference and sample arm optical path lengths are matched to within the coherence length of the light. If a coherent light source is used, interference will be observed over a wide range of path length differences, which does not allow to detect the optical echoes that we are looking for.

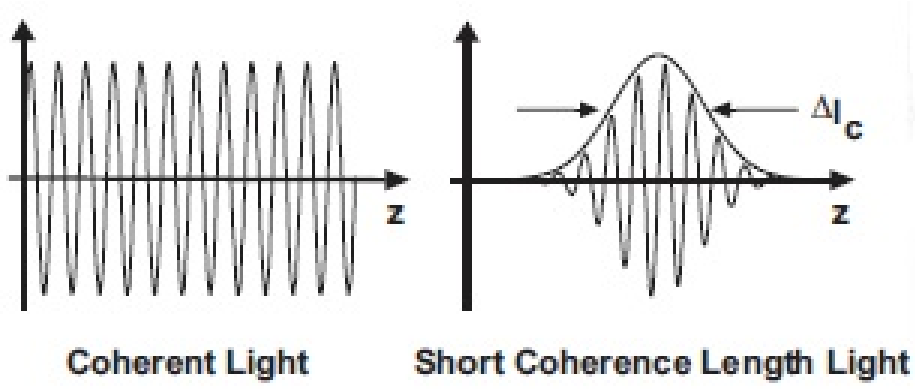

Figure 3: Interferograms of long and low coherence light length, where Δl_c is the coherence length [8].

2.1.3 Axial scan

The axial measurements of backscattered light as function of depth is the basis for OCT. So it is necessary to understand the concept of A-Scan and B-Scan. An OCT system provides an interference signal that can be displayed as cross sectional

or three dimensional images. Those images are generated by measuring the intensity and echo time delay of light. Thus, an axial scan (A-Scan) represents the intensity of the backscattered light in function of depth within the sample. Cross sectional images are generated by acquiring a series of A-Scans at different transverse positions to generate a two dimensional data set (B-Scan). Three dimensional data sets (Volume) can be created by scanning a series of B-Scans.

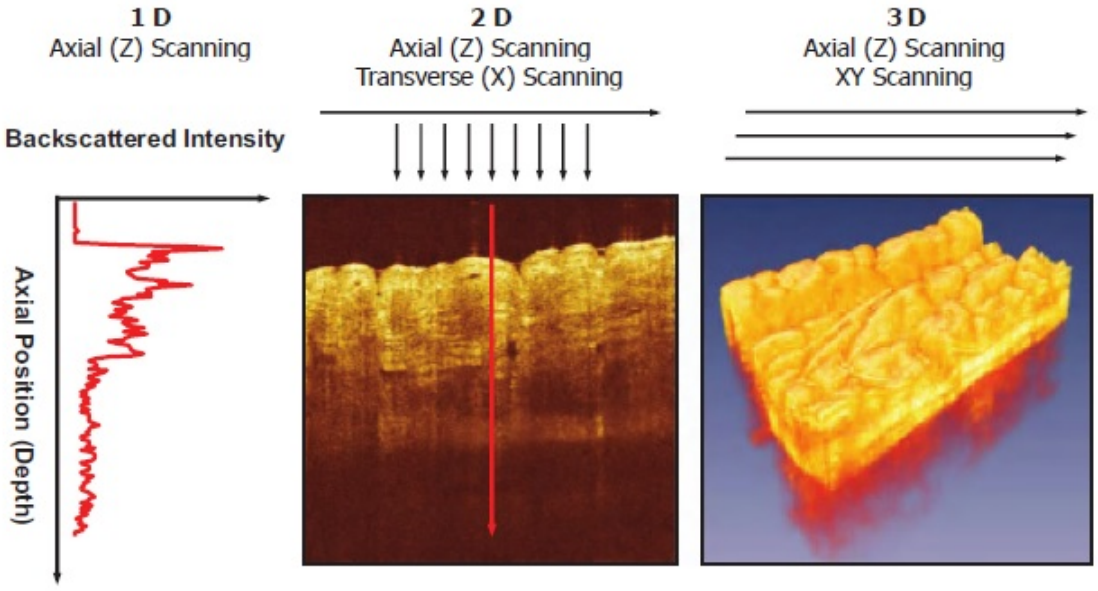

Figure 4: Illustration of an axial scan (A-scan), a two dimensional data set (B-scan) and a three dimensional data set (Volume)[8].

In order to obtain multiple A-scans from different spots in the sample, it is needed a system that changes the focus of the beam to different spots in one or two directions. Usually, a scanning galvo system is used and is represented by figure 5.

On the sample arm, the incident beam is reflected by a galvo mirror, X-scan on the figure 5, which has a fixed position during a B-scan. For each fixed position on the X-axis, the Y-scan galvo mirror moves in order to image different spots in the sample, each micro movement represents a different A-scan which is part of that specific B-scan. When a B-scan is completed, the X-scan galvo mirror moves and another Y-scan is performed. Thus, while the galvo system steps the focused beam position across the sample, multiple A-scans and B-scans are acquired and put together by the system software to generate three dimensional data sets, as shown

in figure 4.

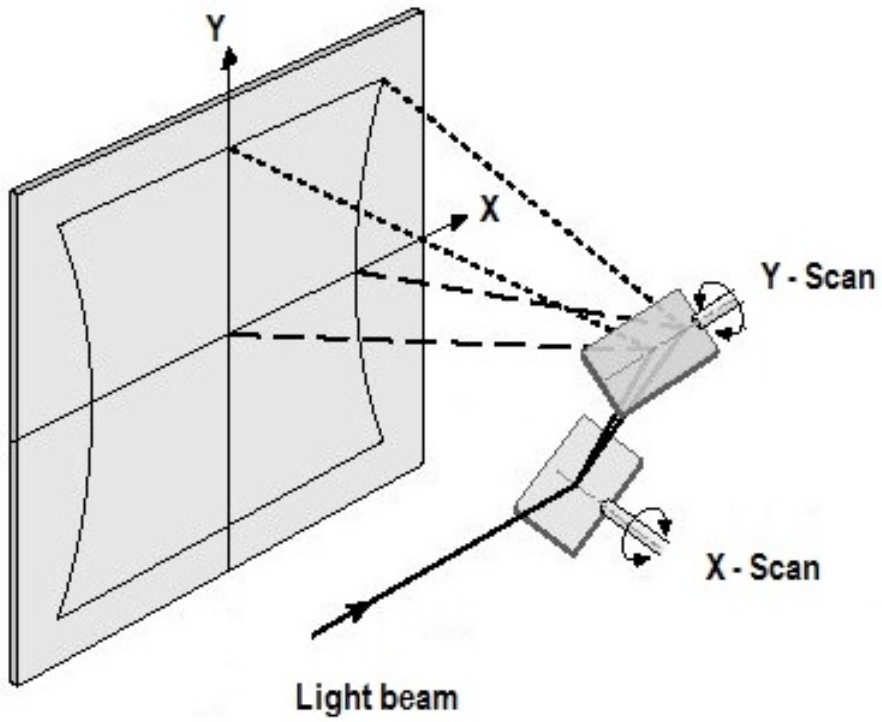

Figure 5: Scheme of a galvo system where it is shown the scanning of the sample.

2.2 Time Domain OCT

Time domain OCT (TD-OCT) is an approach that uses a broadband low coherence light source and is based on Michelson interferometer. It is very similar to what has been described, especially with the work done by Huang *et al* [6].

As discussed above, the incoming beam source of light is split into the reference path and the sample path which are recombined after the back reflection from the reference mirror and the multiple layers of the sample, respectively, to form an interference signal. The interference signal is then measured by a detector and carries information about the sample at a depth determined by the reference path length. In other words, the reference arm mirror is repetitively scanned in length changing the path length of the light, in order to observe an interference pattern that represents the light reflected from successive layers within the sample.

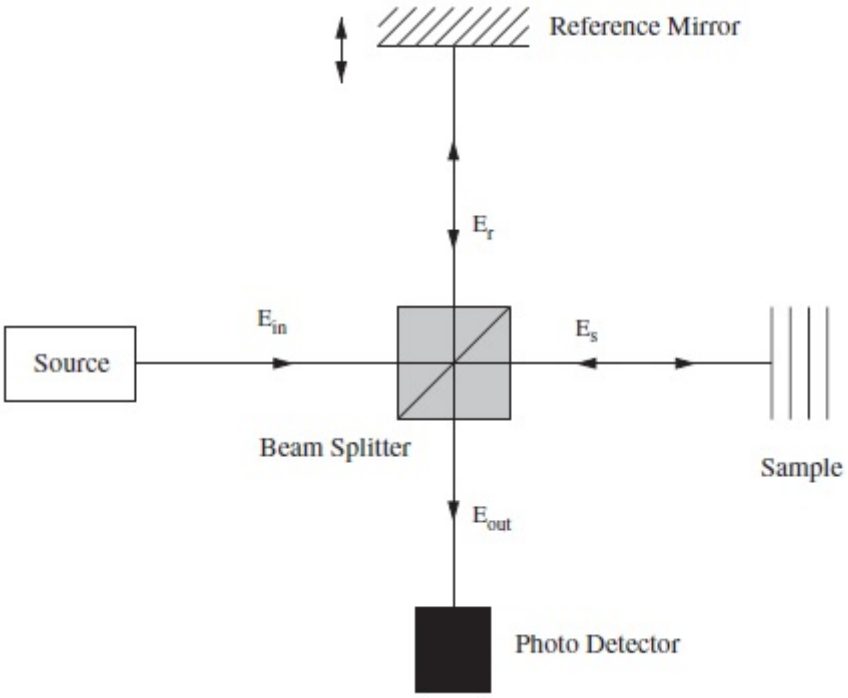

Figure 6: Basic scheme of a TD-OCT system, based on a Michelson interferometer [9].

For a better understanding of what has been described, we are going to apply a theoretical treatment to the figure 6.

The interferometer is illuminated by a light wave whose electric field can be expressed by the following equation:

$$E(w,t) = s(k,w)e^{-i(wt+kz)} \tag{4}$$

where, $s(k,w)$ is the electric field spectrum amplitude as a function of the wave number $k = \frac{2\pi}{\lambda}$ and angular frequency $w = 2\pi\nu$, which are respectively the spatial and temporal frequencies of each spectral component of the field with wavelength λ. Considering that the wavelength λ and frequency ν are related by the index of refraction of the media $n(\lambda)$ which can be expressed by $n(\lambda) = \frac{c}{\lambda\nu}$, where c is the vacuum speed of light.

As we know the beam splitter has reference and sample arm intensity transmit-

tance T_r and T_s which obey to the next relation:

$$T_r + T_s = 1 \tag{5}$$

The reference mirror have an electric field reflectivity r_r and a power reflectivity $R_r =\mid r_r \mid^2$ and the path length from the beam splitter to the reference mirror is z_r. The electric field reflectivity of the sample is treated differently, because in the sample the electric field reflectivity is depth dependent. Therefore, $r_{sn}(z_{sn})$ represents the sample reflectivity, where z_{sn} matches the path length from the beam splitter to each correspondent layer within the sample. Thus, in the sample, each layer has its own electric field reflectivity, as well as a correspondent path length. The power reflectivity is than given by $Rsn =\mid r_{sn} \mid^2$, where n represents a specific layer within the sample.

The input electric fields E_{in} is given by the equation 4 and is divided by the beam splitter into two different paths, the reference electric field E_r and the sample electric field E_s. Those electric fields are given by:

$$E_r = \sqrt{T_r T_s} r_r E_{in} e^{i2kz_r} \tag{6}$$

Note that on equation 6 the factor of two is due to interferometer setup, the light travels twice the optical path z_r.

$$E_s = \sqrt{T_r T_s} r_{sn}(z_{sn}) E_{in} e^{i2kz_{sn}} \tag{7}$$

It is now possible to express the output electric field E_{out} received by the detector which is given by the following equation:

$$E_{out} = E_r + E_s \tag{8}$$

As we know, optical detectors are squared law intensity detection devices, so the current intensity generated is given by:

$$I = \langle E_{out} \cdot E_{out}^* \rangle \tag{9}$$

Knowing that the current intensity represents a time average value, we can inte-

grate infinitesimal current intensities over small time intervals dt during the response time of the detector T, so that the equation 9 can be expressed by:

$$I = \lim_{T\to\infty} \frac{1}{2T} \int_{-T}^{T} E_{out} \cdot E_{out}^{*} dt \tag{10}$$

So, if you replace on equation 10 E_{out} and its complex conjugate from the equation 8, you should obtain the following result:

$$I_D(k) = \frac{\rho}{2} \left(\langle E_s E_s^{*} \rangle + \langle E_r E_r^{*} \rangle + 2\Re\{\langle E_s E_r^{*} \rangle\} \right) \tag{11}$$

where $\Re$ represents the real part of the cross interference term. Here, ρ is the responsivity of the detector, and the factor of two represents the loss in power due to the electric field pass two times through the beam splitter. Be aware of the similarity between this equation and the equation 3 described above.

$$I_D(k) = \frac{\rho}{2} \left[T_r T_s S(k) \sum_{n=1}^{N} R_{sn} + T_r T_s S(k) R_r + 2\Re\{\langle E_s E_r^{*} \rangle\} \right] \tag{12}$$

where $S(k) =\mid s(k) \mid^2$ and represents the power spectral dependence of the light source.

After solving the last term on equation 12, we will achieve the following equation, where three different elements can be easily distinguish.

$$\begin{aligned} I_D(k) = \frac{\rho}{2} T_r T_s S(k) \left[R_r + \sum_{n=1}^{N} R_{sn} \right] + \\ \rho T_r T_s S(k) \left[\sum_{n=1}^{N} \sqrt{R_{sn} R_r} \{\cos[2k(z_r - z_{sn})]\} \right] + \\ \rho T_r T_s S(k) \left[\sum_{n\neq m=1}^{N} \sqrt{R_{sn} R_{sm}} \{\cos[2k(z_{sn} - z_{sm})]\} \right] \end{aligned} \tag{13}$$

As referred above, on equation 13 there are three different components:

- The first one, designated as "DC term" represents the largest component of the detector current if the reference reflectivity dominates the sample reflectivity. This term is independent of the path length difference between both arms, and

scales with the light source spectrum wave number and has an amplitude that is proportional to the sum of the power reflectivity of the reference mirror and all sample layers reflectivities.

- The second term, is usually known as "cross-correlation term" component which depends of the light source wave number and the path length difference between the reference and sample arm reflectors. This component, is the desired component for OCT imaging, besides being smaller than the DC term.
- The last component, referred as "autocorrelation term" occur due to the interference between the different sample reflectors. This signal is usually not desired and can be decreased by choosing a proper reference reflectivity, so that the autocorrelation terms can be despised in comparison with the DC and cross-correlation terms. Notice that for most biological samples imaged with OCT, the sample reflectivity is usually very small when compared with the reference reflectivity. Thus, the reference signal typically dominates the reflected sample signal [8].

By knowing this, we are now able to find the detector current $I_D(k)$ for a time domain OCT system. At first, we despise the third component on equation 13 by assuming that the reference reflectivity dominates the sample reflectivities. Then, the reference mirror is continuously scanned, in order to reconstruct an approximation of the internal sample reflectivities $\sqrt{R_{ns}(z_{ns})}$. The final result is achieved by the integration of the equation 13 over all wave numbers k of the source spectrum, so that the current $I_D(k)$ is given by:

$$I_D(k) = \frac{\rho}{2} T_r T_s S_0 \left[R_r + \sum_{n=1}^{N} R_{sn} \right] + \rho T_r T_s S_0 \left[\sum_{n=1}^{N} \sqrt{R_{sn} R_r} \cdot e^{-(z_r - z_{sn})^2 \Delta k^2} \cos[2k(z_r - z_{sn})] \right] \tag{14}$$

where, $S_0 = \int_0^\infty S(k)dk$ is the spectrally integrated power emitted by the light source. From this interference signal an A-scan can be obtained and is shown on the figure below.

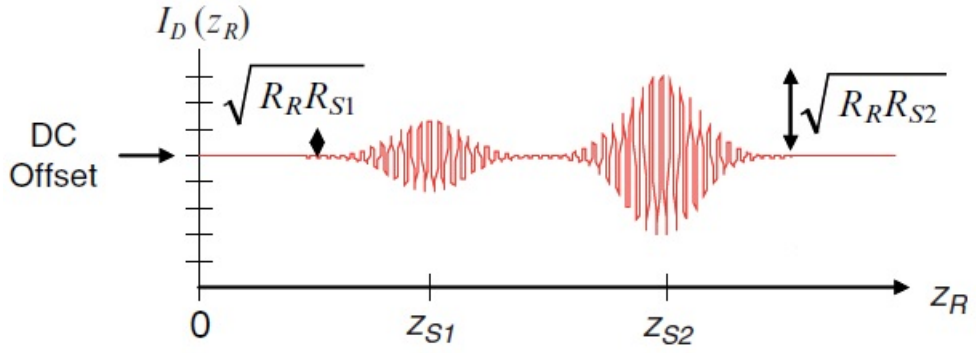

Figure 7: Representation of a time domain OCT A-scan, adapted from [8].

On the figure, we can clearly observe a DC component that results from the first term on equation 14 which is proportional to the sum of all reflectivities. The cross-correlated terms are also observed and are modulated by a wave that is proportional to the source center wave number k_0 and by the path length difference between the reference and sample arms. Note that when the optical paths are matched, by other words, when $z_r - z_{sn} = 0$ the signal intensity is at its maximum value and this happens for each of the sample layers at a distance z_{sn}.

2.3 Fourier Domain OCT

Fourier domain OCT systems are divided into two different approaches. The first approach is known as spectral OCT (SD-OCT), uses an interferometer with a low coherence light source and measures the interference signal with a spectrometer and a high speed line scan camera. The second approach is known as swept source OCT (SS-OCT or OFDI - Optical Frequency Domain Imaging) uses a interferometer with a narrow bandwidth frequency swept light source that combined with a detector is able to measure the interference signal in function of the time [8].

In Fourier domain the current generated by the detector is processed using Fourier analysis to reconstruct an approximation of the internal sample reflectivity profile $\sqrt{R_{sn}(z_{sn})}$. So, if a Gaussian shaped light source was used, its normalized Gaussian function $S(k)$ and its inverse Fourier transform $\gamma(z)$ are given by:

$$\gamma(z) = e^{-z^2\Delta k^2} \overset{FT}{\leftrightarrow} S(k) = \frac{1}{\Delta k\sqrt{\pi}} \cdot e^{-\left[\frac{k-k_0}{\Delta k}\right]^2} \tag{15}$$

where k_0 represents the central wave number of the light source spectrum and Δk its spectral bandwidth. The inverse Fourier transform of the source spectrum $\gamma(z)$ dominates the signal in an OCT system. Making use of the following Fourier transform relation $\frac{1}{2}\left[\delta(z+z_0)+\delta(z-z_0)\right] \overset{FT}{\leftrightarrow} \cos(kz_0)$ and the convolution property of Fourier transforms $x(z)\otimes y(z) \overset{FT}{\leftrightarrow} X(z)Y(z)$, and accorded to the detected current expressed by equation 13, we are able to calculate the inverse Fourier transform.

$$\begin{aligned} i_D(k) = \frac{\rho}{4}T_rT_s\gamma(z)\left[R_r+\sum_{n=1}^{N}R_{sn}\right]+ \\ \frac{\rho}{2}T_rT_s\left[\gamma(z)\otimes\sum_{n=1}^{N}\sqrt{R_{sn}R_r}(\delta(z\pm 2(z_r-z_{sn})))\right]+ \\ \frac{\rho}{2}T_rT_s\left[\gamma(z)\otimes\sum_{n\neq m=1}^{N}\sqrt{R_{sn}R_{sm}}(\delta(z\pm 2(z_{sn}-z_{sm})))\right] \end{aligned} \tag{16}$$

Once again, the desired signal term of the equation above is the cross-correlation term. So, by making use of the sifting property of the delta function $\int_{-\infty}^{\infty}\delta(t-a)f(t)dt = f(a)$ (note that $\delta(t-a)=0$ when $t\neq a$), we can obtain the final interferometric signal.

$$\begin{aligned} i_D(k) = \frac{\rho}{4}T_rT_s\gamma(z)\left[R_r+\sum_{n=1}^{N}R_{sn}\right]+ \\ \frac{\rho}{2}T_rT_s\sum_{n=1}^{N}\sqrt{R_{sn}R_r}\left[\gamma[2(z_r-z_{sn})]+\gamma[-2(z_r-z_{sn})]\right]+ \\ \frac{\rho}{2}T_rT_s\sum_{n\neq m=1}^{N}\sqrt{R_{sn}R_{sm}}\left[\gamma[2(z_{sn}-z_{sm})]+\gamma[-2(z_{sn}-z_{sm})]\right] \end{aligned} \tag{17}$$

The resulting A-scan from the interferometric signal above has at its zero position the DC term, which is related to the position of the reference reflector z_r.

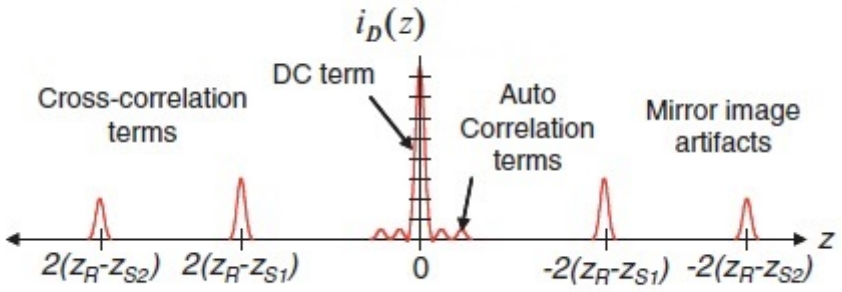

Figure 8: Illustration of the A-scan resulting from the Fourier domain low coherence interferometry in the case of two discrete reflectors [8].

The magnitude of the sample reflectivity, which is very small, is amplified by the big reference reflectivity $\sqrt{R_r}$. In the cross-correlation terms a mirror image appears on the opposite side of the zero path length (reference reflector position). These mirror images are known as the complex conjugate artifact in FD-OCT, and are related to the inverse Fourier transform of the detected interferometric signal. Thus, the positive and negative distances given by the inverse Fourier transform are complex conjugates of each other. This kind of artifact is not a big deal, because we can just display the positive distances by image processing.

Another type of image artifacts due to the auto-correlation terms appears near the DC term, because the distance between the sample reflectors is much smaller than the distance between the sample reflectors and the reference arm path length. These artifacts can be neglected by choosing a proper reference reflectivity, so that the autocorrelation term has an amplitude much smaller than the cross-correlation term [10].

2.3.1 Spectral OCT

Spectral domain OCT uses a broad bandwidth light source and a spectrometer combined with a line scan camera to measure the interference signal between the reference and sample arms. The first demonstration of retinal imaging using SD-OCT was performed by Wojtkowski *et al.* [2].

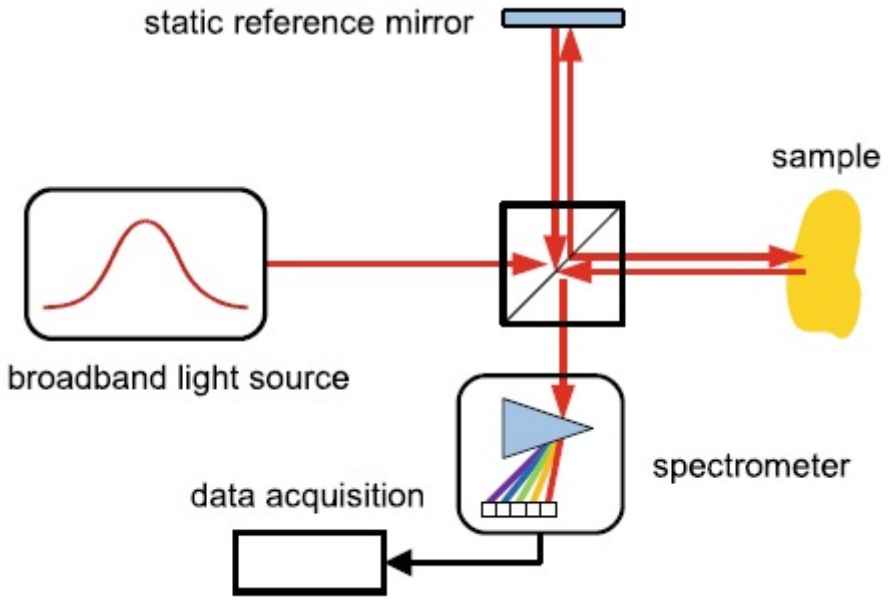

Figure 9: Schematic of a spectral domain OCT system [11].

A schematic of a spectral domain OCT system is shown on figure 9, where the beam emitted by the light source is split into two beams by a beam splitter. One beam is directed onto the sample and is reflected from different layers within the sample, at different depths. The second beam is directed onto a reference mirror that is static. The relative time delay between those two beams is determined by the optical path length difference, which is related to the depth of each layer within the sample. The interference signal measured by the spectrometer, which consists of a diffraction grating that disperses the light, an objective lens and a high speed line scan camera that simultaneously measures the different spectral components of the interference signal. The current measured by the detector is given by equation 12 and the sample profile reflectivities $\sqrt{R_{sn}(z_{sn})}$ can be reconstructed by Fourier analysis as shown on equation 17.

The interference signal has a spectral modulation that is function of frequency, which is inversely related to the echo time delay between the reference and sample beams or in other words related to the path difference Δz. Thus, different time delays will result in different frequency modulations, each one corresponding to a specific layer of the sample.

2.3.2 Swept Source OCT

Swept source OCT, is also known as optical frequency domain interferometry (OFDI). This kind of approach uses an interferometer with a narrow bandwidth light source that is frequency swept in time. SS-OCT was first demonstrated by Chinn *et al.* [12].

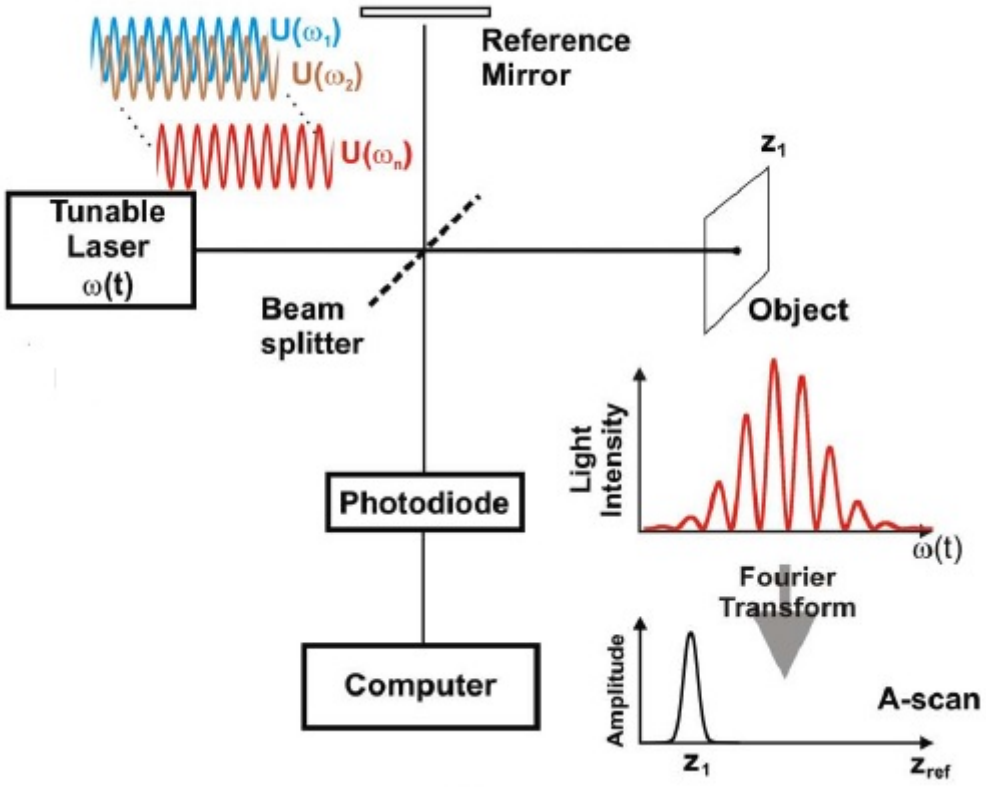

Figure 10: Schematic of a swept source OCT system where a tunable light source is illustrated [13].

In figure 10, a schematic of a swept source OCT is represented. This approach is very similar to spectral OCT however, the big difference is the light source, where the wave number of the light emitted changes repetitively within a certain range Δk, as function of time. In SD-OCT different spectral components are separated in space by the use of a spectrometer and a line scan camera, but in SS-OCT the spectral information is encoded in time. The wave number can then be written as

function of time:

$$k(t) = k_1 + \frac{\Delta k}{\Delta T} t \tag{18}$$

where k_1 is the starting wave number, Δk is the optical bandwidth source swept and ΔT is the time during an entire swept.

The interferometric signal is measured with a photo detector, where the current measured is given by equation 12, where $k(t)$ is function of time, as shown on the equation above. The interferometric term will oscillate with an angular frequency $w = \frac{\Delta k}{\Delta T} 2\Delta z$. Thus, the signal detected has a frequency that is equal to the difference frequency between the light waves from the sample and reference arms. This signal exhibits an amplitude that is proportional to the sample reflectivity profile $\sqrt{R_{sn}(z_{sn})}$, which by Fourier transformation can be decomposed in its different frequency components, each one representing light reflected by a sample layer at a specific depth.

2.4 Comparison between different OCT systems

Today, there are several different imaging techniques used in medicine such as confocal microscopy, optical coherence tomography, ultrasound, X-ray (also known as CT - computed tomography) and finally magnetic resonance imaging (MRI). As we can observe in figure 11 several imaging techniques are compared, each one with its own use for medical applications, in spite of the differences between them. The well known MRI and X-ray techniques are able to image the entire body but the image resolution cannot be compared to ultrasound, which has a good resolution combined with reasonable penetration in tissue. By another hand, confocal microscopy has the best image resolution but just can achieve a few hundred micrometers in tissue penetration. Therefore, with the arising of OCT, it was possible to fill a gap between ultrasound and confocal microscopy imaging. OCT combine a great axial resolution while is able to reach a good depth, in tissue.

Now, that we know the position of OCT in relation to the other imaging techniques, we are able to focus on comparing the different OCT systems, discussed above.

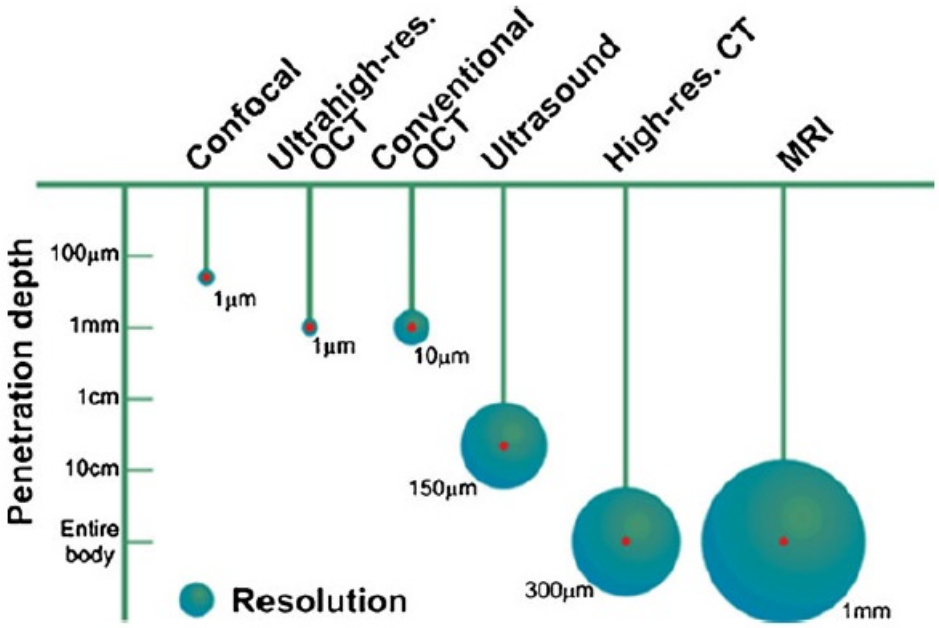

Figure 11: Comparison of image resolution and tissue penetration between several medical imaging techniques [14].

The arising of conventional OCT caused a huge impact in biomedical research, but nowadays most of the research focuses on FD-OCT, because of a great improvement in detection sensitivity and speed acquisition. Thus, acquisition speed is one of the two main advantages of Fourier domain OCT over time domain OCT and it is due to the fact that on FD-OCT the reference mirror is static, when in TD-OCT the acquisition rate is limited by the mechanical movement of the reference mirror. Hence, on Fourier domain the optical echoes are detected at the same time instead of being detected sequentially, which allows a great improvement in detection sensitivity.

Choma *et al.* demonstrated, in their work [15], the superior sensitivity of FD-OCT as compared to TD-OCT and other studies have shown that Fourier domain OCT can provide a signal to noise ratio that is more than $20dB$ better than the conventional time domain OCT [16].

In conclusion, Fourier domain detection enables OCT imaging with a $50 - 100$ times increase in speed compared to earlier OCT systems. This increase in speed is very important because it allows to increase the number of A-scans and as a

consequence improve the image quality.

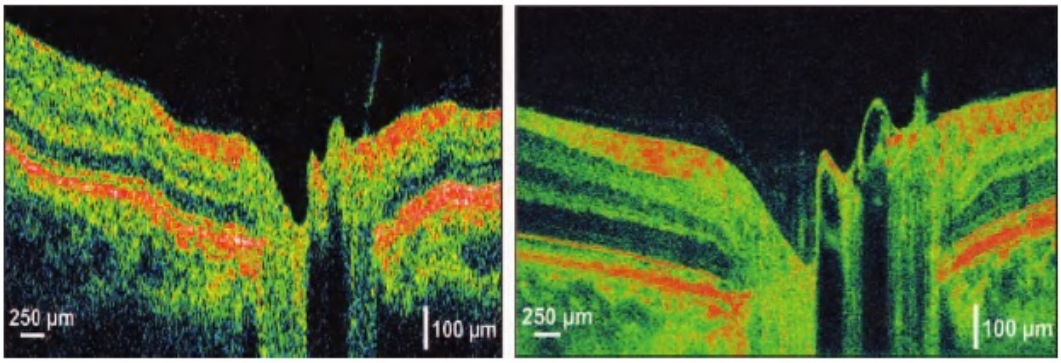

Figure 12: Spectral OCT imaging of the human retina. Comparison between a standard OCT image at left and a spectral domain OCT image at right [8].

The figure 12, illustrates a standard $10\mu m$ axial resolution human retina image with 512 axial scans acquired in $1,3s$. In comparison with an ultra-high resolution OCT image with $2\mu m$ axial resolution and 2048 axial scans, acquired in $0,13s$. This difference allowed to achieve an improved OCT image, which enables a better diagnostic of several pathologies.

Despite these advantages, FD-OCT has a disadvantage compared to TD-OCT that is the sensitivity drop-off with increasing imaging depth, which is somehow masked by the higher sensitivity achieved.

Comparing SD-OCT with SS-OCT can be a bit more challenging. Swept source OCT offers several advantages over spectral domain OCT, for example, SS-OCT has a minimal sensitivity drop-off in comparison to SD-OCT. In terms of imaging speed, it is acceptable to say that SS-OCT is in general faster, but it depends of how fast is the swept rate of the wavelength bandwidth of the light source. For SD-OCT faster spectrometers are required to achieve higher imaging speed. However, high dynamic linear detector arrays coupled with high speed data transfer electronics can be very expensive. So, with the development that has been observed according to faster laser sources swept rates, SS-OCT as the edge in terms of acquisition speed. SS-OCT has also higher detection efficiency, once there are no losses due to the spectrometer grating and still has the potential to perform dual balanced detection. Nevertheless, SS-OCT is very sensitive to parasitic reflections, since combinations of reflections at any point in the optical system can interfere to produce beat frequencies resulting

in a degradation of the signal [17].

2.5 Applications

OCT is a powerful imaging technology in biomedical research and medicine, because it enables *in vivo*, visualization of tissue structure and pathologies without the need to be intrusive.

OCT has the most clinical impact in ophthalmology, where it provides structural information that cannot be provided by any other kind of system. Thus, OCT is today a powerful tool at imaging eye structures as cornea, optic nerve, retina and crystalline lens. It is possible to make the diagnostic of ocular pathologies such as macular retinal diseases, age related macular degeneration (AMD), retinal circulation disorders, diabetic retinopathy, among others, without being intrusive. In addition to the diseases diagnosis another huge implementation of the OCT is the ability to monitoring the response to the treatment of a specific pathology.

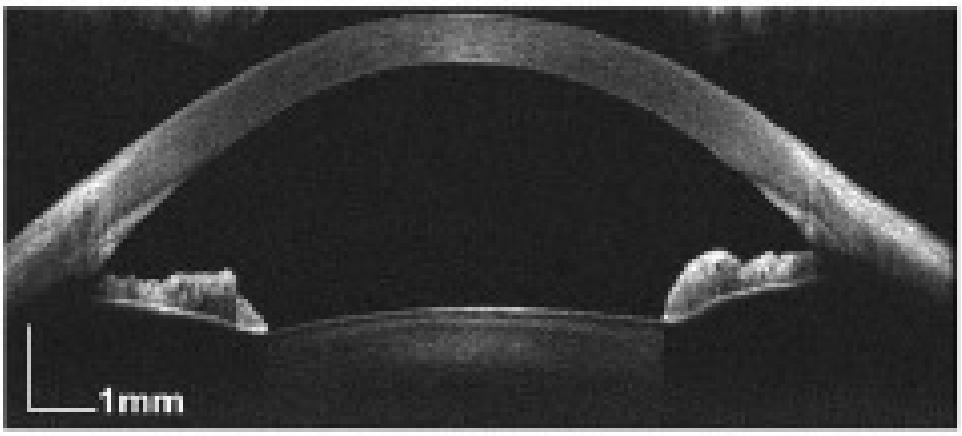

Figure 13: High quality, ultra high resolution, cross-sectional, *in vivo*, imaging of the anterior segment of the human eye, measured by a spectral domain OCT [13].

A similar application that is growing fast is cardiology, where the first commercial intra-vascular OCT system have found approval for clinical use [11]. Here, the main tasks of OCT are monitoring the response to intra-vascular interventions and provide three dimensional images that can help to understand and prevent factors associated

with heart attack episodes [13] [14].

Another field of operation is developmental biology, where the understanding of formation of functional organs requires the observation of constant changes at a cellular level. It has been demonstrated for avian embryos that is possible to keep track of different stages of development. Images of the early stages of the heart allowed the observation of morphological dynamics of its beating [13].

OCT can perform an important role in other medical fields like optical biopsy. Excisional biopsy bring problems like the risk of cancer cell spreading, infection and haemorrhage. Therefore, OCT is a viable option to perform optical biopsy with high resolution, high penetration depth and has the potential for functional imaging. Functional OCT includes the detection of polarization properties, local flow of liquid, the chemical composition or the optical and mechanical properties of the sample [11].

While OCT has a high depth resolution, the penetration depth into typical biologic samples is usually limited to a few millimetres. However, OCT is not only useful for examining the outer body surface, because, it can be interfaced with endoscope probes or subcutaneous imaging needles, which enables the imaging of internal organ systems in real time [11]. The ability to see beneath the surface of tissue, in real time can guide surgery near sensitive structures such as vessels or nerves [18].

Its wide range of current applications, from medical diagnosis and surgical guidance to the characterization of polymer micro-structures indicate that OCT will play a major role in practical scientific innovation and research in the next few years.

Chapter 3

Performance Parameters of a SS-OCT System

Optical coherence tomography is an optical technique in which the light source determines the general performance of the system. A correct choice of the light source, not only depends on the intended application, but also on the overall system performance required for that specific application. Therefore, the optical bandwidth of the light source, determines the axial resolution and the central wavelength determines the achievable penetration depth in the sample, which is limited by absorption and scattering.

This chapter provides an overview of several performance parameters of an SS-OCT system and its contribute to the achievable image quality. A theoretical treatment is applied, for better understanding of these parameters, where some standard values will be specified.

3.1 Point Spread Function

In order to understand some of the performance parameters of an OCT system, it is necessary to define the point spread function (PSF) , illustrated on figure 14. The point spread function describes the impulse response of a focused optical system. In OCT, the Fourier transformation of the signal representing a single reflection at a specific depth is the definition of PSF [19]. The determination of the PSF is a required procedure, in order to calculate several of the optical performance parameters that we will define.

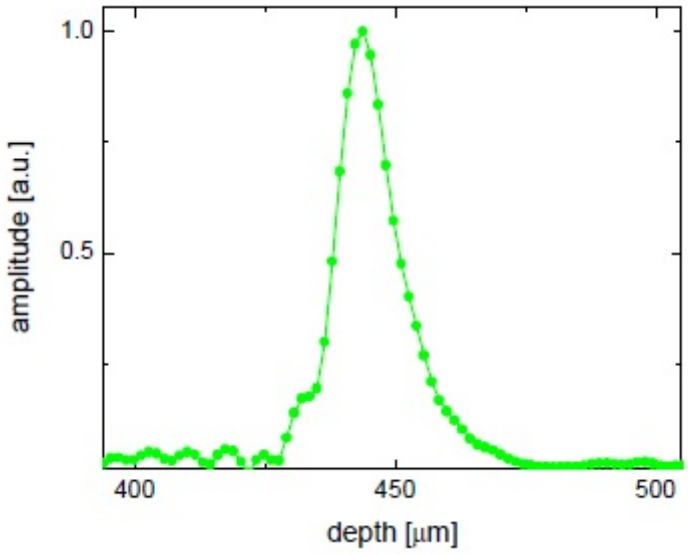

Figure 14: Illustration of a point spread function in an OCT system at a depth of $440\mu m$. Adapted from [19].

3.2 Sensitivity

Sensitivity specifies the smallest possible back reflection in the sample arm that can still be detected. Therefore, it can be defined as the minimum reflectivity R_{smin} of a sample layer whose signal can still be detected. It can also be defined as the ratio of the signal power P_0, generated by a perfectly reflecting mirror, to the minimum detectable power P_{min}, or as the ratio between the maximum current signal measured by the detector i_{Dmax} to the minimum current signal i_{Dmin} [9][13].

The system sensitivity S can then be expressed by one of the following equations:

$$S = 10 \log \left(\frac{1}{R_{smin}} \right) \tag{19}$$

$$S = 10 \log \left(\frac{P_0}{P_{min}} \right) \tag{20}$$

$$S = 20 \log \left(\frac{i_{Dmax}}{i_{Dmin}} \right) \tag{21}$$

We can measure the sensitivity of an OCT system by placing a mirror in the sample arm, and determine the PSF at a point where the optical path lengths are matched ($\Delta z \sim 0$). Once it is not possible to distinguish the minimum sample signal from the background noise of the system, it is currently accepted that this transition occurs when the signal to noise ratio (SNR) equals one. So, when $SNR = 1$, the mean square of the signal power equals the variance of the background noise σ^2_{noise} and the minimum current measured by the detector follows the next equation:

$$i_{Dmin} = \sqrt{\sigma^2_{noise}} = \sigma_{noise} \tag{22}$$

Now, we have tools to determine the sensitivity of the system, replacing on equation 21, i_{Dmax}, by the calculated PSF maximum value and substituting i_{Dmin} by the result obtained on equation 22. It is important to notice that the value of variance should be calculated after Fourier transform of the background noise signal. In order to determine σ^2_{noise} it is necessary to block the light from reaching the sample mirror. It is also essential to measure both PSF maximum peak and the variance of the background noise separately.

Obviously, the noise in OCT limits the sensitivity and to have good image quality, in biomedical applications, the sensitivity should be above $90dB$ [3][11][20]. This is required to make up for the low power reflectivities of the sample layers.

As already mentioned on the last chapter, the roll-off performance, only relevant for Fourier domain OCT, determines the decrease in the OCT signal strength at increasing depth. Therefore, in FD-OCT, the sensitivity fall-off with the depth and can be specified by the R-number, which is usually represented in dB/mm. The roll-off performance can be measured in a similar way as the measurement of sensitivity.

Basically, we successively measure the sensitivity for different depth positions $S(\Delta z)$. The R-number can then be obtained by estimating the slope of a linear fit to the maximum peak of each PSF, as shown in the figure 15.

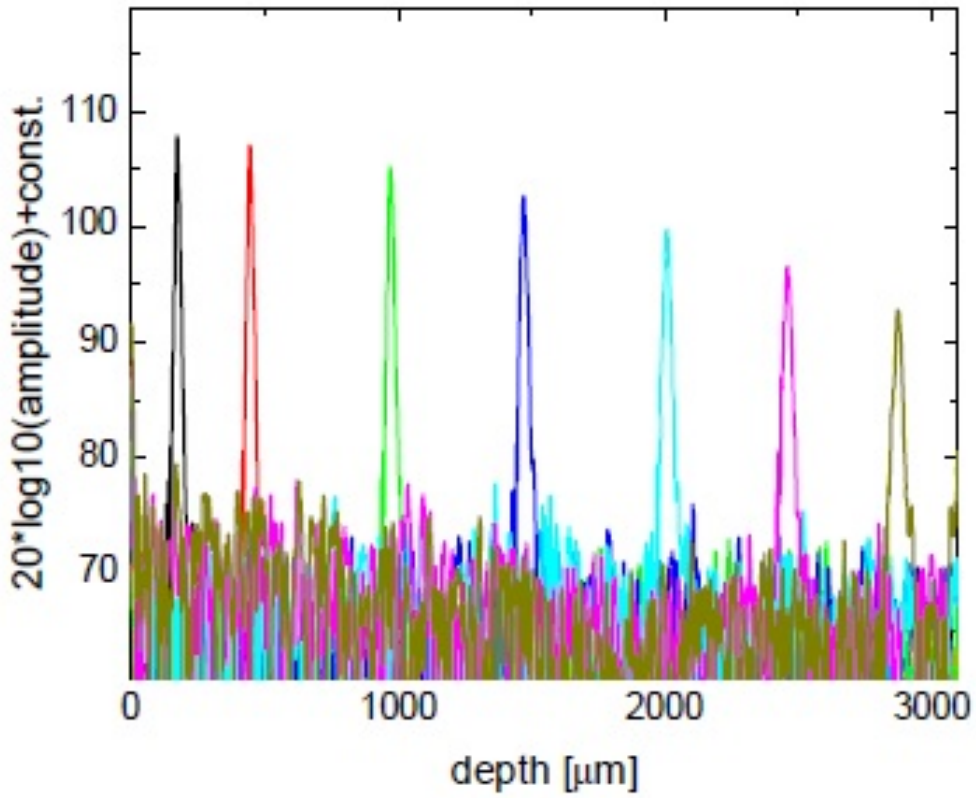

Figure 15: Measurement of several PSFs at different depths, which shows the sensitivity roll-off of a SS-OCT system [19].

A good OCT system should be able to have a roll-off, or R-number, below 10 dB/mm [20][21]. The sensitivity roll-off in a SS-OCT system is caused by the finite instantaneous linewidth of the light emitted by the tunable laser [13].

3.3 Dynamic Range

The dynamic range is the ratio in signal strength between the strongest and weakest reflection which can be measured simultaneously, within one A-scan. The measurement of dynamic range is performed similarly to a sensitivity measurement.

The real difference is that the measurement is performed at the same time instead of separately. This can be clearly understood by observing the next figure.

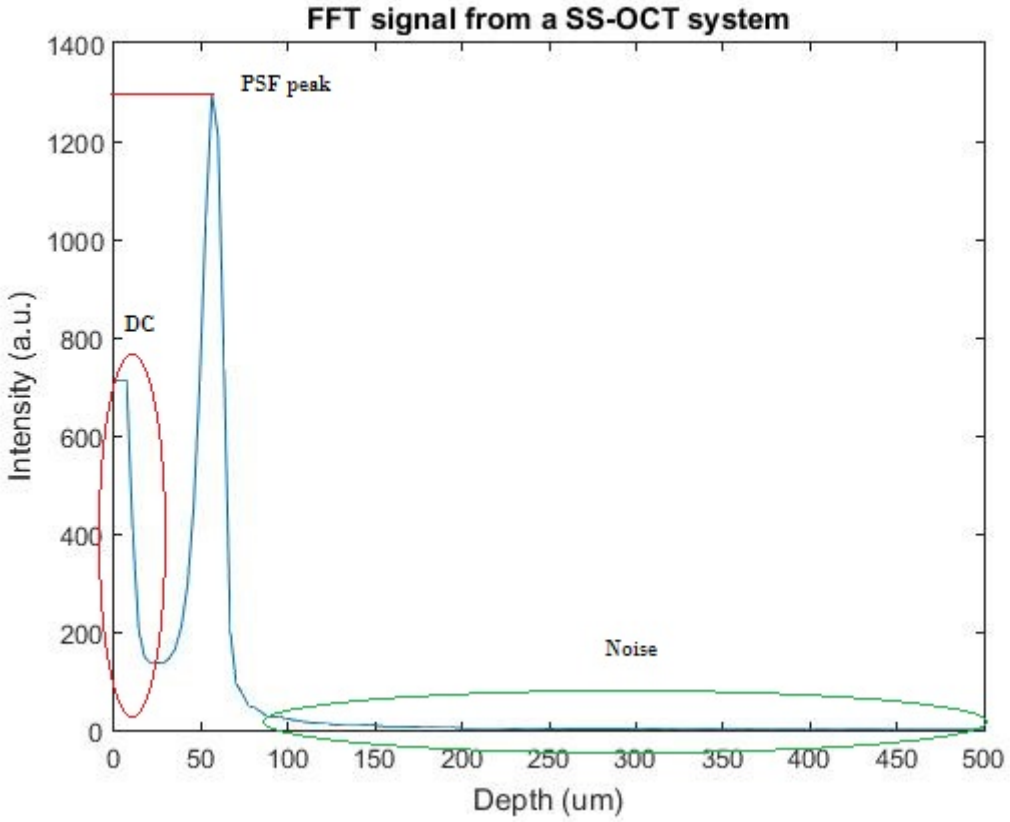

Figure 16: Measurement of a PSF, where a mirror is placed at the sample arm, corresponding to a depth of nearly $60\mu m$.

In figure 16, it is represented a PSF of a SS-OCT system, which allows to measure the dynamic range of the system. As we can observe, it is possible to measure the peak signal and calculate the variance of the background noise $\sigma^2_{noisePSF}$, after the PSF peak. The dynamic range D can be calculated based on equation 23 and on the graphic of figure 16. It results in a reduction of the magnitude compared to the sensitivity.

$$D = 20\log(\frac{i_{Dmax}}{\sigma_{noisePSF}}) \tag{23}$$

To guarantee enough image quality, an OCT system should have a dynamic range values above $40dB$ [22].

3.4 Axial Resolution

Axial resolution is one of the most important parameters of an OCT system, because in many biomedical applications, high axial resolutions are required in order to distinguish different cellular layers.

The axial resolution in FD-OCT is linked to the light source spectrum (equation 15) and is determined by the coherence length of the light source (see equation 2) [2][9][13]. In the case of the Gaussian shape of the coherence function and also keeping in mind that the light travels back and forth in the interferometer, the axial resolution is expressed by the formula [9]:

$$\delta z = \frac{l_c}{2} = \frac{2\ln(2)}{\pi}\frac{\lambda_0^2}{\Delta\lambda} \tag{24}$$

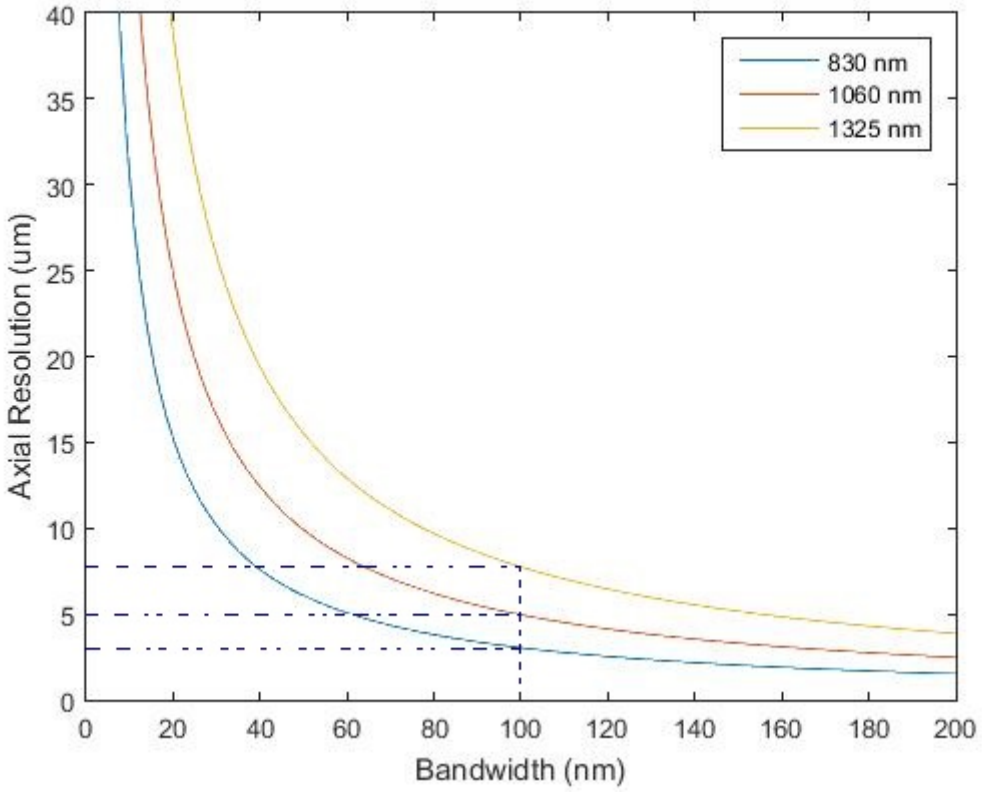

Figure 17: Axial resolution of an OCT system as function of the center wavelength and the bandwidth of the light source.

The axial resolution achieved is assumed to be on air, because in a medium of refractive index n, the resolution becomes $\frac{\delta z}{n}$. Thus, the effective axial resolution in tissue is usually smaller, since its index of refraction is higher [14]. For biomedical applications, the recommended value of axial resolution should be below $10\mu m$, on air [11].

As expected from equation 24 and figure 17 analysis, the axial resolution increases with higher center wavelengths and on the other hand decreases with wider bandwidths of the light source.

3.5 Lateral Resolution

The lateral or transversal resolution in optical coherence tomography imaging is determined by the focusing properties of the optical beam. The minimum spot size to which an optical beam can be focused is inversely proportional to the numerical aperture [14][18]. The lateral resolution δx is given by [14]:

$$\delta x = \frac{4\lambda_0}{\pi}\frac{f}{d} = \frac{2\lambda_0}{\pi NA} \tag{25}$$

where d is the entrance pupil diameter of the scanning objective lens, f is its focal length and $NA = \frac{d}{2f}$ its numerical aperture. High lateral resolution can be obtained by using high numerical aperture optics and focusing the beam to a small spot size. In addiction, the lateral resolution is also related to the depth of focus (DOF) [14][18], which is given by:

$$DOF = \frac{\pi \delta x^2}{2\lambda_0} = \frac{2\lambda_0}{NA^2} \tag{26}$$

Thus, increasing the lateral resolution results in the depth of focus decrement.

One of the advantages of OCT is that the lateral resolution is not related to the axial resolution. Therefore, the optical system can be optimized in order to improve lateral resolution without effect on the axial resolution. However, by increasing the lateral resolution, maximum depth penetration is lost. Hence, equilibrium between maximum penetration and lateral resolution has to be found [9], as you can observe on figure 18.

In most OCT applications designed for practical clinical and research applica-

tions, relatively low numerical aperture objective is used, so that the lateral resolution is approximately matched to the axial resolution, and thus approximately isotropic resolution imaging is performed [8]. The aim of OCT is to image over the maximum possible depth range that is why low numerical aperture lens are used.

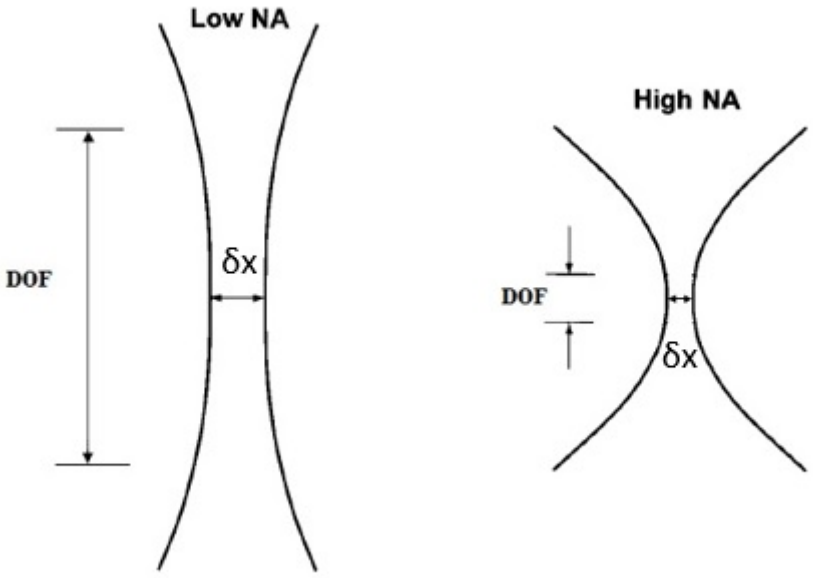

Figure 18: Schematic of both low and high numerical aperture focusing lens. Relationship between lateral resolution δx and depth of field DOF. Adapted from [18].

3.6 Noise Contributions

The optical detection in OCT has three significant sources of noise: shot noise, thermal noise and excess photon noise [9].

Shot noise arises from current fluctuations, due to the quantization of light. A photo detector will emit charge corresponding to a mean rate defined by the photo current. However, the arrival time between specific emissions will be random thus, photon arrival and electron emission times are described by a Poisson distribution [18]. An event that follows a Poisson distribution has a standard deviation proportional to the square root of the average number of photons arriving the detector, per unit of time, $\sigma = \sqrt{N}$. Each photon produces an electron with an efficiency η, which

is the efficiency of the detector. During the time interval T, the average number of electrons produced is ηN. Each electron contributes to the current I with a charge $e = 1,602 \times 10^{-19} C$, and the average signal current is given by:

$$I_n = \frac{e}{T}\eta N \tag{27}$$

Thus, fluctuations in the number of photons generates fluctuations in the signal current. These fluctuations can be described by its variance:

$$\sigma^2 = \frac{e^2}{T^2}\eta N \tag{28}$$

Knowing that the bandwidth of the detector is given by $\Delta f = \frac{1}{2T}$ and using equations 27 - 28, we have:

$$\sigma^2 = 2\Delta f e I_n \tag{29}$$

Thus, the shot noise can be expressed by the standard deviation :

$$\sigma_{shot} = \sqrt{2\Delta f e I_n} \tag{30}$$

Thermal noise arises from random particle motion due to the thermal energy of a system. Thermal noise is usually associated with the transfer of the energy and the temperature equilibrium established between a resistor and its surroundings [18]. There are some derivations for estimation of thermal noise from the shot noise calculation. Hence, the thermal noise is given by the following equation:

$$\sigma_{thermal} = \sqrt{\frac{4K_B T_0 \Delta f}{R_L}} \tag{31}$$

where K_B is the Boltzmann constant, T_0 is the temperature and R_L represents the load resistance.

Excess photon noise, also called intensity noise, describes the beating between the constituent frequencies of the source spectrum. Excess photon noise is sometimes called relative intensity noise (RIN), which is a wrong assumption. This happens because excess photon noise is one order of magnitude higher than the shot and thermal noise together [23]. Excess photon noise refers to the noise from spontaneous beating between different spectral components with random phase. Excess photon

noise for a purely spontaneous source is given by:

$$\sigma_{exc} = \sqrt{\frac{(1+\alpha)^2 I_n^2 \Delta f}{\Delta \nu}} \tag{32}$$

where α is the degree of polarization, and $\Delta\nu$ is the spectral bandwidth of the source [18].

The relative intensity noise consists of all three noise terms, shot noise, thermal noise and excess photon noise and can be represented by:

$$RIN = \frac{\sigma_{shot}^2 + \sigma_{thermal}^2 + \sigma_{exc}^2}{I_n^2 \Delta f} \tag{33}$$

RIN represents the total amount of photon noise, per unit of bandwidth, and is one of the most significant factors limiting the sensitivity of an OCT system [18].

Chapter 4

Swept Source OCT System

On this chapter, we will focus on the description of the swept source OCT system used on this master thesis.

The description of all SS-OCT components will be made here, where several characteristics are emphasized regarding its importance on the imaging system.

4.1 Experimental Arrangement

On the last chapter, the basic principles of a SS-OCT system were explained and now it is time to apply those principles. Thus, the experimental setup used on this master thesis is represented on figure 19 and a photo is shown on figure 21, where several components are identified.

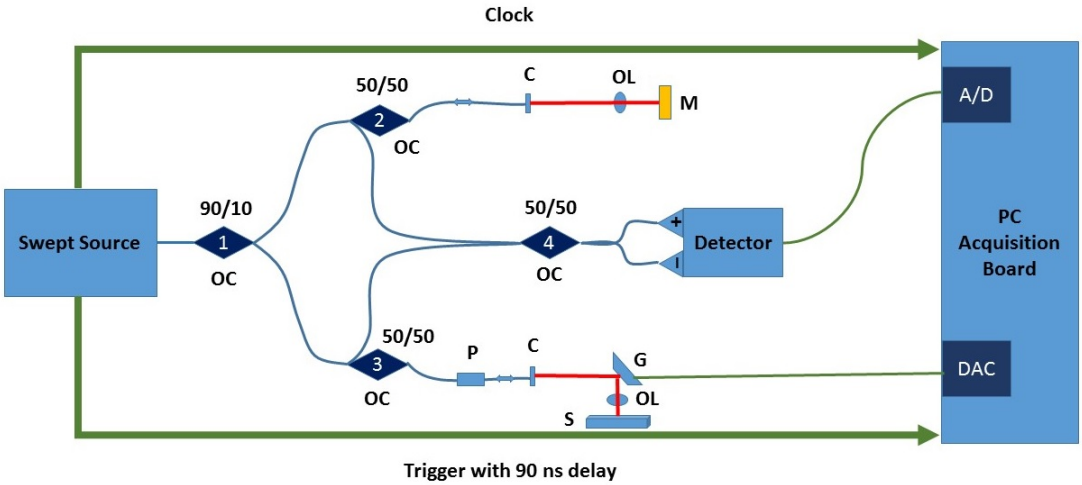

Figure 19: Schematic of the swept source OCT system used on this thesis. OC - Fiber Optic Coupler; C - Fixed Focus Collimator; OL - Scanning Objective Lens; M - Gold Mirror; P - Optical Fiber Polarization Controller; G - Galvanometer; S - Sample;

The experimental setup represented above is based on the Michelson interferometer and uses fiber optic components in order to guide the light through the system. Light from the swept source passes through a 90 : 10 fiber optic coupler (OC-1), which splits the light onto two different paths, the reference and sample path. Hence, 90% of the light goes to the sample path and the remaining 10% goes to the reference path. However, before the light reaches the reference and sample arms (figure 20), it passes through another fiber optic coupler, OC-2 and OC-3, respectively. These fiber optic couplers have a different function from the first one, they work as circulators.

On the reference path, the light enters the optic coupler OC-2 and is directed onto the reference arm, where it is collimated by a fixed focus collimator (C) and focused by an objective lens (OL) on a mirror (M), where the light is reflected. The

back-reflected light is then received by the collimator and redirected into the optic coupler OC-2, where the back-reflected light is then directed to the optic coupler OC-4.

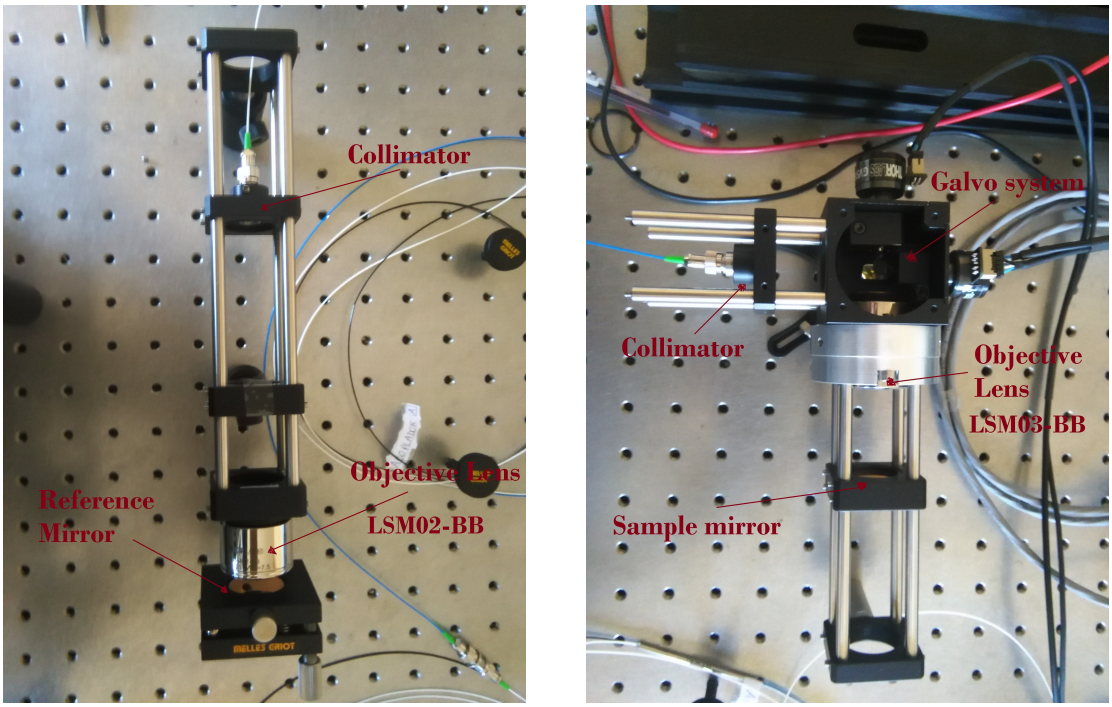

(a) Reference arm, using a scanning objective lens $LSM02 - BB$.

(b) Sample arm, using a scanning objective lens $LSM03 - BB$.

Figure 20: Picture of the reference and sample arm of the SS-OCT system used, with the identification of all the components.

On the reference arm, the position of the collimator can be adjustable to match the path length difference between both arms.

A similar approach was taken on the sample path. The light exiting the optic coupler OC-3, is directed onto the reference arm, after passing through a polarization controller (P). The collimated light is then reflected and directed, by a galvanometer (G), into the sample, after being focused by the objective lens $LSM03 - BB$. The back-reflected light from the sample is then redirected into the optic coupler OC-3 and then directed to the optic coupler OC-4.

You should be aware that for most of the tests performed with the presented SS-OCT system, the sample is usually a mirror with the same reflectivity properties of the mirror used on the reference arm.

As mentioned above, the optic couplers OC-2 and OC-3 work as circulators however, they are still 50 : 50 couplers. Thereby, the light is attenuated by 50% each time it passes through the optic coupler. In both cases, the light passes twice by the respective coupler, which means that only 25% of the light from each arm is directed onto the optic coupler OC-4. In turn, this coupler works as an interferometer and is here that interference signal is formed and directed into a balanced detector. The detected signal is digitalized by an acquisition board, which also receives an external clock from the source. The data is then processed by a custom software on a computer and displayed for further analysis. The final experiment arrangement can be observed on the figure below.

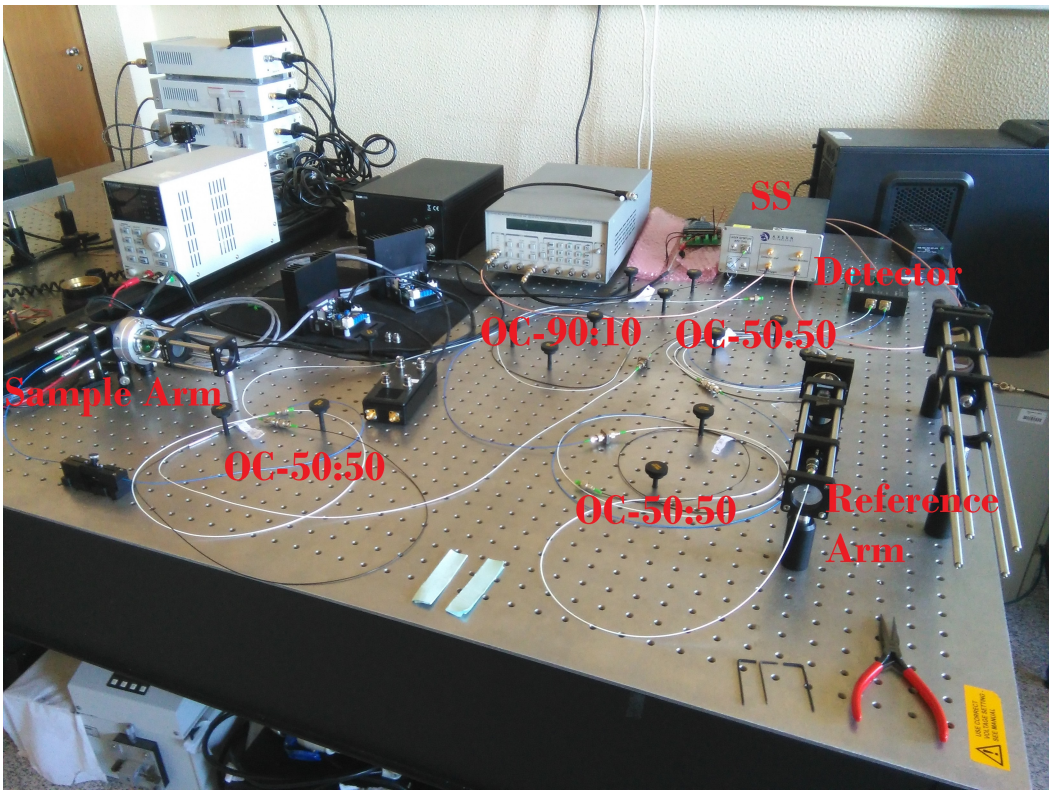

Figure 21: Photo of the final experimental arrangement of the SS-OCT used on this thesis.

4.1.1 Swept Source

A swept laser source, is a kind of light source, in which the output wavelength of the light is continuously changed, within a specific wavelength range, as function

of time [10]. As can be seen in figure 22, within a specific wavelength range, a pulse of light with a narrow linewidth $\delta\lambda$, is emitted as function of time.

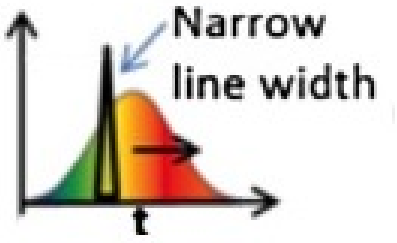

Figure 22: Illustration of a narrow linewidth pulse from a swept source with a bandwidth $\Delta\lambda$. Adapted from [10].

Note that the swept source is able to sweep its bandwidth front to back (forward sweep) and back to front (backward sweep) [10].

The swept source used in this project is Axsun high speed $1060nm$ swept source engine for OCT, model SSOCT-1060 from the AXSUN Technologies Inc., Massachusetts, USA.

The laser engine consists on AXSUN Technologies' optical integration platform and patented MEMS (micro-electromechanical system) tunable optical filter [10] [24] [25]. Its main specifications include:

- Wavelength range between $980 - 1100nm$;
- Central wavelength at $1060nm$;
- Average output power of at least $15mW$;
- Laser swept speed between $10 - 100kHz$ however, the source operates at a fixed swept rate, within this range of frequencies;
- Coherence length at least $10mm$;

In figure 23, we are able to observe a graphic of the time average spectral output power of the swept source engine. The wavelength sweep range is approximately $110nm$, starting at $985nm$ to $1095nm$, operating at a sweep speed of $100kHz$, which corresponds to $10\mu s$ sweep time. Within this range, it is able to take 1376 samples

in a maximum of 1510, corresponding to nearly 91% of the considered bandwidth. Therefore, each pulse emitted by the light source has an instantaneous linewidth equal to:

$$\delta\lambda = \frac{\Delta\lambda}{Npoints} = \frac{110nm}{1376} = 79.94pm \tag{34}$$

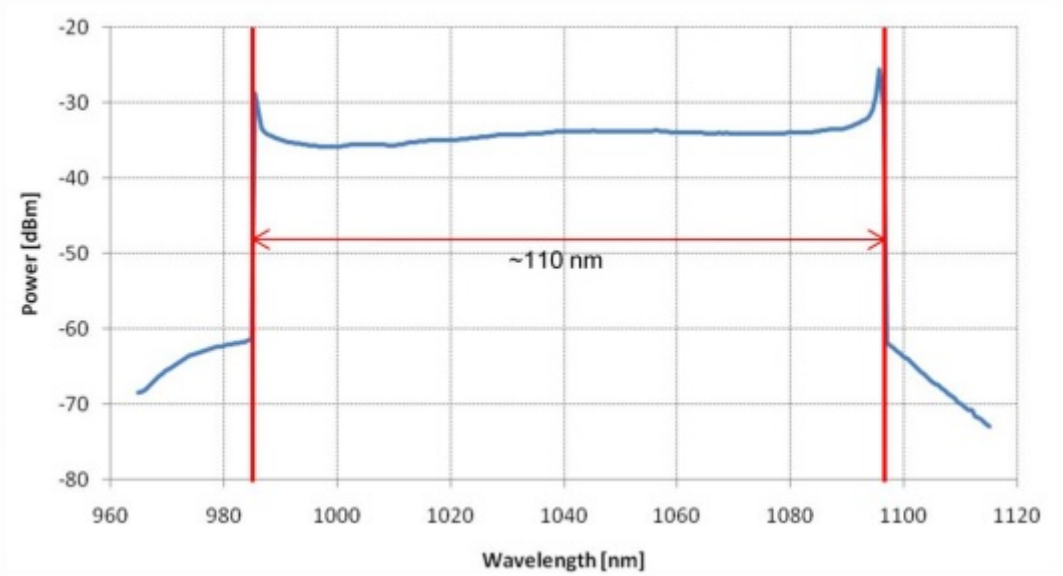

Figure 23: Graphical representation of the time average spectral output power of Axsun swept source engine [24].

The trigger signal that comes from the swept source is used to synchronize the data acquisition with the beginning of the wavelength swept. However, this trigger is modified by a digital delay of $90ns$, in order to compensate the difference in time between the clock signal and the trigger. The clock oscillates at a mean rate of $310MHz$, but its clock rate is not constant, it has a typical variation of nearly 20% [24].

On figures 24 and 25, are shown the trigger and clock signals generated by the swept source, as well as the interference signal obtained from our SS-OCT system. As said above, the source swept time is synchronized by the trigger which has a duration of $10\mu s$, as we can observe on figure 24. The trigger activates the source clock, which can be divided in two distinct phases, an optical clock and a dummy clock. The optical clock is the clock generated when the laser is ON and it corresponds to

$4.45\mu s$ of the sweep time. The remaining sweep time is related to the dummy clock, which is generated when the laser is OFF, and it can be clearly observed on figure 25. In conclusion, the trigger, the clock signal and the data acquisition are perfectly synchronized.

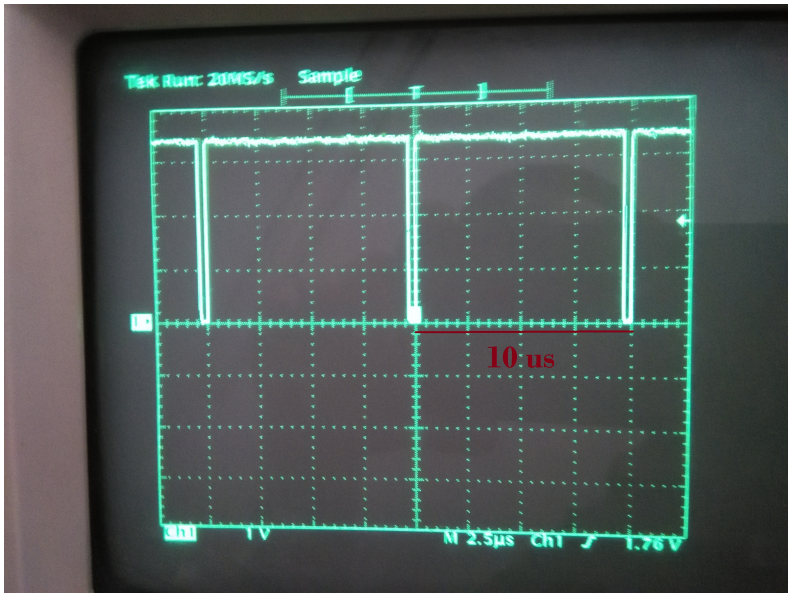

Figure 24: Swept Source trigger signal, represented on an oscilloscope.

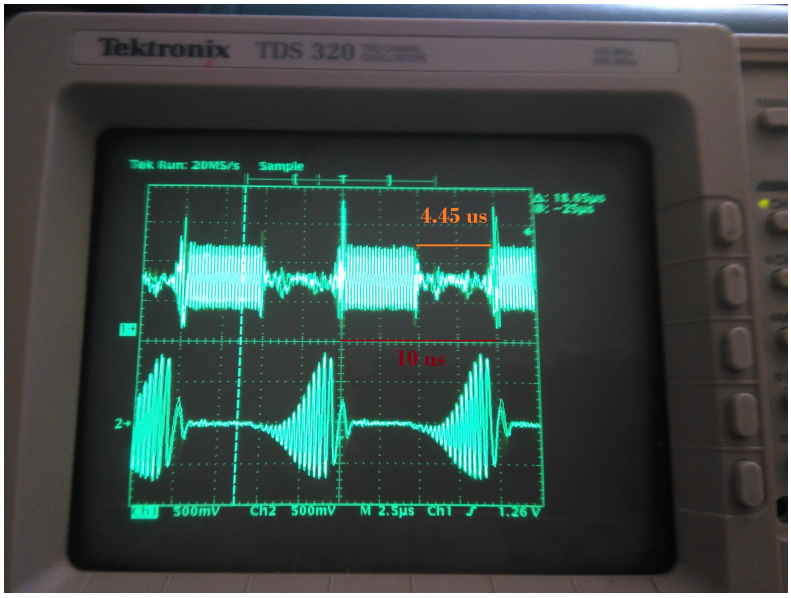

Figure 25: Swept Source clock signal (top) and SS-OCT interference signal acquired by the detector (bottom), represented on an oscilloscope.

As already mentioned on the last chapters, the light source, in an OCT application, is a key component and is important to focus a bit on its central wavelength. When imaging biological samples, there are two main processes that are wavelength dependent: absorption of photons by the sample and scattering. On near-infrared (NIR) region ($600-1500nm$) water absorption becomes the most important parameter (50% absorbed light at $1060nm$) [13]. The swept source chosen for this project has a central wavelength of $1060nm$, which allows higher tissue penetration at the cost of a loss of axial resolution [13]. Knowing that we intend to image small animals retina, it seems to be an adequate choice.

4.1.2 Single Mode Fused Fiber Optic Coupler

A fiber optic coupler is a device generally used in optical fiber systems. Light entering an input fiber can appear at one or more outputs with a specific power distribution. A 2×2 fused fiber optic couplers (figure 26) are usually used as beam splitters or to mix two light beams with minimal power loss [26].

On the experimental arrangement, four 2×2 single mode fused fiber optic couplers were used:

- three Thorlabs FC 1064-50B-APC couplers, with $50:50$ split ratio and central wavelength of $1064 \pm 15nm$;
- one Thorlabs FC 1064-90B-APC coupler, with $90:10$ split ratio and central wavelength of $1064 \pm 15nm$;

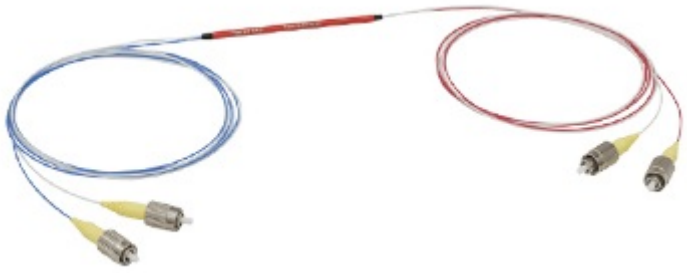

Figure 26: Picture of a 2×2 single mode fused fiber optic coupler used on the experimental setup. Adapted from [26].

On figure 27, it is represented a schematic of a 50 : 50 fiber optical coupler, when used as beam splitter. The light enters on input A, in this situation input B must be closed, and its power is divided equally between output C and D, because it has 50 : 50 split ratio. On the final experimental setup, shown on figure 19, this type of configuration is performed by the coupler OC-1.

Figure 27: Schematic of a 50:50 split ratio fiber optic coupler, used as beam splitter. Adapted from [26].

A different application for the fiber optical coupler, is shown on figure 28. In this configuration the coupler works as an interferometer and is represented by the coupler OC-4, on the experimental setup (figure 19). The light enters on inputs A and B and exits the output C and D with a power that is dependent of the split ratio of the coupler. For instance, the light power at the output C is composed by $0.9 \times B + 0.1 \times A$.

Figure 28: Schematic of a 90:10 split ratio fiber optic coupler, used as interferometer. Adapted from [26].

The last configuration used on our experimental setup is when the fiber optic coupler works as a circulator, like the couplers OC-2 and OC-3 (figure 19). A

schematic of this kind of implementation is shown on figure 29. Light enters input A and is divided between both output ports, however one of them must be closed (D). Light exiting output C is then reflected by the reference mirror or sample, and is redirected into the output C. Light is divided once again, and exits the inputs A and B, being the input B the required port. Note that the power on port $B = 0.5 \times C$, is just 25% of the initial power, for this specific situation.

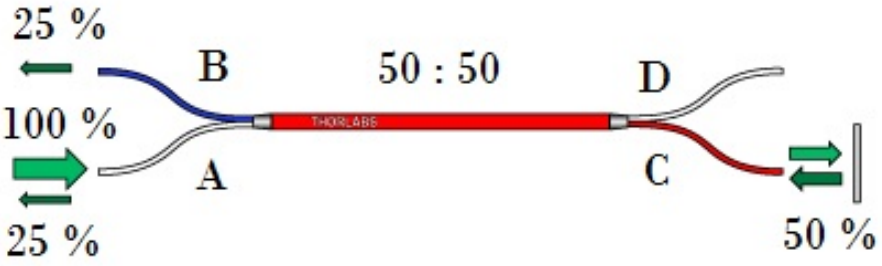

Figure 29: Schematic of a 50:50 split ratio fiber optic coupler, used as circulator. Adapted from [26].

All these explanations were simplified and did not take into account the insertion loss correspondent to each port of the fiber optic coupler and also, all the other power loss sources.

4.1.3 Fixed Focus Collimator

A collimator is a device that align a light beam in a specific direction, with all rays travelling parallel to each other.

In this project were used two collimators F220APC from Thorlabs Inc., with the following characteristics:

- Central wavelength $\lambda = 1064nm$;
- Numerical aperture $NA = 0.25$;
- Effective focal length $f = 11.17mm$;
- Output beam diameter $D = 2.4mm$;

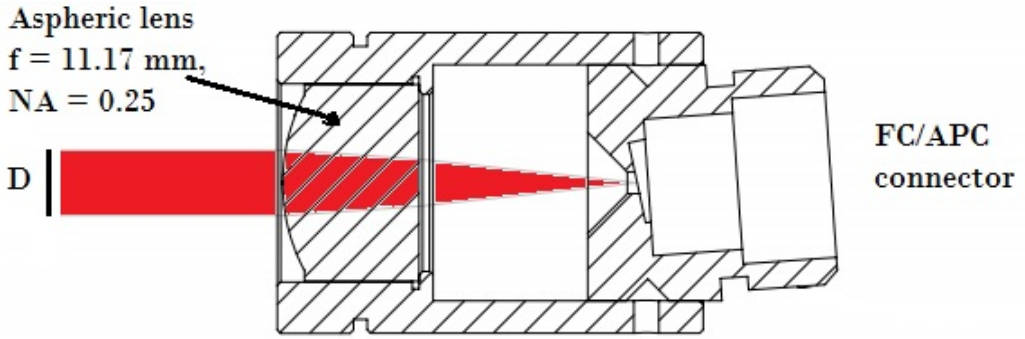

Figure 30: Schematic of a Thorlabs F220APC collimator. Adapted from [26].

In figure 30, it is represented a schematic of the collimator used on the experimental setup, whose main task is to collimate a laser beam that comes from an optical fiber, and also to collect the back reflected light from both reference and sample arms, and direct it into the optical fiber again.

These collimators are factory aligned, in order to make sure that the lens is at a distance, equal to the focal length, from the FC/APC connector output [26]. The aspheric lens used on the collimator (figure 30) has a coating that is anti-reflective, in order to prevent surface reflections that would introduce noise on the system. This coating assures a coefficient of reflection less than 0.5% between a wavelength range of $964 - 1164nm$.

4.1.4 Balanced Detector

In order to measure the interference signal from our SS-OCT system a balanced detector is required. Thus, the detector used in this project is the Thorlabs PDB471C, which is an InGaAs fiber coupled balanced amplified photodetector with a bandwidth of $400MHz$ and with an operating wavelength ranging between 900 and $1400nm$, optimized for $1060nm$ [26].

The detector used consists of two well matched photodiodes and an ultra-low noise, ultra-low distortion high speed transimpedance amplifier (TIA), which generates an output voltage (RF OUTPUT) that is proportional to the difference between the two optical input signals, as shown on figure 31. It functions as a balanced receiver by subtracting the two optical input signals from each other, which results in the cancellation of common mode noise. Note that the two photodiodes are

matched, in order to achieve a good common mode rejection ratio (CMRR), which allows small changes in the signal to be distinguish from the noise floor. Figure 32 shows the typical frequency response curve of the detector and it is clear that the device has a high common mode rejection ratio for frequencies between DC and $400MHz$.

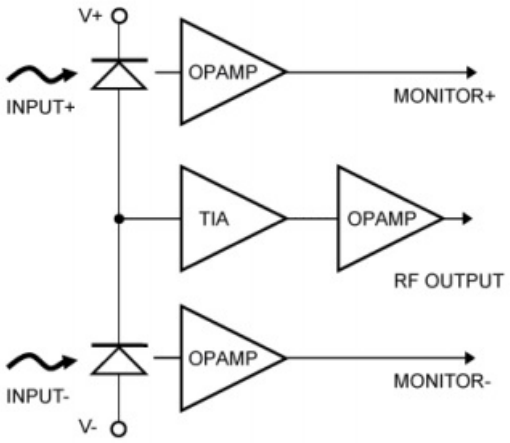

Figure 31: Schematic of a functional block diagram of the PDB471C balanced amplified photodetector [27].

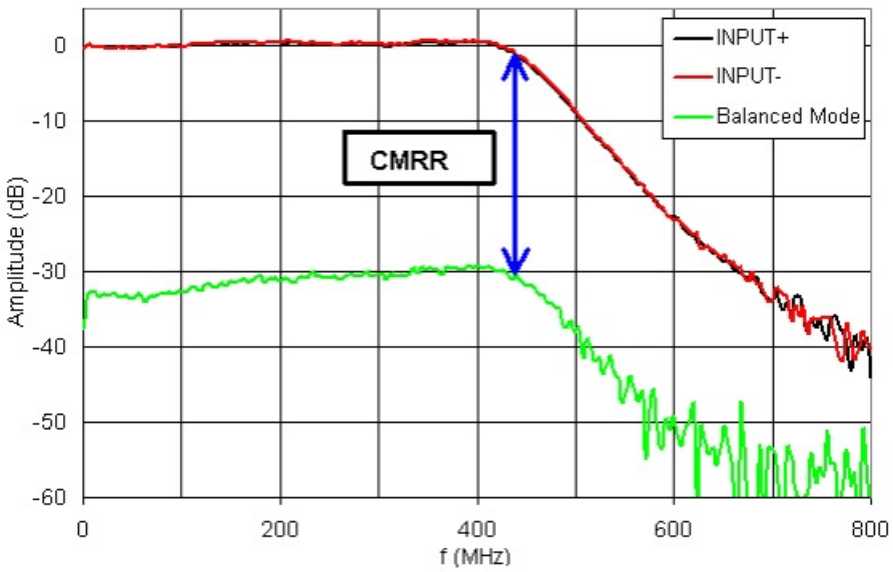

Figure 32: Typical PDB471C RF OUTPUT frequency response [27].

The balanced detector has a typical responsivity $R(\lambda)$ response of $0.72A/W$ at a wavelength of $1060nm$, as we can observe on figure 33. Within the sweep range of the laser source, which corresponds to the $110nm$ marked on figure 33, a variation of the detector responsivity of approximately $0.08A/W$ is expected. The detector has also a transimpedance gain $G_{V/A}$ of $10 \times 10^3 V/A$. Hence, the conversion gain $G_{V/W}$, which represents the ratio of the output voltage to the input optical power of the detector, can be expressed by $G_{V/W} = G_{V/A} \times R(\lambda)$ and clearly shows the gain wavelength dependence [26].

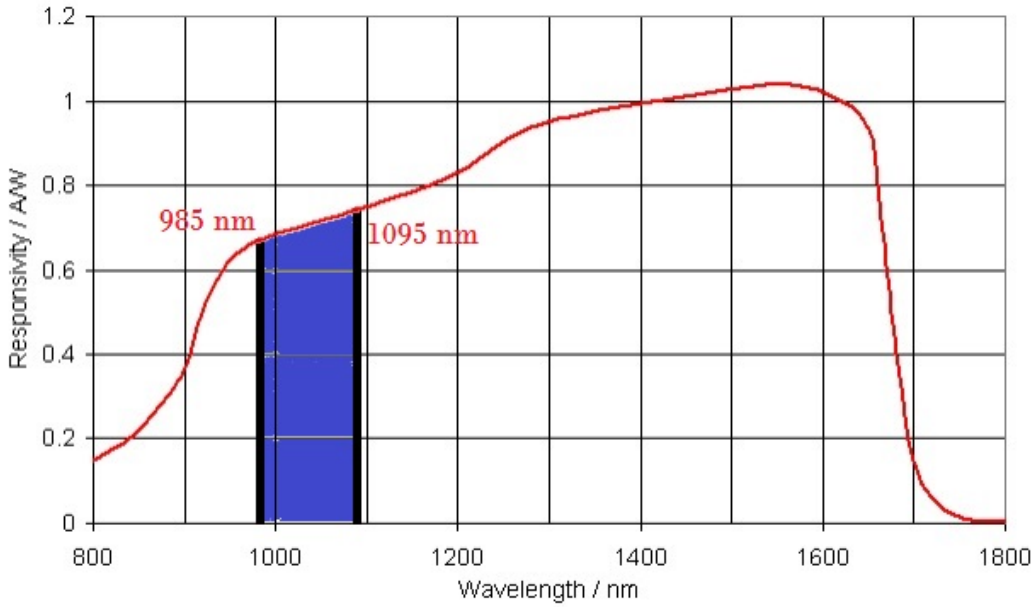

Figure 33: Typical PDB471C balanced detector responsivity. Adapted from [27].

Lastly, it is needed to emphasize the importance of balanced detection on swept source OCT systems. The DC term, resultant from the interferometric terms, has no relevant information. Thus, the cancellation of the DC terms by the balanced detection allows to achieve better resolution, by taking advantage of the analog to digital conversion dynamic range.

4.1.5 Gold Mirror

As mentioned on earlier chapters, a good reflectivity on the reference arm is the key to achieve a good sensitivity in OCT systems. Therefore, a Thorlabs PF10-03-

M01 protected gold mirror was used in the reference arm of the SS-OCT system developed. This mirror has an average reflectance higher than 96% over the wavelength range of $800nm$ to $20\mu m$ [26].

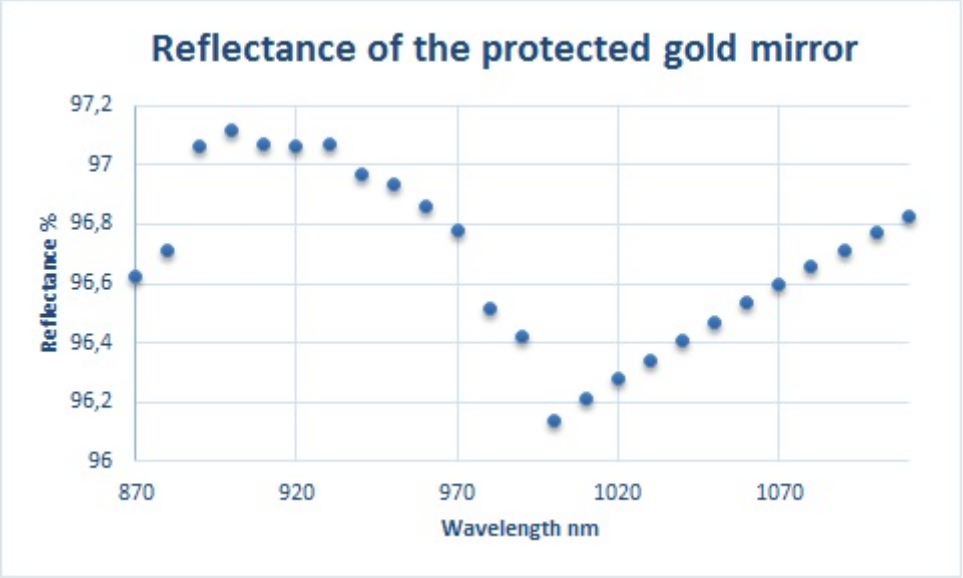

Figure 34: Reflectance of the protected gold mirror, Thorlabs PF10-03-M01, as function of the wavelength. Data taken from Thorlabs website [26] and treated on excel.

In figure 34, we are able to observe the reflectance of the protected gold mirror over the $110nm$ wavelength sweep range of our light source. A variation of approximately 1% on the reflectance of the mirror is also observed over the analysed wavelength range.

4.1.6 Scanning Objective Lens

On this project, three different scanning objective lenses were used, where tests have been made in order to determine the best possible combination. The best objective lens combination is the one that allows to achieve the best performance parameters. Therefore, the objective lenses used were the Thorlabs LSM02-BB, LSM03-BB and LSM04-BB [26].

These scan lenses are made as telecentric objectives, which are a viable option for applications such as OCT, where image scan across the sample is required. A

major advantage of this kind of objective lens is the nearly constant spot size in the image plan over the entire field of view, which results in constant image resolution and minimizing image distortion [26].

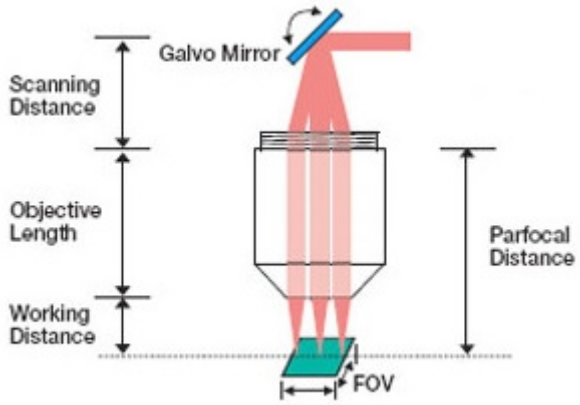

Figure 35: Schematic of a scanning objective lens [26].

On the figure 35 a schematic of scanning objective lens is shown, where some distances are identified. A list of these distances and parameters is presented and explained below:

- Scanning distance: The scanning distance is the distance between the galvo mirror pivot point and the back mounting plane of the objective. Respecting this distance is very important in order to maximize image resolution;

- Pupil size: The pupil size determines the ideal laser beam diameter used to image the sample in order to maximize resolution;

- Field of view: The field of view (FOV) is the maximum size of the area on the sample that can be imaged with good resolution and it is dependent on the objective specifications;

- Depth of view: Depth of view (DOV) or depth of focus (DOF) is related to the distance between the parallel planes on both sides of the front focal plane, where the beam spot diameter is $\sqrt{2}$ greater than the beam spot diameter at the front focal plane (see figure 18, on section 3.5).

On the following table, some of the relevant optical parameters of the scanning objective lenses used are specified.

Table 1: Properties of the scanning objective lenses used on the SS-OCT layout [26].

	LSM02-BB	**LSM03-BB**	**LSM04-BB**
Magnification	10	5	3
Design Wavelength	1050 ± 50 nm		
Effective Focal Length	18 mm	36 mm	54 mm
Lens Working Distance	7.5 mm	25.1 mm	42.3 mm
Scanning Distance	16.1 mm	18.9 mm	
Pupil Size $(1/e^2)$	4 mm		
Depth of View	0.05 mm	0.22 mm	0.49 mm
Parfocal Distance	30.7 mm	50.5 mm	80.7 mm
Mean Spot Size	11 μm	21 μm	29 μm

4.1.7 2D Galvanometer System

As pointed several times above, in order to scan the sample, a galvanometer system is required. The explanation of how a galvo system works has already been made on section 2.1.3 (see figure 5). Therefore, the galvanometer system used in this project is the Thorlabs GVS002 - 2D galvo system, represented in figure 36.

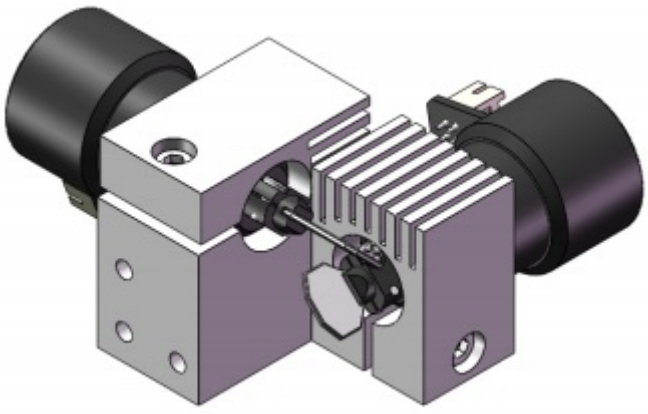

Figure 36: Illustration of the 2D - galvo system used on the experimental setup. Adapted from [28].

The galvo system GVS002 is a dual axis scanning system, used for small diameter beam applications (less than 5 mm), with position sensor linearity of 99.9%. Each axis scan is associated to a galvo motor, coupled to a mirror, which has a protective silver coating with a reflectance of $96.85\% - 97.28\%$, over a wavelength range of 970 to 1100 nm, as we can observe on figure 37. Each galvo motor is controlled with a voltage generated by the galvo driver, in order to move the position of the respective mirror. Thus, the analog position signal input voltage range of the galvo drivers is $\pm 10V$, where the scale factor can be mechanically switched between three different factors:

- 1 V per degree;
- 0.8 V per degree;
- 0.5 V per degree;

Hence, it is possible to achieve a maximum scan angle of $\pm 10^{o}$, $\pm 12.5^{o}$ and $\pm 20^{o}$ respectively, with an angular resolution of $15\mu rad$ [26] [28].

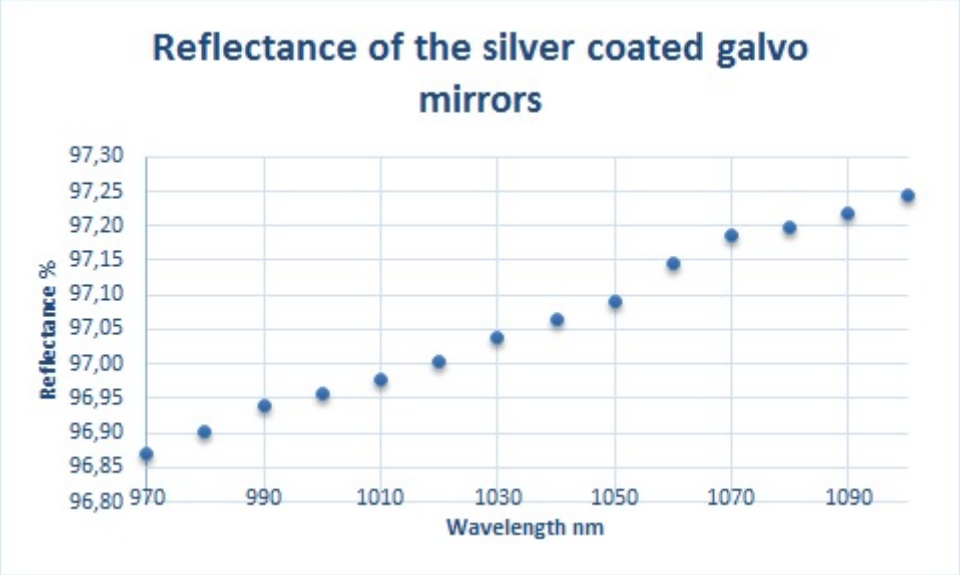

Figure 37: Reflectance of the silver coated galvo mirrors as function of the wavelength. Data taken from Thorlabs website [26] and treated on excel.

It is important to clarify that the total number of motor steps or in this case the number of A-scans is defined on the software interface.

4.1.8 In-Line Optical Fiber Polarization Controller

A light wave is composed of two orthogonal electrical vector field components that vary in amplitude and frequency. So, basically, we can say that light is polarized when these two components differ in phase or amplitude.

OCT systems are very dependent of the degree of polarization of the light. Thus, in our experimental setup, a Thorlabs PLC-900 in-line optical fiber polarization controller was used on the sample arm. The purpose of the polarizer was to ensure that light entering the optical coupler OC-4 in both input ports (see figure 19), had the same degree of polarization, in order to maximize the detection sensitivity.

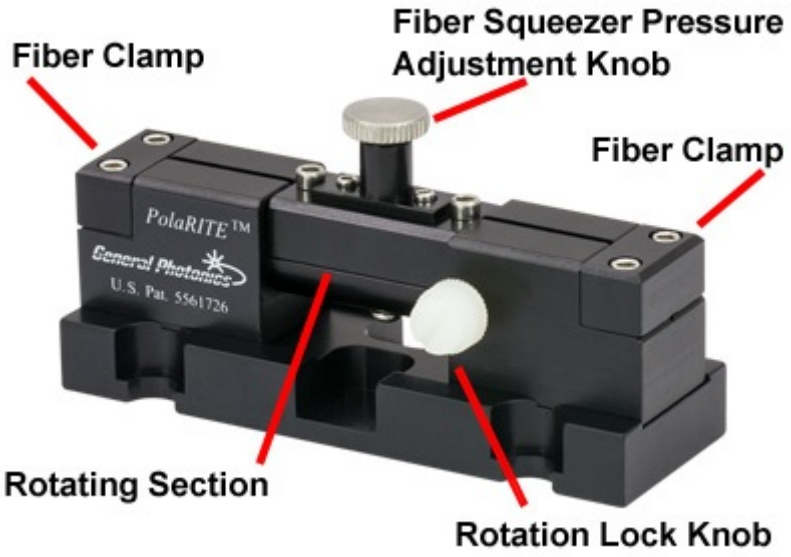

Figure 38: Schematic of the Thorlabs PLC-900 in-line optical fiber polarization controller with identification of the respective constituents [26].

On figure 38, it is presented a scheme of the polarizer used, where the operation principle consists of comprising a fiber squeezer that rotates around the optical fiber. Applying pressure to the fiber produces a linear birefringence, which creates a fiber wave plate, whose retardation depends with the applied pressure. Simple squeeze and rotation operations can generate the desired polarization state from any arbitrary input polarization [26].

4.1.9 Data Acquisition Hardware

On our swept source OCT system, the acquired data is displayed on a computer, where the acquisition code was programmed using the Visual Studio 2008 software, developed by Microsoft Corporation. The programming language used was $C++$ and the interface runs with the Visual $C++ \setminus CLI$.

However, in order to process the acquired data, it is necessary to digitalize the interference signal provided by the detector. The acquisition board used was a XMC module X5-400M (figure 39), developed by Innovative Integration. This acquisition board has an acquisition rate up to 400 MSPS (Mega Samples Per Second), and allows to use external trigger and clock or internal trigger and clock [29]. The acquisition board have two different modes of package acquisition, it can acquire data with a specific size in frames or it can make a continuum acquisition. On our system, we used the frame mode, where each data package has 2048 samples, which contains an entire A-scan, also the external clock and trigger signals are generated by the laser source.

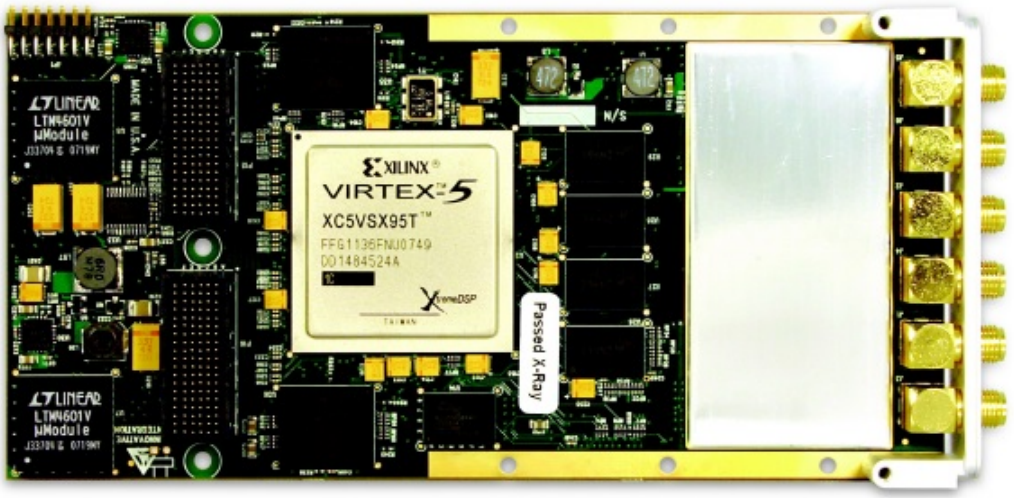

Figure 39: Picture of the XMC module X5-400M board from Innovative Integration [29].

The interface allow us to control the galvanometer system, as has been already told, and for that purpose a National Instruments Corporation PCI-6010 board is used to generate the galvo control signal [30]. The main task of this board is to generate the analog wave signals that will control the position of the galvanometers.

Both acquisition and galvo control are synchronized by the clock and trigger from the light source.

Chapter 5

Experimental Performance Parameters Results and Analysis

On this chapter, we will focus on presentation and discussion of the performance parameters results of the SS-OCT system. You should note that the theoretical principles of such parameters have already been given on chapter 3.

Experiments were made in order to better understand certain effects of some of the components of the OCT system. With these tests, we were able to choose the correct components and configuration, which give the best performance results acquired so far.

Finally, we proceed to the discussion and analysis of results and tests presented, identifying possible improvements and comparing the results with the SS-OCT system minimum requirements.

5.1 Sensitivity

The sensitivity and all the other performance parameters were measured for the SS-OCT system setup presented on figure 19 and described on section 4.1.

The procedure to measure the system sensitivity was already explained on section 3.2, however, it was necessary to add a new element to the system layout, just for this procedure.

As we can find on literature [31][32]("*...Sensitivity was measured by placing a neutral density filter ND 4.0 of well-known optical density (OD) in the object arm...*"[31]), it is necessary to introduce a neutral density filter in the sample arm, for example, between the scanning objective and the sample mirror. Its function is to attenuate the light on the sample arm, in order to achieve similar optical power on both arms of the SS-OCT system. Thus, it is possible to determine the correct system sensitivity. The neutral density filter used was the Thorlabs $NENIR20A$, which has an optical density (OD) at $1064nm$ of 2.14. As already mentioned, light travels backward and forward in the sample arm, so the effect produced by the filter is doubled and an attenuation of $42.8dB$ is expected.

Therefore, we can apply the procedure explained on section 3.2, and use equations 21 and 22 to calculate the system sensitivity. So, we can start by analysing the obtained noise signal and calculating its standard deviation.

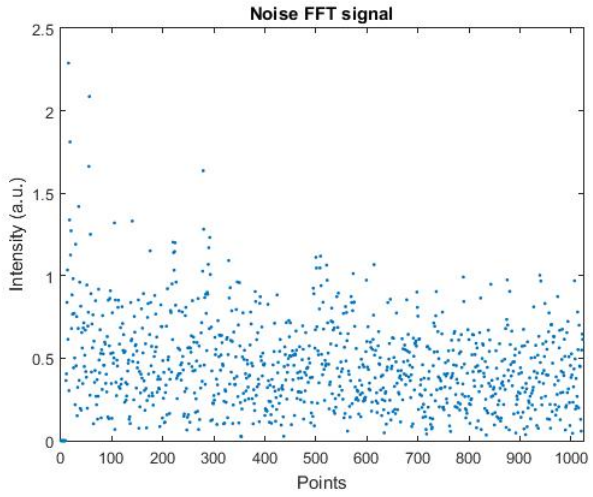

Figure 40: FFT of the noise signal obtained from the SS-OCT system, whose standard deviation is $\sigma_{noise} = 0.2542$.

The FFT noise signal obtained from the system is shown on figure 40. These data was treated on Matlab R2015a, where a fitting function was applied, in order to extract the standard deviation from its residuals. Thus, the standard deviation of the noise signal is $\sigma_{noise} = 0.2542$. Note that each point on the graphic is depth related, so each point corresponds to $2.5536\mu m$.

Continuing the procedure, it is time to determine the maximum point spread function intensity value of the interference signal, as we can observe on figure 41.

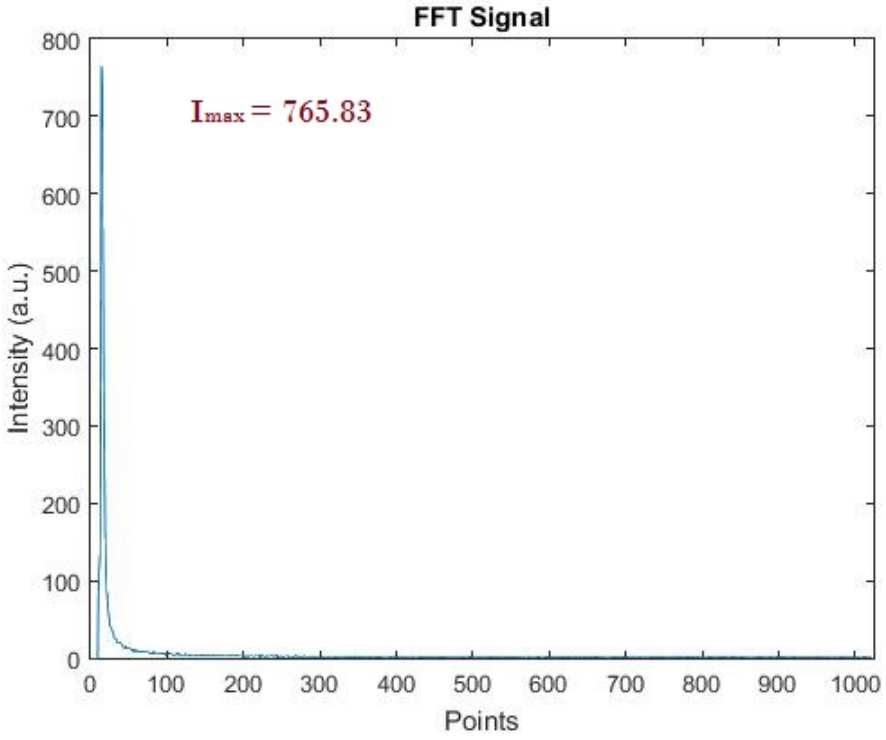

Figure 41: Point spread function obtained from the SS-OCT for a depth position ΔZ, whose maximum intensity is $i_{Dmax} = 765.83$.

Thus, the maximum signal intensity is $i_{Dmax} = 765.83$ and using the following equation, the system sensitivity is:

$$S = 20\log\left(\frac{i_{Dmax}}{\sigma_{noise}}\right) + 20 \cdot OD = 20\log\left(\frac{765.83}{0.2542}\right) + 20 \times 2.14 = 112.38dB \quad (35)$$

This result is a great achievement, because the system sensitivity is much higher than the minimum required sensitivity for an OCT system $90dB$ [3][11][20].

The sensitivity result above, was measured for the final and best SS-OCT layout possible, which is represented on figure 19. However, several measurements were made with different scanning objectives, in order to show if there was a significant change on system sensitivity. It is important to be aware that the optical density filter was not used for this measurement however, the same conclusions can be applied, because the filter only adds a constant component to the sensitivity. The following results were obtained for a experimental layout where the scanning objective lens of the sample and reference arms are changed.

Table 2: Sensitivity results for different sample and reference arms scanning objective lens configurations.

Sample arm	**Reference arm**	**Sensitivity (dB)**
LSM02-BB	LSM03-BB (blue)	73.62
LSM02-BB	LSM03-BB (pink)	72.79
LSM02-BB	LSM04-BB	73.38
LSM03-BB (pink)	LSM02-BB	75.06
LSM03-BB (pink)	LSM03-BB (blue)	75.23
LSM03-BB (pink)	LSM04-BB	74.97
LSM03-BB (blue)	LSM02-BB	76.13
LSM03-BB (blue)	LSM03-BB (pink)	73.47
LSM03-BB (blue)	LSM04-BB	74.82
LSM04-BB	LSM02-BB	76.13
LSM04-BB	LSM03-BB (pink)	73.03
LSM04-BB	LSM03-BB (blue)	73.22

By analysing the table 2, it is clearly visible that there are not large variations in the system sensitivity, for the scanning objective lenses configurations tested. Actually, it is only observed a small sensitivity variation of $1-4dB$ from the obtained maximum value. The maximum value of $76.13dB$ was obtained for two distinct configurations, being one of those, the configuration used on the SS-OCT final layout (LSM03-BB on sample arm and LSM02-BB on reference arm).

5.1.1 Polarization control effect

As said in the last chapter, we use an in-line optical fiber polarization controller on the sample arm, to convert an arbitrary input polarization into the desired polarization state. So, the following procedure was executed to maximize the interference intensity signal, and obviously maximize the sensitivity of the system.

First, pressure was applied on the fiber squeezer, while monitoring the output optical power, on the SS-OCT system software interface. Applying pressure causes a significant increase on the monitored optical power so, we kept increasing the pressure until the optical power started to decrease. Keeping the achieved pressure, we rotated the fiber squeezer until maximum output optical power was obtained.

After this procedure, a significant increase on system sensitivity was clearly visible and can be proved by the following results. Once more, the optical density filter was not used on the procedure.

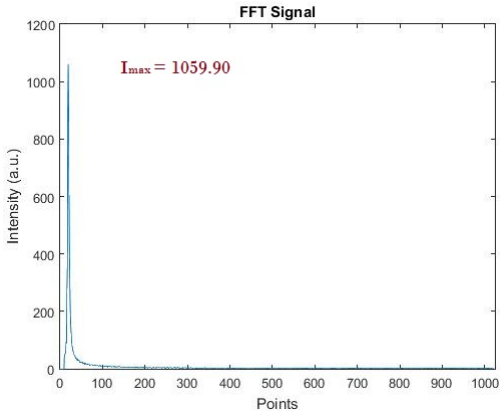

(a) Interference FFT signal when polarization state is maximized.

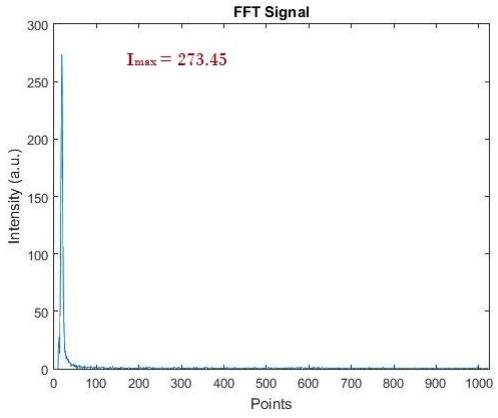

(b) Interference FFT signal when polarization state is not maximized.

Figure 42: Inteference FFT signals for different polarization states.

On figure 42, it is clearly visible the polarization influence on the interference signal intensity. Therefore, when the polarization state is maximized a sensitivity of $72.40dB$ is achieved, on the other hand, when the polarization state is not maximized lower sensitivity is obtained, resulting on a system sensitivity of $60.63dB$. This result, reflects the importance of polarization control on our SS-OCT system, resulting in lower sensitivity results when the polarization state is not ideal.

5.1.2 Roll-off

The procedure to measuring the roll-off performance, consists of successively measure the sensitivity of the system for different depth positions.

On figure 43, we are able to observe the roll-off sensitivity results of the final SS-OCT configuration. For this results, sensitivity samples were taken for different depth positions, spaced of $20\mu m$, within a range of nearly $4mm$. Once more, for simplicity reasons, the neutral density filter was not used in the following measures.

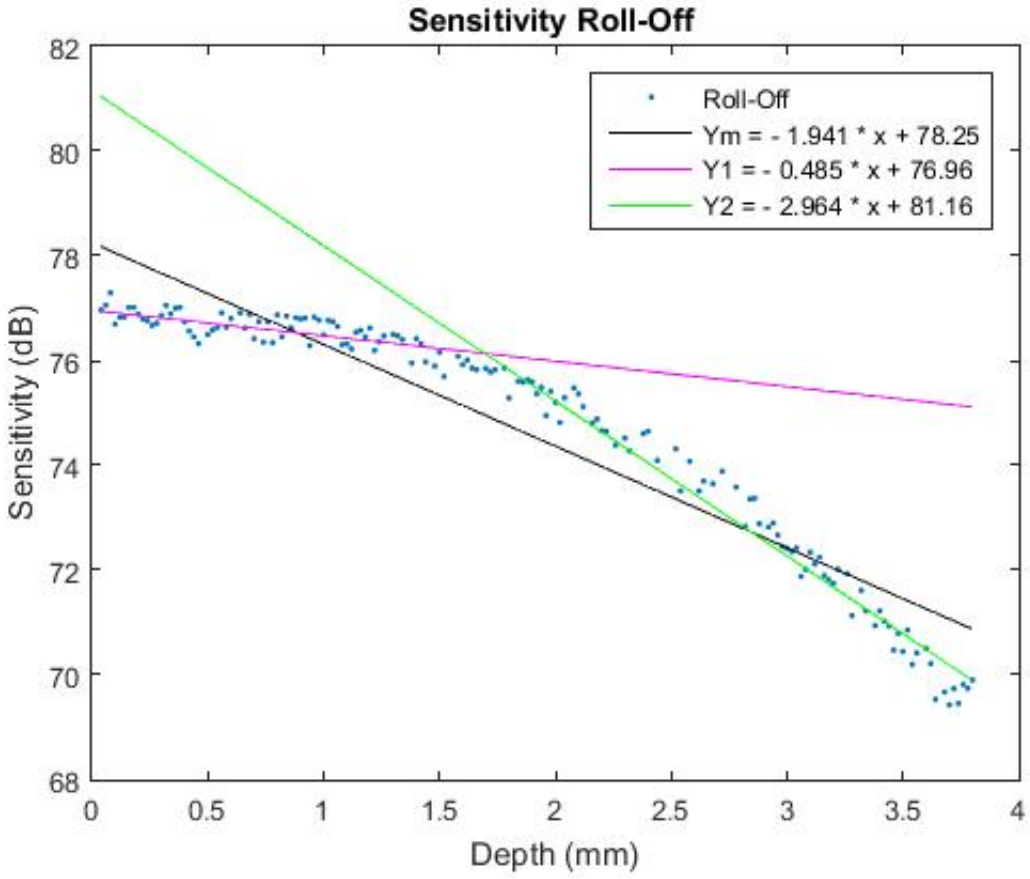

Figure 43: Roll-off sensitivity performance of the final SS-OCT system setup. Sensitivity measurement for different depth positions.

On figure 43, were made three different linear fits to the roll-off sensitivity results. The slope of each linear fit represents the R-number, which quantifies the roll-off of the system. Thereby, analysing the graphic on figure 43, it is easy to see that the SS-OCT system roll-off shows two different behaviours. At first, it has a nearly

constant behaviour, where the sensitivity fall-off is minimal, corresponding to a R-number of nearly $0.5dB/mm$. This behaviour, is observable up to $1.5mm$ depth, and is shown on the graphic, by the fit in pink ($Y_1 = -0.485x + 76.96$). After this point until $4mm$ depth, the R-number is about $3dB/mm$, which represents a sensitivity fall-off six times bigger than the previous behaviour, and is shown on the graphic, by the fit in green ($Y_2 = -2.964x + 81.16$). At last, the fit in black ($Y_m = -1.941x + 78.25$), matches to a R-number of nearly $2dB/mm$, and represents the global roll-off sensitivity of the swept source OCT system.

The obtained results meet the minimum requirements of having a R-number bellow $10dB/mm$ [20][21]. We can compare our system roll-off sensitivity results with the results shown on a paper with a similar setup, *Ultrahigh speed 1050nm swept source/Fourier domain OCT retinal and anterior segment imaging at 100,000 to 400,000 axial scans per second* [17]. We achieved a sensitivity fall-off of $8dB$ over $4mm$ depth, where on their paper, they achieved a sensitivity fall-off of $6dB$ over $4mm$ depth. However, our system sensitivity is more than $10dB$ higher, than the sensitivity achieved on their experiment, which somehow compensates the worse roll-off performance of our SS-OCT system. Thus, there is still space to improve our system in term of roll-off sensitivity, especially by getting a better system alignment.

5.2 Dynamic Range

The procedure to measure the system dynamic range was already explained on section 3.3. Therefore, a similar procedure to the sensitivity measurement was executed, where the main difference is the calculation of the noise standard deviation σ_{noise}. Thus, the noise component is calculated in the same graphic as the maximum intensity peak, as shown on figure 44, and the system dynamic range is:

$$D = 20 \log \left(\frac{1627.9}{1.1820} \right) = 62.78dB \tag{36}$$

A dynamic range of $D = 62.78dB$ is a very promising result, since it is considerable higher than the minimum dynamic range ($40dB$) required for an SS-OCT, and clearly shows the great signal to noise ratio of our swept source OCT.

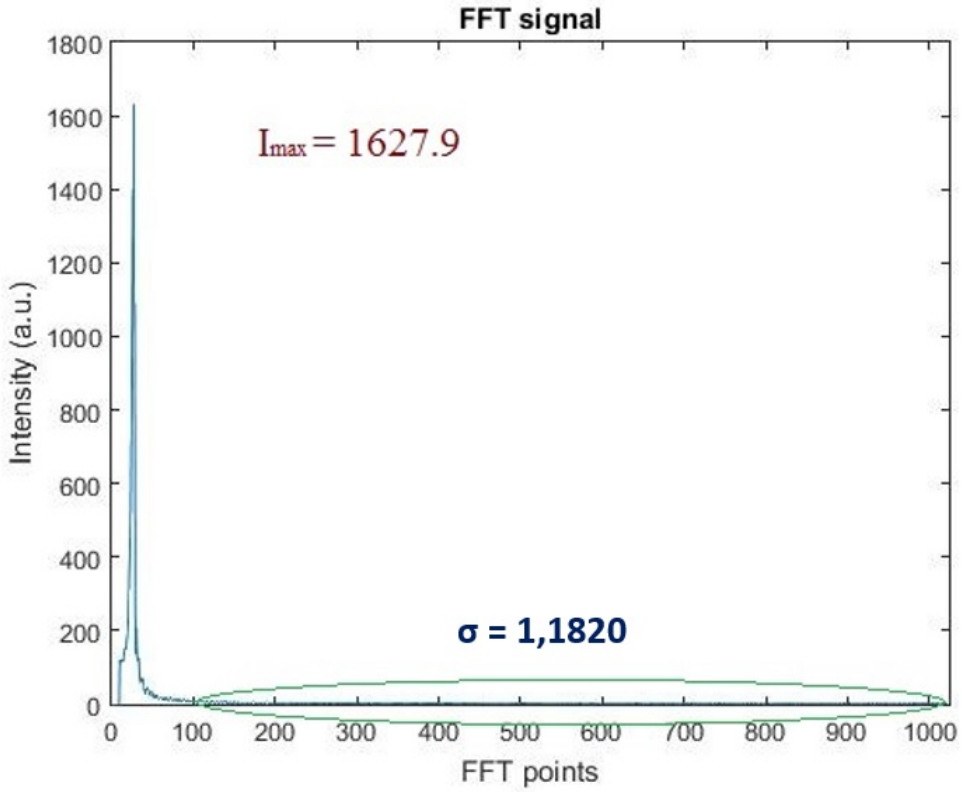

Figure 44: Interference signal from our SS-OCT, showing relevant data to calculate the system dynamic range.

5.3 Axial Resolution

Axial resolution is one of the most important performance parameters in an OCT system, and the theoretical SS-OCT system axial resolution can be calculated using equation 24, from section 3.4.

$$\delta z = \frac{2\ln(2)}{\pi}\frac{1060 \times 10^{-9}}{110 \times 10^{-9}} = 4.51 \times 10^{-6} m = 4.51 \mu m \tag{37}$$

Thus, the theoretical axial resolution of the system is $\delta z = 4.51 \mu m$. However, as in many practical situations, the theory do not match with reality, and the real axial resolution of the system is a bit higher than what was expect by the theory.

So, for practical situations, the axial resolution measurement, basically, consists on measuring the FWHM of the point spread function. Remember that for this measurement, the sample arm objective lens was the $LSM03-BB$ and the reference

arm objective lens was the $LSM02 - BB$. Therefore, on figure 45, it is shown a Matlab graphic, where the system axial resolution was measured. In order to determine the FWHM of the PSF, it was necessary to use a Lorentzian fitting and function to calculate the FWHM of the respective fitting curve [9]. These functions can be found on the *MathWorks, Inc.* web site (www.mathworks.com), where the respective functions can be download from [33] [34].

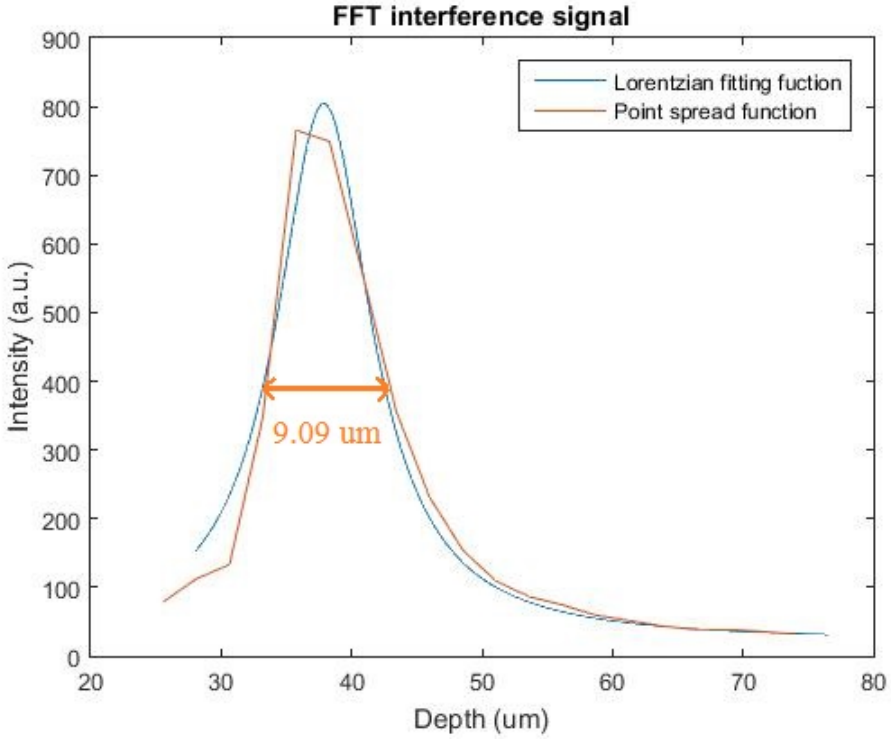

Figure 45: PSF for measurement of the SS-OCT axial resolution. Data treated on Matlab R2015a.

Thus, following the described procedure, we were able to achieve an axial resolution $\delta z = 9.09\mu m$. Despite the deviation from the theoretical value, axial resolution is still below the value recommended for biomedical applications [9].

Similarly, to what was made for the system sensitivity, an experiment was performed in order to determine the axial resolution dependence on the scanning objective lens configuration of reference and sample arms. The following table, shows the results of such experiment.

Table 3: Axial resolution measurement for different sample and reference arms scanning objective lens configurations.

Sample arm	**Reference arm**	**Axial Resolution (μm)**
LSM02-BB	LSM03-BB (blue)	32.97
LSM02-BB	LSM03-BB (pink)	36.00
LSM02-BB	LSM04-BB	30.97
LSM03-BB (pink)	LSM02-BB	9.96
LSM03-BB (pink)	LSM03-BB (blue)	19.09
LSM03-BB (pink)	LSM04-BB	19.91
LSM03-BB (blue)	LSM02-BB	9.12
LSM03-BB (blue)	LSM03-BB (pink)	21.46
LSM03-BB (blue)	LSM04-BB	19.09
LSM04-BB	LSM02-BB	10.62
LSM04-BB	LSM03-BB (pink)	23.42
LSM04-BB	LSM03-BB (blue)	27.20

Looking at the table 3, it is clearly visible that the configuration with a $LSM03-BB$ objective lens on sample arm, and a $LSM02-BB$ objective lens on the reference arm, offers much better results, which is the reason why it is the final configuration of the SS-OCT layout. However, there are large variations on the axial resolution, which at first do not make any sense, once the axial resolution, is only dependent of the central wavelength and bandwidth of the light source. So, we took a look at one of the point spread function, shown on figure 46, whose resultant axial resolution was so poorly.

The analysis of the figure 46, clearly shows what appears to be the overlap of several intensity peaks, which causes broadening of the major peak. This result, explains why the axial resolution is so poorly for some configurations. However, this effect should not happen, since there is only one reflection, which originates only one intensity peak, after Fourier transformation. Hence, the first thing we thought, was that maybe some component was broken and because of that multiple reflections appeared on the FFT signal. Thus, several experiments were made to find the broken component, which was never found. Therefore, if the problem is not on the components, it should be something else, and finally we found the problem,

on the literature [8] [18].

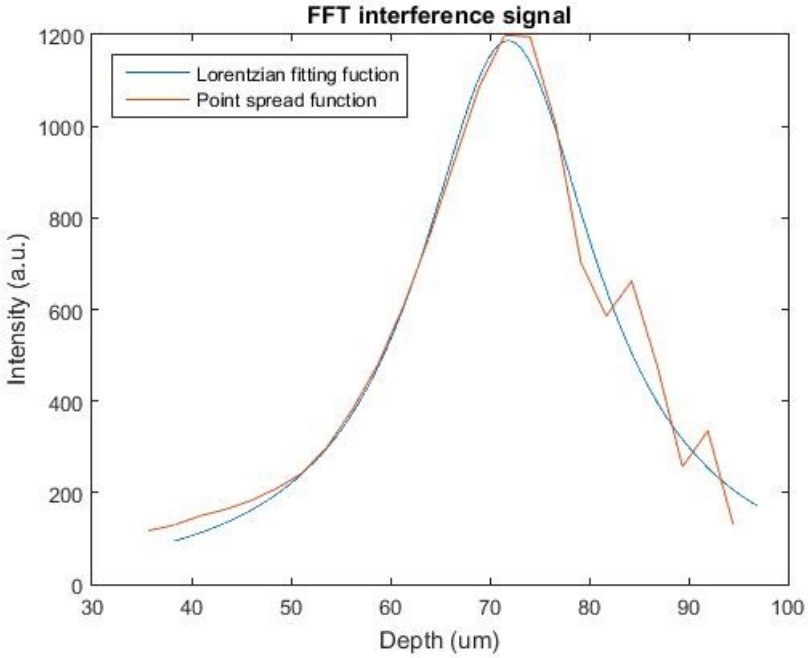

Figure 46: PSF and respective Lorentzian fitting curve of a SS-OCT interference signal, when the scanning objective lens $LSM03 - BB$ is used in both arms of the interferometer.

The problem causing the bad axial resolution, is in fact, the dispersion imbalance between the two interferometer arms. This phenomenon, happens due to light passing through a refractive material, whose index of refraction is frequency dependent. Hence, dispersion introduces additional phases to the Fourier components, which results in a corresponding increased FWHM and so, poor axial resolution is achieved. A quotation from the book " Optical Coherence Tomography - Technology and Applications" [8], clearly explains the consequences of dispersion: *" The most dramatic impact of dispersion on OCT signals is a degradation of depth resolution δz and reduced sensitivity"* [8].

5.3.1 Dispersion Compensator

The problem of dispersion imbalance between both arms of the interferometer has been identified. Thus, in order to solve this problem, light in both arms of

the interferometer should pass through the same glass, to make sure that dispersion is balanced. Since, on the sample arm, the scanning objective lens was the $LSM03 - BB$, it was necessary to have on reference arm, a component with similar characteristics. Therefore, on the reference arm a dispersion compensator was introduced, Thorlabs Inc. $LSM03DC$, which provide up to second order dispersion compensation. A photograph of the reference arm with the dispersion compensator, is shown on figure 47.

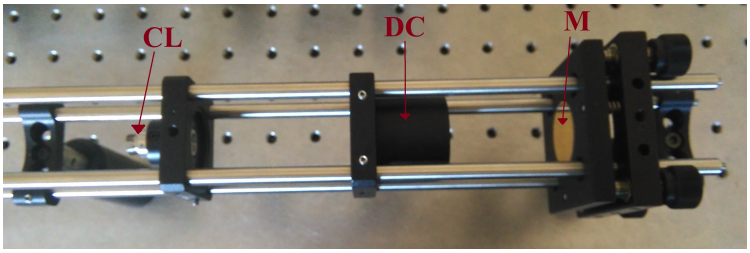

Figure 47: Picture of the reference arm with a dispersion compensator $LSM03DC$ instead of the scanning objective lens $LSM03 - BB$. CL - fixed focus collimator; DC - dispersion compensator; M - gold mirror;

After this implementation, the next step was to measure the system axial resolution with this setup.

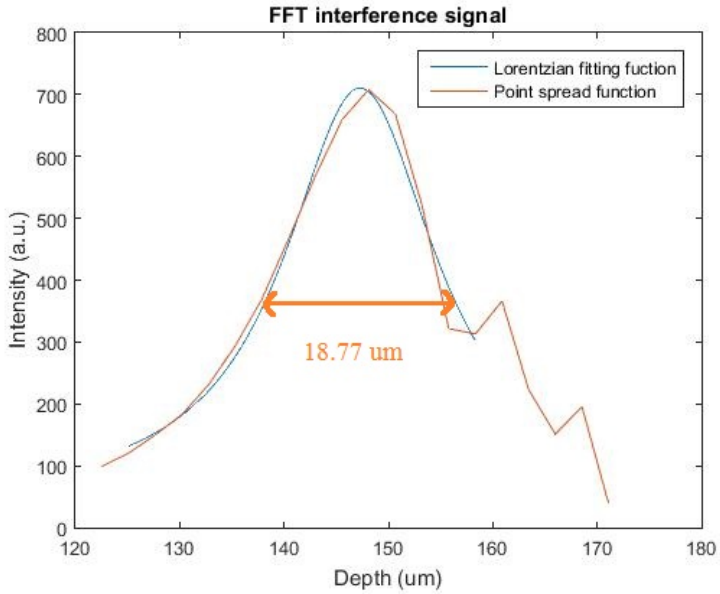

Figure 48: SS-OCT axial resolution measurement when a dispersion compensator is used on the reference arm.

On figure 48, is shown the axial resolution measurement result, of the setup mounted to balance the dispersion in both interferometer arms. Different from what was expected, there was no real improvement on the system axial resolution, was obtained an axial resolution of $18.77\mu m$. If we pay attention, this result is very close to the axial resolution obtained when both interferometer arms use the scanning objective lens $LSM03-BB$ as we can observe on table 3. In fact, a slight decrease in the axial resolution was observed, compared to the data on table 3, but the dispersion imbalance signature is still present on figure 48.

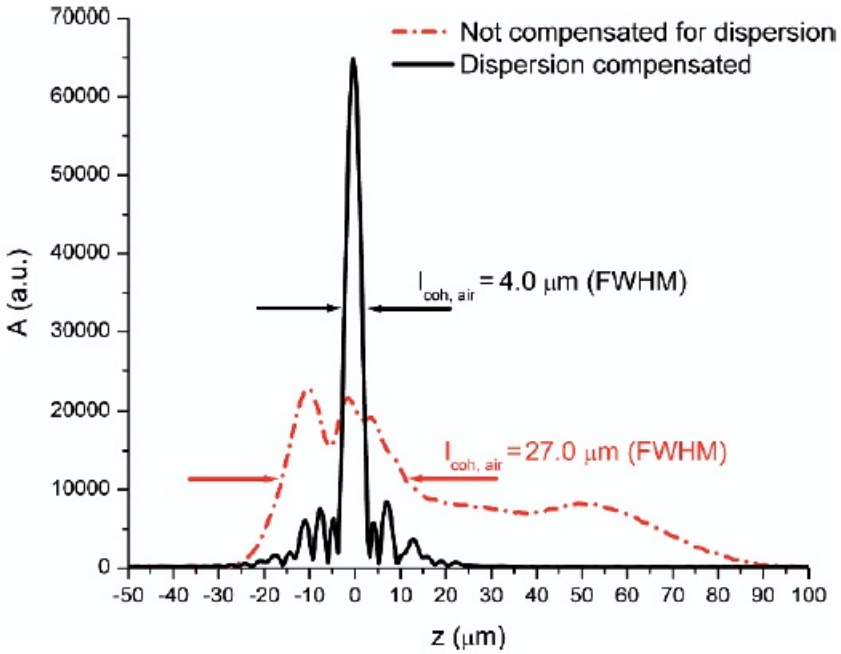

Figure 49: Graphic comparing dispersion compensated and uncompensated data and its implications on the FFT signal[8].

In conclusion, this result is very weird, because if the problem is dispersion imbalance, the best balanced configurations, are when both arms have the same scanning objective lens $LSM03-BB$ or when the sample arm use the scanning objective $LSM03-BB$ and the reference uses the dispersion compensator $LSM03DC$. However, with these configurations the achieved axial resolution is about $18-22\mu m$, which is much worse than the $9.09\mu m$ achieved with the final configuration (LSM03-BB and LSM02-BB). This means that the final configuration can perform a better dispersion balance between both arms, which does not make much sense, once the

two scanning objectives are different. Thus, it is possible that some other layout component could be introducing dispersion terms, and the final configuration is the best way to compensate those factors. Nevertheless, we could not find that component yet. Another reason, can be that the third and fourth order dispersion terms are causing the distortion, whose terms cannot be balanced by the dispersion compensator used, which only compensates the first and second order dispersion components. Therefore, other methods of dispersion compensation need to be implemented, specially by software implementations. The dispersion miss-match, can be corrected by the addition of appropriate phase factors to the interferometric signal data before the inverse Fourier transformation [8]. Figure 49 shows a graphic from [8], where are illustrated the consequences of software dispersion compensation. A huge improvement on the axial resolution was observed, as well in signal strength.

5.3.2 Depth Dependence of Axial Resolution

It is interesting to observe how the axial resolution changes as function of depth. A god OCT system has an axial resolution that is nearly constant over a wide depth range.

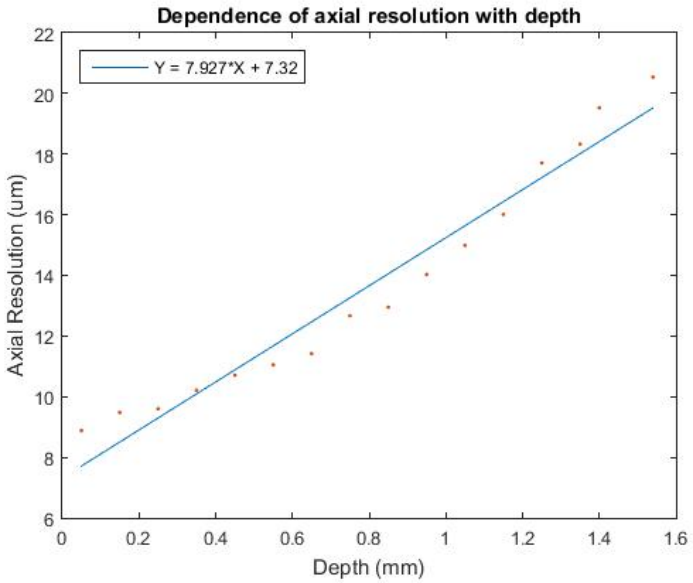

Figure 50: Dependence of the system axial resolution with depth for the final system setup.

By analysing the figure 50, a linear dependence of the axial resolution as function of depth, instead of staying at a constant value is clearly visible. A linear fitting to the data, shows an axial resolution increase of nearly $8\mu m$, for each $1mm$ of depth. Once more, the increased axial resolution is related to the observable dispersion imbalance between both arms of the interferometer. Even when the system setup is maximized to achieve the better dispersion balance, with increasing depth, is clearly visible the effect of the dispersion miss-match. This is obviously a huge problem in the current experimental setup, once for deeper positions, the axial resolution is very poor, resulting in a degraded image resolution.

5.4 Lateral Resolution

The lateral resolution, of the swept source OCT system studied, is given by equation 25, and by looking to the respective scanning objective lens specifications from table 1. Thus, for the scanning objective lenses used on the OCT system, the lateral resolution is:

$$\delta x_{LSM02} = \frac{4 \times 1050 \times 10^{-9} \times 18 \times 10^{-3}}{\pi \times 4 \times 10^{-3}} \simeq 6\mu m \tag{38}$$

$$\delta x_{LSM03} = \frac{4 \times 1050 \times 10^{-9} \times 36 \times 10^{-3}}{\pi \times 4 \times 10^{-3}} \simeq 12\mu m \tag{39}$$

$$\delta x_{LSM04} = \frac{4 \times 1050 \times 10^{-9} \times 54 \times 10^{-3}}{\pi \times 4 \times 10^{-3}} \simeq 18\mu m \tag{40}$$

Looking at the lateral resolution calculations, the $LSM03 - BB$ scanning objective lens is able to achieve a lateral resolution closer to the axial resolution of the system, which allows to a better image uniformity. Nevertheless, the scanning objective $LSM02 - BB$ has the better lateral resolution. It is also important to note that the final system has two scanning objectives, one on each arm of the interferometer however, only the objective on the sample arm is relevant for the system lateral resolution.

The next step, is to find the numerical aperture of each scanning objective lens, using the following equation: $NA = \frac{d}{2f}$. It is also important to determine the depth of focus (FOV) for each objective, using equation 26, whose results are displayed on

the following table.

Table 4: Table showing the results of the numerical aperture and depth of focus of each scanning objective used on the SS-OCT system layout.

Scanning Objective	**NA**	**FOV** (μm)
LSM02-BB	0.11	174
LSM03-BB	0.056	670
LSM04-BB	0.037	1534

By analysing the data on table 4, we should expect that the scanning objective lens $LSM04-BB$ is the best option to be used on the sample arm, because it allows to image over a deeper range, than the other scanning objective lenses. However, the aim of the present SS-OCT system is to image the retina of small animals, which is a very thin layer so, the scanning objective $LSM03-BB$ is also a good choice. We need also to keep in mind the trade of between lateral resolution and depth of focus. Therefore, once both $LSM03-BB$ and $LSM04-BB$ have enough depth of focus range, for this specific application, the obvious choice is to use the $LSM03-BB$ scanning objective, because it allows to achieve an higher lateral resolution.

5.5 Coverslip Thickness Determination

The following experiment, shows a minor application of the SS-OCT system developed, where we try to determine the thickness of a coverslip (cover glass). The coverslip has an area of $22 \times 22mm^2$, whose thickness can go from 130 to $160\mu m$, as specified by the manufacturer. Therefore, the coverslip is now our sample instead of the gold mirror, and the respective FFT signal result is shown on figure 51. Each FFT peak on figure 51, represents a back-reflection from the coverslip sample. Thus, the distance between both intensity peaks, is actually the thickness of the coverslip. Hence, the thickness of the coverslip is $155.77\mu m$, which is within the range specified by the manufacturer. This is an important result, because it validates the calibration of the OCT system.

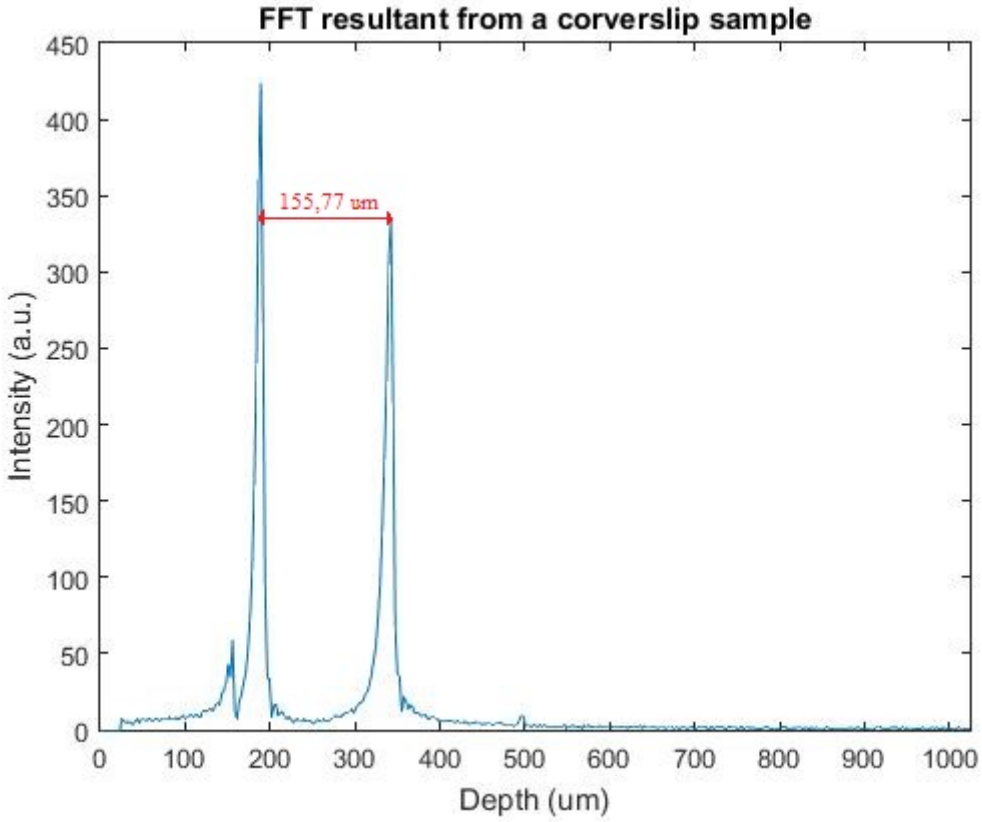

Figure 51: FFT interference signal obtained from a coversplit sample, with a thickness of 155.77μm.

5.6 Discussion and Analysis of the Experimental Results and Procedure

One of the most important aspects of developing and mounting an OCT system, is to assure that the system is perfectly aligned. This is also one of the most difficult aspects to accomplish and requires lots of time and patience. When mounting the SS-OCT system layout, it was much easier to align the final system than align the layout using the dispersion compensator. The use of the scanning objective lens facilitates the alignment of the system, because of its ability to focus the light beam. On the other hand, when using the dispersion compensator the focus ability on the reference arm disappears, and because of that the system alignment can take many hours. Beyond the alignment of both interferometer arms, it is also

extremely important to obtain perfectly alignment of the galvanometer mirrors, because it greatly affects the light reaching the sample. Thus, in order to perform the galvanometer mirror alignment, a red pointing laser was used as a guide. The galvo mirrors adjustment was made manually, which requires a careful and precise work to assure the most perfect alignment possible. It is important to stress that a perfect system alignment provides the maximum use of the light beam, minimizing power losses, which greatly improve the system performance parameters.

The overall system performance parameters achieved are not perfect yet. The system sensitivity is one of the greatest experimental achievements, once we were able to obtain a very high system sensitivity. The roll-off sensitivity is also very good, if compared to similar published systems, as already reported on previous sections. However, it is relevant to say that it can still be better, when the problem of dispersion imbalance is fixed, which will certainly increase the sensitivity for deeper positions, and consequently improve the roll-off sensitivity. On the other hand, the axial resolution is the worst performance parameter of the current setup. The dispersion imbalance between both arms of the interferometer needs to be fixed in order to achieve good axial resolution for deeper positions. On my personal opinion, dispersion compensation by software needs to be implemented as already mentioned above, since the use of a dispersion compensator has proven to fail.

This master thesis is based on the previous work made by other students so, it is important to verify the evolution achieved since I started to work on this project. Therefore, the following experiment results were performed by my colleague João Rodrigues, master student in biomedical engineering, before I started to work on this project.

Table 5: Table showing the system sensitivity results at the start and actual state of the project, with and without the neutral density filter.

Previous sensitivity	**Actual sensitivity without ND**	**Actual sensitivity with ND**
72.56 dB	76.13 dB	112.38 dB

In terms of the system sensitivity a great improvement is verified, which is mainly related to the measurement methodology. The use of the neutral density filter, allowed to correctly measure the system sensitivity. On the table 5, a comparison

between the previous and actual results are made, where it is visible the huge sensitivity improvement when a ND filter is used. For the results without the ND filter, it is also noticeable a slight increase on the system sensitivity, mainly due to the sample and reference arms scanning objective configurations.

On the figure 52, it is represented the roll-off results for the previous SS-OCT layout, where a roll-off of nearly $54dB/mm$ was verified.

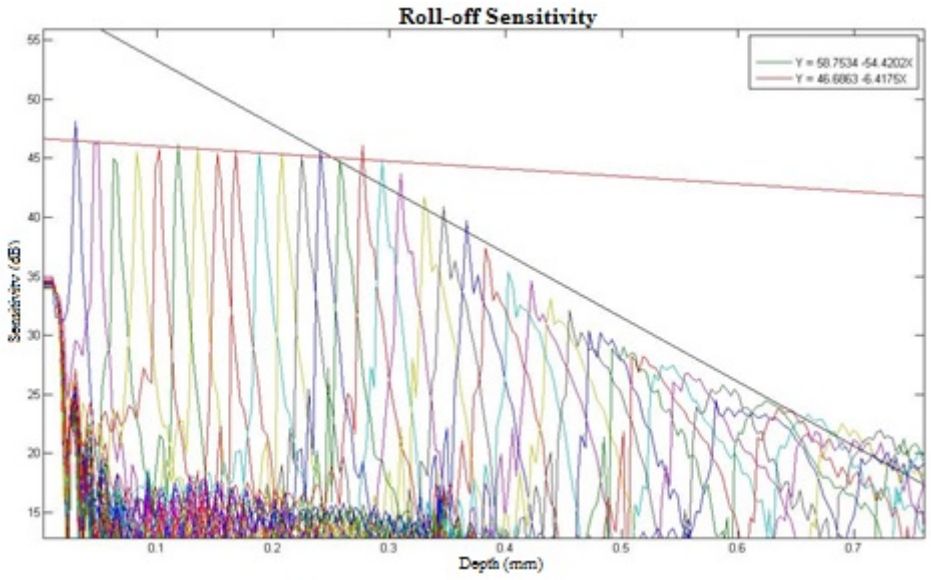

Figure 52: Roll-off sensitivity performance of the previous SS-OCT layout. Measurement made by João Rodrigues.

With the current setup, we achieved a huge improvement on the system roll-off sensitivity, obtaining a roll-off of nearly $2dB/mm$, which is an excellent achievement. This improvement result is due to the detector, the actual detector $PDB471C$ has a bandwidth of $400MHz$, when the previous detector was the Thorlabs Inc, $PDB145C$, which only has a bandwidth of $15MHz$. Thus, based on the following calculations, we were able to identify that the detector $PDB145C$ was cutting the interference signal, because its bandwidth was very limited, which was causing the sensitivity drop observed on figure 52.

The following equation describes the OCT system interference signal frequency at a specific depth [18]:

$$f = \frac{\Delta L}{\pi} \times \Delta k \times f_{sweep} \tag{41}$$

where, ΔL is the light path length difference between both interferometer arms, Δk is the light source spectral bandwidth and f_{sweep} is the swept frequency of the light source. Therefore, considering a depth range $\Delta L = 4mm$, a source swept frequency $f_{sweep} = 200kHz$ and $\Delta k = 2\pi\frac{\Delta\lambda}{\lambda_0^2}$, we are able to obtain an interference signal frequency of:

$$f4mm = \frac{4 \times 10^6}{\pi} \times 2\pi\frac{110}{1060^2} \times 200000 \simeq 157MHz \tag{42}$$

This result clearly shows that for imaging at $4mm$ depth, a balanced detector with bandwidth of at least $160MHz$ is required, and this is the reason why we changed the detector. Another evidence result, is the calculation of the depth range corresponding to an interference signal frequency of $15MHz$. Thus, using the equation 42, the depth range corresponding to a signal frequency of $15MHz$ is $\Delta L \simeq 0.38mm$, which can be compared to the result shown on figure 52, where a huge sensitivity drop is evident from this depth position.

In terms of the axial resolution, an improvement of nearly $1\mu m$ was observed when compared to the previous layout.

In conclusion, achieving better performance results is dependent of the correct dispersion balance between both arms of the interferometer.

Chapter 6

Zemax Optic Simulations

On this chapter, several optic simulations will be performed and discussed, in order to know if the available scanning objective lenses can be used to image the rat retina.

The simulations were made using the optical design program Zemax OpticStudio 15 Standard Edition, developed by Zemax, LLC. Zemax, is an optical design program that is used to design and analyze imaging systems. It works by ray tracing the propagation of rays through an optical system, modelling optical elements such as mirrors or lenses and providing several standard analysis diagrams.

At the beginning of this chapter a brief introduction to the schematic of the rat eye model is presented, including the final eye model developed on Zemax and utilized on the simulations. Furthermore, simulations of the three scanning objectives lenses used on the SS-OCT system are shown, where several comparisons are made regarding the best possible option and discussing problems of the current setup.

6.1 Schematic of the Rat's Eye

In medicine, the use of animals to test new treatments is quite common. Optical coherence tomography as a new technique to diagnosis and monitoring of treatment response, especially for eye diseases, is obviously an area of intense research. Therefore, the use of animals to conduct experiments is the following step.

In our case, there is interest in studying the eye retina of small animals like the rat. Despite being different, they are good models of the human eye. Once the project is at an early stage, the simulation of such procedures is very important to refine and improve the OCT system. Thereby, an optical model of the rat's eye was necessary. The schematic of the rat's eye adopted was the model published in 1978, by A. Hughes, on his work *A schematic eye for the rat* [35], where he demonstrates that previous models are not satisfactory for modelling a small eye and a new model is shown, which can be observed on figure 53.

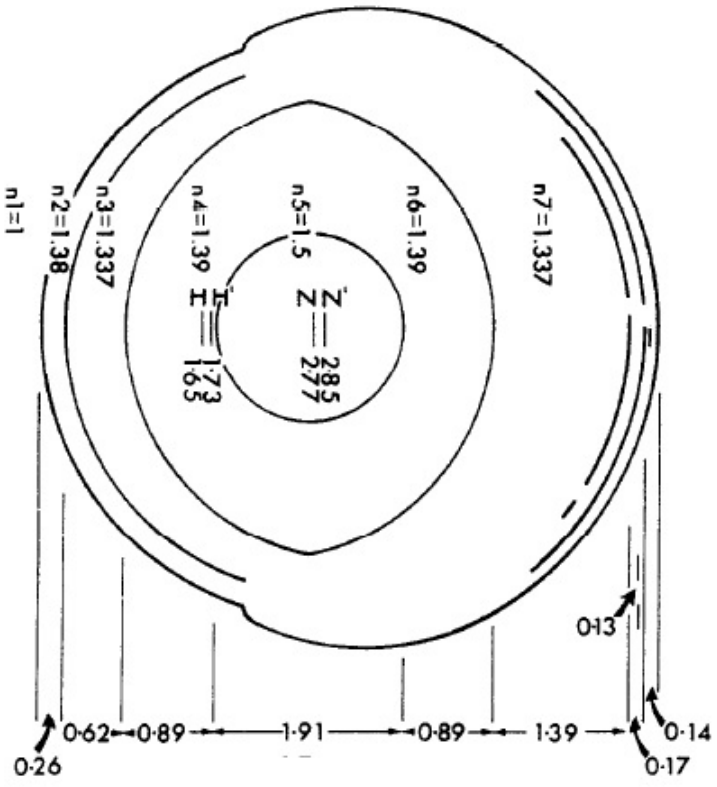

Figure 53: Schematic of the rat's eye and representation of the main parameters. The refractive index of each media is indicated by the letter n and the distance between layers is indicated bellow, in millimetres. Adapted from [35].

In order to design this eye model on Zemax, several parameters were needed, such as refractive index, distance between layers and radius of each surface. These parameters are expressed on the following tables.

Table 6: Rat average schematic eye index of refraction. Data found at [35].

Eye Media	**Index of Refraction**
Cornea	1.380
Aqueous and vitreous	1.337
Lens cortex	1.390
Equivalent core lens	1.500
Homogeneous lens	1.683
Retina	1.351

Table 7: Rat average schematic eye structure position and surface radius. Data found at [35].

Eye Structure	**Position (mm)**	**Radius (mm)**
Anterior cornea surface	0.000	2.965
Posterior cornea surface	0.260	2.705
Anterior lens surface	0.881	2.340
Anterior core surface	1.778	0.958
Posterior core surface	3.695	0.958
Posterior lens surface	4.591	2.340
Retina surface	5.981	-

With the data from the tables above, we were able to design a computational model of the rat's eye, on Zemax, whose illustration can be observed on figure 54.

The rat's eye has a length of $6.29mm$, measured by A. Hughes [35], however, our model only has a length of $5.982mm$. This difference is due to the presence of other layers after the retina, as outer limiting membrane or posterior scleral surface, and also the retina thickness of $0.17mm$. Once the primary objective is to image the rat's retina, this difference in length is not significant. On the designed model the retina is represented by a small spot with a few micrometers, which is perfectly acceptable once the retina height is much greater than the image spot.

Light entering the eye is limited by the entrance pupil diameter on the crystalline lens. Its diameter varies under certain conditions, but it can be specified on Zemax and is usually around $1mm$ for the rat [35].

However, the real problem when imaging the rat's retina is the significant spherical aberration. The rat lens is the largest contributor to the overall power of the eye, which results in negative aberration at the lens predominating over the positive aberration of the cornea. The total optical power (dioptre $D = 1 \setminus f$) of the rat's eye is $300.705D$, which is much greater when compared to the human eye optical power, $20D$ to $60D$ [35]. This is the main reason for the large spherical aberration of the rat's eye and the main problem at imaging the rat's retina with good quality.

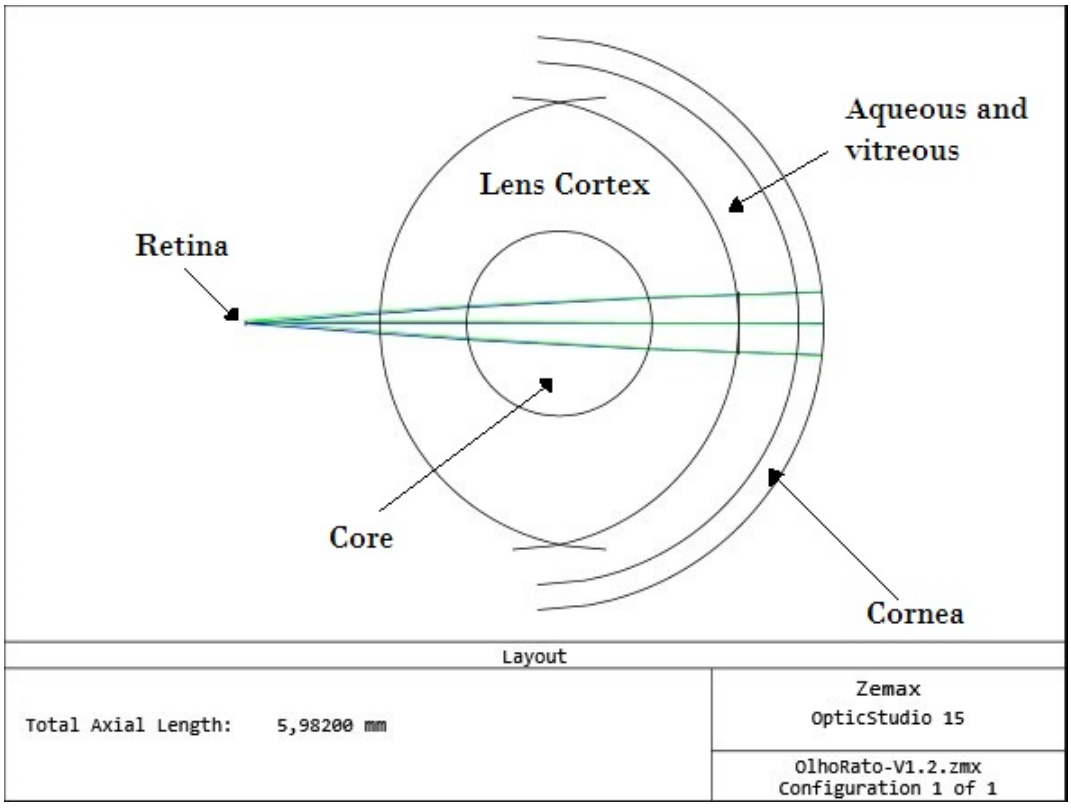

Figure 54: Rat's eye designed on Zemax with the data from tables 6 and 7.

6.2 Simulations and Analysis of Results

The following simulations were made to know if the three scanning objective lenses available could be used to image the rat's retina. The scanning objective

lenses used are the $LSM02-BB$, $LSM03-BB$ and $LSM04-BB$ from Thorlabs Inc., whose specifications can be found on chapter 4, section 4.1.6. The black box Zemax files of each objective lens was provided by Thorlabs Inc. [26].

These optical simulations only represent the sample arm of the swept source OCT system used on this master thesis. For each simulation of the sample arm, it is only considered the path from the galvanometer system to the sample. Thus, the collimated light beam reflected by the galvo mirror goes through the scanning objective lens, which focus the beam into the sample, or in this situation the rat's retina.

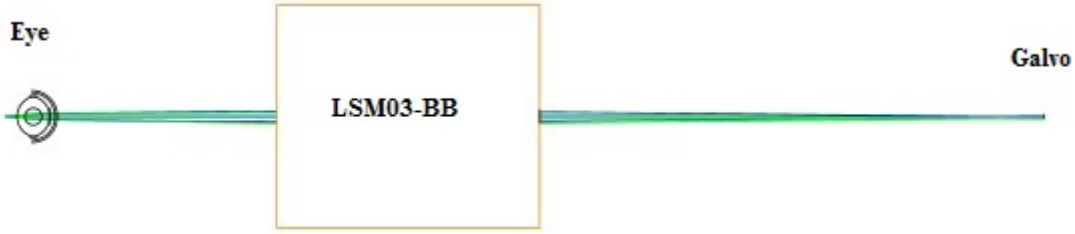

Figure 55: Illustration of an optical simulation layout, when is only used a scanning objective lens. Simulation made on Zemax OpticStudio 15.

On figure 55 is shown a simulation of the light path described. Note that in order to make sure that the image is formed on the rat's retina, the simulation layout was designed on the contrary of what was described above. Therefore, on the simulation layout, the object is the spot on the retina, and light leaving the eye goes through the objective lens, which directs the light onto the galvo mirror. However, as you can clearly observe, with this simple scheme it is impossible to focus the light at infinity, or in other words, collimate the light. Hence, additional elements are required on the system to enable the use of these objective lenses for imaging the rat's retina.

6.2.1 Objective Lens LSM02-BB Simulation

On figure 56, the simulation layout for the objective lens $LSM02-BB$ is shown. In order to observe collimated light exiting the scanning objective, it was necessary to introduce a convergent lens between the eye and the scanning objective. This lens is a Thorlabs $LB1092$, which is a bi-convex lens, with a focal length $f = 15.0mm$ and made of $N-BK7$ glass.

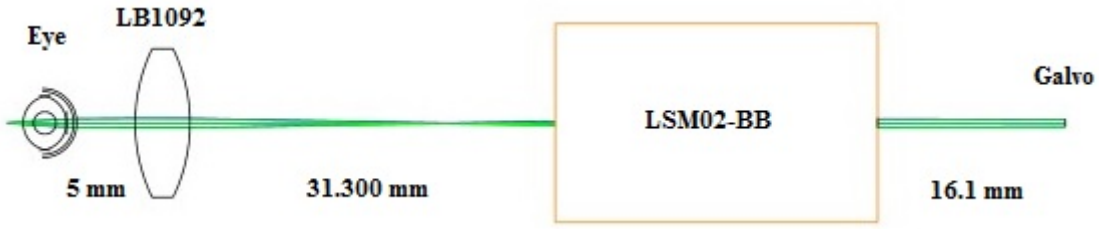

Figure 56: Optical simulation layout for the scanning objective lens $LSM02-BB$. Simulation made on Zemax OpticStudio 15.

All distances in the presented layout were carefully adjusted to obtain the best output and must be respected. However, the distance between the scanning objective and galvo mirror must be below the scanning distance of the scanning objective, which for $LSM02-BB$ is less than $16.1mm$.

The spot size on the eye, corresponds to the mean spot size of the respective objective lens, which is $11\mu m$ for $LSM02-BB$. Note that this value is a bit higher than the lateral resolution calculated for this objective, being the best prediction for the beam spot size on the retina.

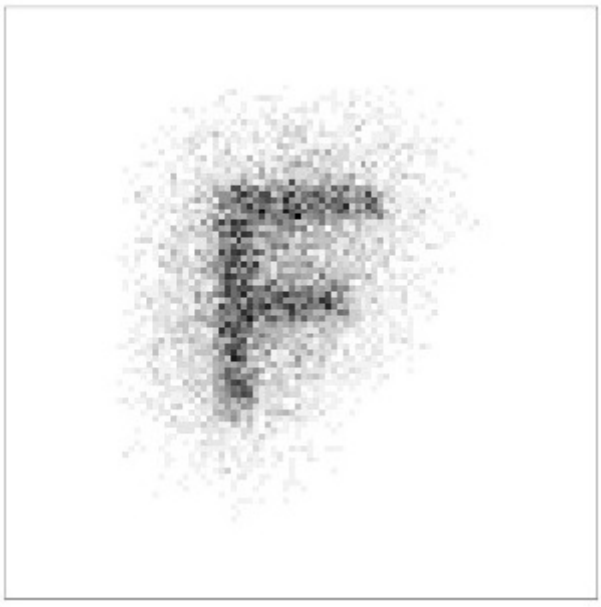

Figure 57: Image simulation for the scanning objective lens $LSM02-BB$, showing the consequences of spherical aberration. Results from Zemax OpticStudio 15.

The image simulation shown on figure 57, shows the effects of spherical aberration

on the final image. Thus, it is easy to recognize that the image is not perfect however, the "F" can still be identified, showing the possible use of this objective lens, with proper corrections, to image the rat's retina.

On figure 58, a Seidel diagram of the designed simulation is shown. A Seidel diagram shows the basic types of aberration on an optical system. As expected the main type of aberration present on our layout is spherical aberration. For the designed layout and analysing the Seidel diagram, we can confirm that the main sources of aberration are due to lens core and cornea. The maximum spherical aberration for this layout configuration is around $1.075\mu m$, which corresponds to 9.77% of an object size of $11\mu m$.

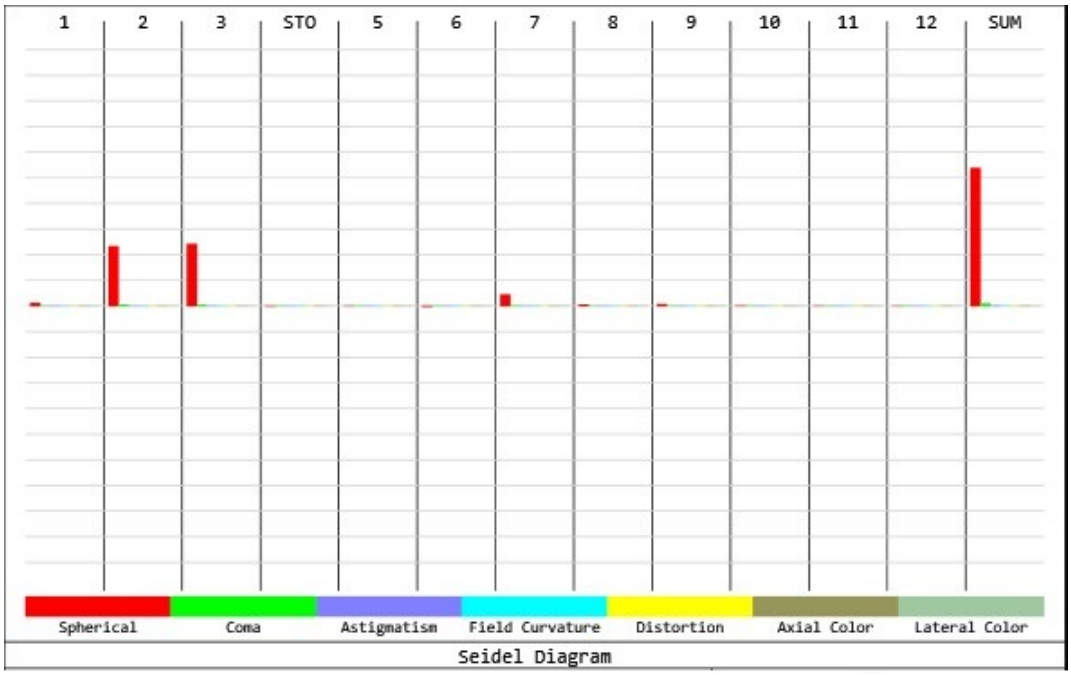

Figure 58: Seidel diagram for the scanning objective lens $LSM02-BB$ simulation, showing different aberration types present on the layout, where grid lines are spaced $0.2\mu m$. Results from Zemax OpticStudio 15.

6.2.2 Objective Lens LSM03-BB Simulation

The scanning objective lens $LSM03-BB$ received a special treatment since, it is the objective lens used by the current SS-OCT setup.

On figure 59 are shown the simulation layouts for the scanning objective lens

$LSM03 - BB$ with two different approaches. Different from the $LSM02 - BB$ layout, for $LSM03 - BB$ it is physically possible to use divergent lenses. Thus, both approaches produce basically the same result, obviously with some differences, as we will discuss. On figure 59a, the Thorlabs lens $LD2060$, which is a bi-concave lens, with a focal length $f = -15.0mm$ and made of $N - BK7$ glass, is used between the eye and the scanning objective. As we saw for $LSM02 - BB$, also for $LSM03 - BB$ the Thorlabs lens $LB1092$ was used, as we can observe on figure 59b.

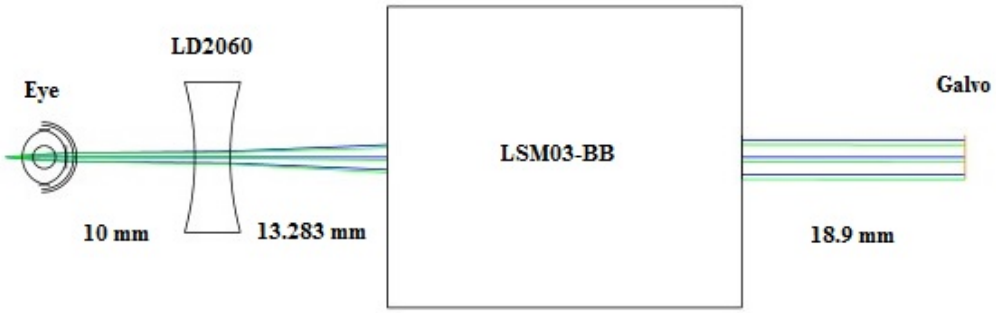

(a) Simulation layout using a divergent lens.

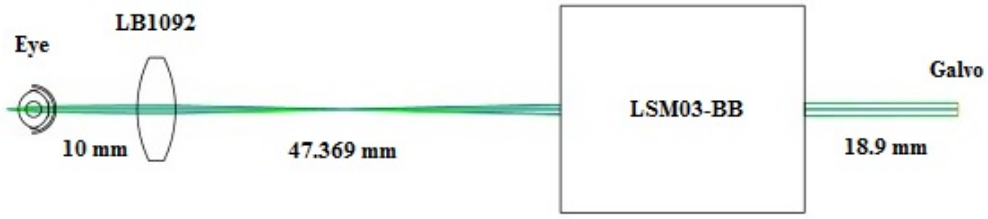

(b) Simulation layout using a convergent lens.

Figure 59: Optical simulation layout of the objective lens $LSM03 - BB$, using two different lenses, divergent on top and convergent on bottom. Simulation made on Zemax OpticStudio 15.

As already mentioned above, all distances on the layout, must be respected and the distance between the scanning objective and the galvo mirror must be bellow the scanning distance of the objective lens, which for $LSM03 - BB$ is less than $18.9mm$.

The spot size for these simulation layouts is $21\mu m$, which corresponds to the mean spot size of the respective scanning objective.

The image simulations shown on figure 60 reflect the effect of spherical aberration on the final image. However, it is easy to recognize that the image has imperfections. Once more, the "F" can still be identified, showing the potential use of this objective

lens to image the rat's retina.

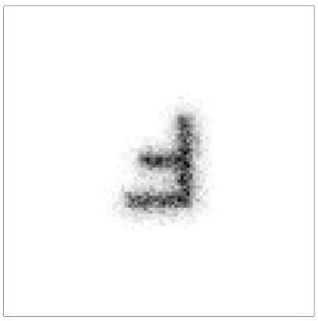

(a) Image simulation with divergent lens.

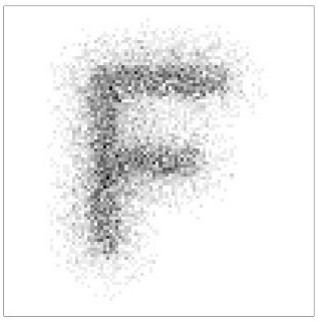

(b) Image simulation with convergent lens.

Figure 60: Image simulations for the scanning objective lens $LSM03-BB$, showing the consequences of spherical aberration for both approaches. Results from Zemax OpticStudio 15.

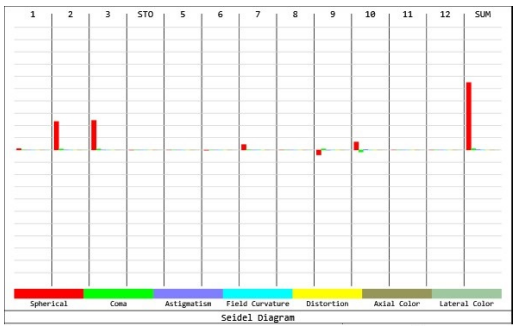

(a) Seidel diagram for the divergent lens layout.

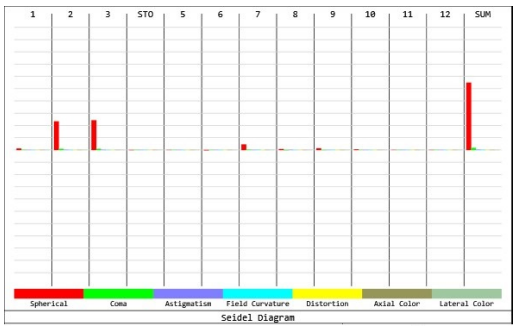

(b) Seidel diagram for the convergent lens layout.

Figure 61: Seidel diagrams for the scanning objective lens $LSM03-BB$ simulations, showing different aberration types present on each configuration layout, where grid lines are spaced $0.2\mu m$. Results from Zemax OpticStudio 15.

On figure 61, it is shown a Seidel diagram of the designed simulation. As expected, the main type of aberration present on our layout is spherical aberration. In terms of spherical aberration, the only difference between the two simulated approaches is on the divergent lens surface, as we can observe on figure 61a. It is visible a small amount of spherical aberration on surfaces 9 and 10, which are the surfaces of the lens. However, this aberration is cancelled, once one surface has positive aberration and the other negative spherical aberration. The configuration

using the divergent lens $LD2060$ has a maximum spherical aberration of $1.101\mu m$, while the configuration using the convergent lens $LB1092$ has a maximum spherical aberration of $1.097\mu m$. Considering an object size of $21\mu m$, the spheric aberration corresponds to 5.2% of its size.

The scanning objective lens $LSM03 - BB$ is the objective lens used on the sample arm of the SS-OCT system current setup. Therefore, the majority of the simulations made on Zemax, are related to the $LSM03 - BB$, where we tried to find a good configuration to image the rat's retina. Following this line of thinking, on table 8, are shown several simulation results for different simulated configurations of the scanning objective lens $LSM03 - BB$.

Table 8: Optical simulation results for the scanning objective lens $LSM03 - BB$, using several different configurations. f - focal length; X - simulated distance between the lens and the scanning objective.

Lens	**X (mm)**	**f (mm)**	**Spherical Aberration (μm)**
LA1116	37.275	+ 10	1.272
LA1540	46.159	+ 15	1.113
LA1074	62.780	+ 20	1.080
LB1157	37.973	+ 10	1.251
LB1092	47.369	+ 15	1.097
LB1014	87.389	+ 25	1.058
LC1054	7.732	- 25	1.073
LC1060	5.921	- 30	1.065
LD2060	13.283	- 15	1.101
LD2297	8.592	- 25	1.058
LD1357	1.161	- 50	1.050
LE5838-E	57.639	+ 20	1.107

As for the optical simulations shown of figure 59, we tried to use different lenses between the rat's eye and the scanning objective $LSM03 - BB$. Several types of lenses were simulated, including:palno-convex lenses (LAxx), bi-convex lenses (LBxx), plano-concave lenses (LCxx), bi-concave lenses (LDxx) and positive meniscus lenses (LExx). All the lenses tested are from Thorlabs Inc. For each simulated configuration, the following parameters were taken into account: the Thorlabs code

of the lens used, its focal length (f), the simulated distance between the lens and the scanning objective (X) and, finally, the total spherical aberration of the simulated configuration.

From the data present on table 8, we can conclude that positive lenses require longer distances (X) between the lens and the scanning objective than negative lenses, which is a positive factor, since distances below $10mm$ are difficult to achieve in practical situations. The spherical aberration results are very similar however, the best result was achieved for the lens $LB1014$, whose system spherical aberration was around 5% of the object size, which is still not good. Lenses with longer focal lengths, for instance $f = 50mm$, the optical system lose the ability to collimate the light exiting the objective lens, which does not allow to image the rat's retina.

6.2.3 Objective Lens LSM04-BB Simulation

On figure 62, the optical simulation layout for the objective lens $LSM04-BB$ is shown. As for the other simulated scanning objective lens, additional optic elements were required, in order to have collimated light exiting the scanning objective. Thus, a plano-concave Thorlabs lens, $LC1975$, with a focal length $f = -24mm$ and made of $N-BK7$ glass was used. All the distances in the present layout were maximized, to achieve the best possible final image, for this configuration.

The spot size on the rat's eye is, once more, related to the scanning objective lens. For the $LSM04-BB$ it corresponds to $29\mu m$, being the best possible prediction of the object size on the rat's retina.

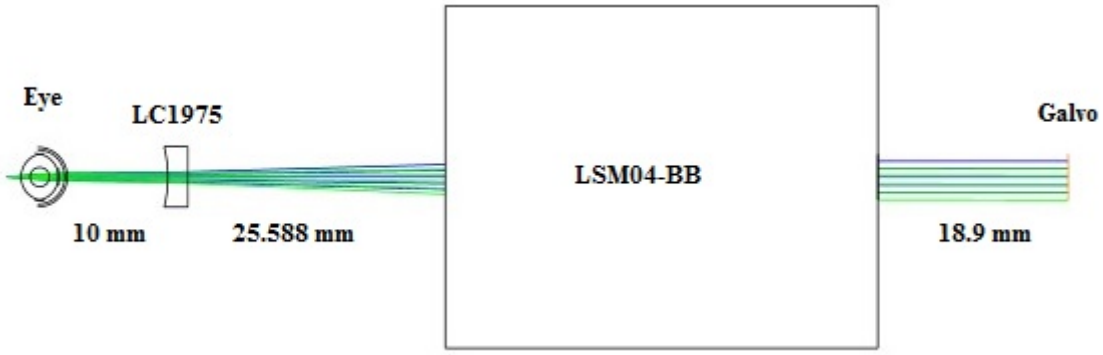

Figure 62: Optical simulation layout for the scanning objective lens $LSM04-BB$. Simulation made on Zemax OpticStudio 15.

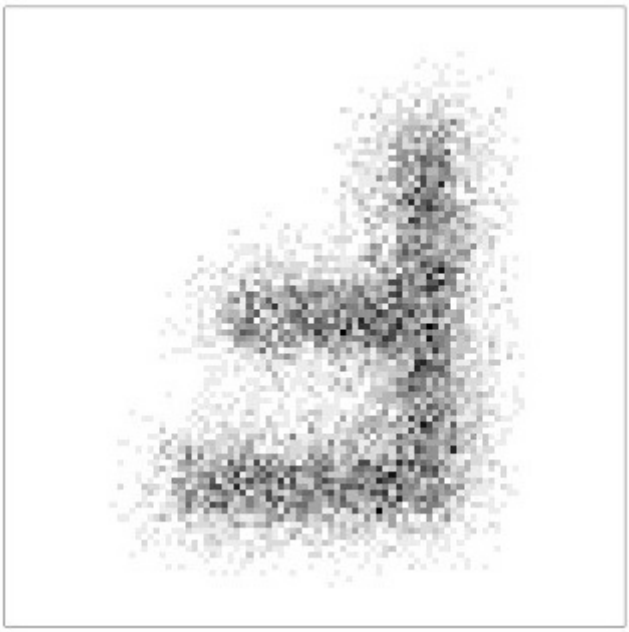

Figure 63: Image simulation for the scanning objective lens $LSM04-BB$, showing the consequences of spherical aberration. Results from Zemax OpticStudio 15.

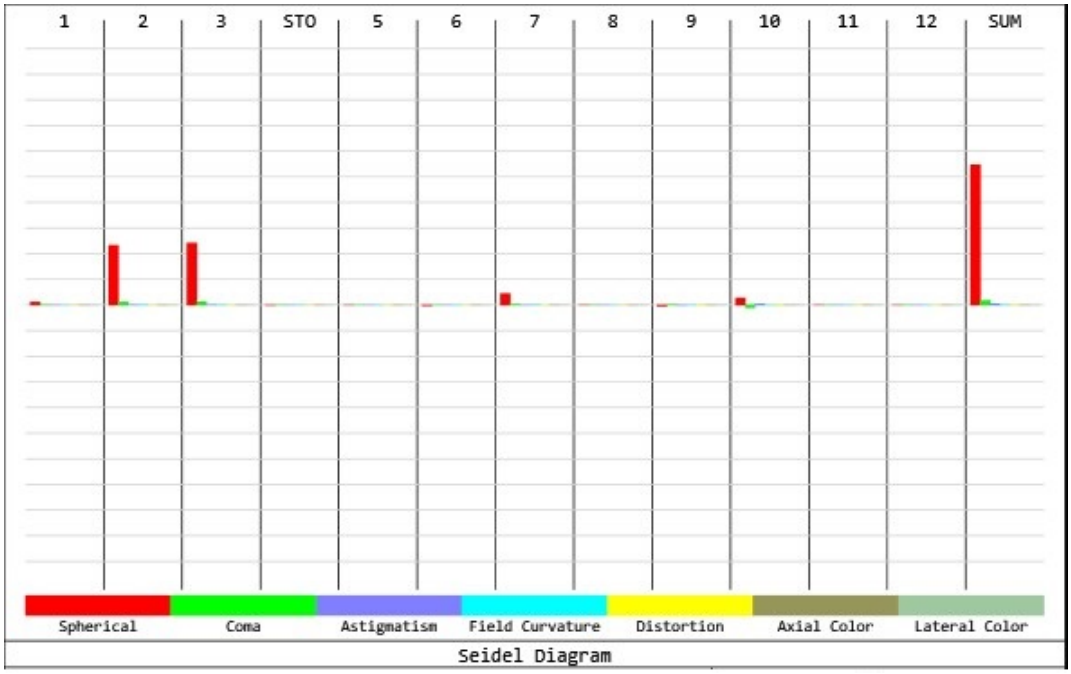

Figure 64: Seidel diagram for the scanning objective lens $LSM04-BB$ simulation, showing different aberration types present on the layout, where grid lines are spaced $0.2\mu m$. Results from Zemax OpticStudio 15.

The image simulation shown on figure 63 reflects the effect of spherical aberration on the simulated layout. Once more, according to this simulation, it is possible to image the rat's retina with this configuration. However, the image quality is not good and other optical improvements are required to achieve better image quality.

The Seidel diagram resulting of the optical simulation for the scanning objective lens $LSM04 - BB$ is shown on figure 64. For the configuration shown on figure 62, the main type of aberration is spherical, whose maximum aberration can go up to $1.094\mu m$. Considering an object size of $29\mu m$, a spherical aberration of 3.77% of the object size was obtained. Despite being the best result achieved in terms of spherical aberration, this scanning objective cannot be used on the SS-OCT system, because its performance parameters were below of the minimum requirements.

6.2.4 Discussion of Results

The primary objective of the Zemax optical simulations was achieved. It was proved that it is possible to image the rat's retina with the available scanning objective lenses for this project. Nevertheless, additional optical elements were required to achieve the desired result.

The simulation results show that low numerical aperture scanning objective lenses achieve better results, being the spherical aberration of the rat's eye the real problem of the optical system. Therefore, we focused our effort on the scanning objective lens, whose performance parameters were the best. Thus, the majority of the simulations were made for $LSM03 - BB$. Several simulations were made with only one additional lens between the objective lens and the eye. The results were not perfect, it was always observed an huge amount of spherical aberration, with some configurations achieving better results than others. We have tried to add multiple lenses, but these configurations proved to be difficult to obtain an image, once with multiple elements, the distances adjustment is much more complicated. For the performed simulations, it was shown that using convergent lenses with a focal length below $50mm$ resulted on better optical systems. Also, the use of convergent lenses allowed to work with longer distances (X), which could be a decisive factor on a real experimental setup.

In conclusion, despite the simulated scanning objective lenses being able to image the rat's retina, the image quality was degraded by the amount of spherical

aberration. Hence, other configurations or methods should be implemented, in order to correct the spherical aberration, allowing these objective lenses to image the rat's retina with better quality.

It is interesting to compare, the simulated results for a configuration using the rat's eye to other using the human eye. Both simulations were made for the scanning objective lens $LSM03-BB$, using the Thorlabs lens $LB1092$, as shown on figure 65.

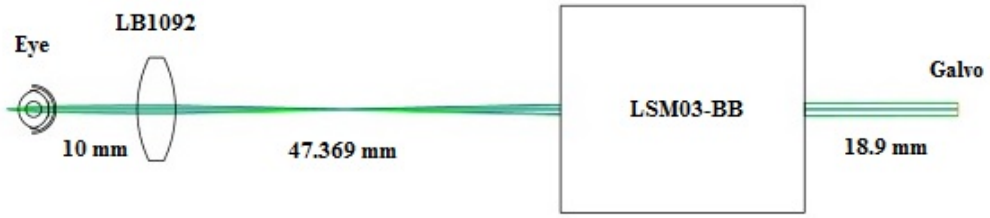

(a) Simulation layout for the rat's eye.

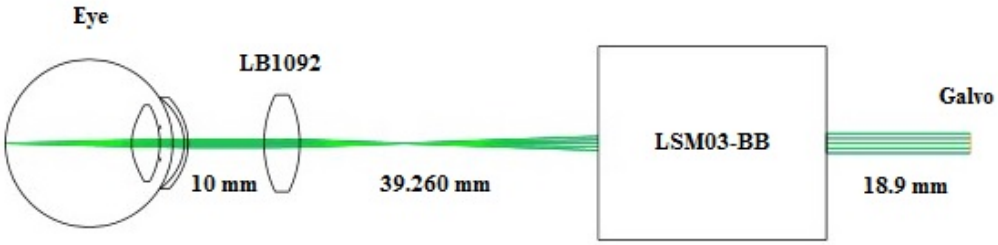

(b) Simulation layout for the human eye.

Figure 65: Optical simulation layout of the objective lens $LSM03-BB$, using the same lens $LB1092$, for rat's eye on top and for human eye on bottom. Simulation made on Zemax OpticStudio 15.

The image simulations shown on figure 66 are representative of the huge image quality difference between both experimental layouts. The simulated image resulting from the human eye configuration has much higher quality than the image on figure 66a. This difference is mainly due to the big discrepancy in terms of spherical aberration between the two layouts. While for the image on figure 66b, a maximum spherical aberration of $0.131\mu m$ was obtained, for figure 66a, the maximum spherical aberration was $1.097\mu m$, which is an amount eight times higher than for human eye. Hence, it is necessary to use appropriated optical elements for the rat's eye layouts, in order to cancel the high spherical aberration present on its eye.

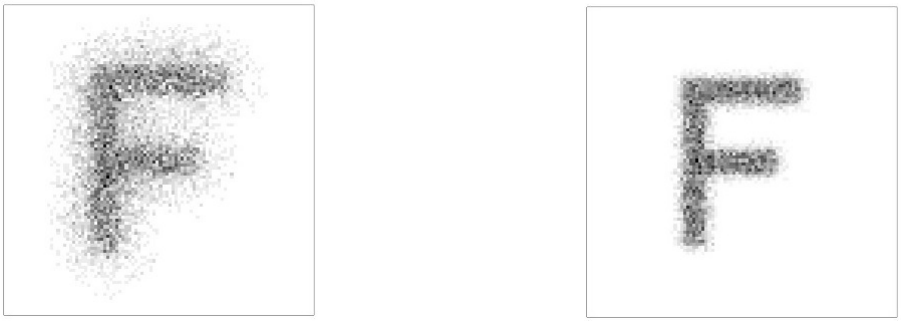

(a) Image simulation for the rat eye. **(b)** Image simulation for the human eye.

Figure 66: Image simulations for the rat and human eye, using a scanning objective lens $LSM03 - BB$. Results from Zemax OpticStudio 15.

One of the solutions, found on literature, to cancel the high spherical aberration of the rat's eye is the use of adaptive optics on the sample arm [32] [36] [37]. A schematic of an adaptive optics OCT system can be observed on figure 67, where it is clearly visible the huge amount of optical elements and the complexity of the system.

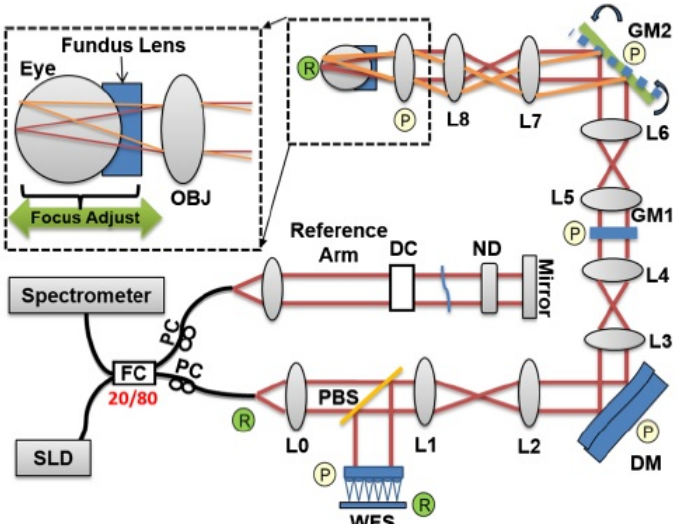

Figure 67: Schematic of an adaptive optics OCT system from [32].

However, with the inclusion of lots of optical elements, the dispersion compensation becomes even more important for the system performance. Therefore, other options must be explored, such as the use of aspheric lenses to compensate the spherical aberration.

Chapter 7

Conclusions

First, I am very pleased that at the end of my work, a visible progress has been achieved, regarding the initial state of the project.

This project was very challenging in many ways, being the first working experience, for me, on an engineering project of such importance.

The SS-OCT system performance parameters were the most important accomplishment of my work. A visible improvement of such parameters was achieved, particularly, the system sensitivity, roll-off performance and dynamic range.

The discovery of the correct procedure to measure the system sensitivity, led to a fantastic result, where a system sensitivity of $112dB$ was achieved. A substantial improvement was observed for the roll-off performance, whose R-number went down from $54dB/mm$ to $3dB/mm$, where the decisive factor was the balanced detector replacement. With the increased system sensitivity, also the dynamic range of our SS-OCT system improved. Finally, the axial resolution accomplished met the minimum requisites for an OCT application. However, the visible axial resolution degradation with increasing depth is a real issue and the dispersion imbalance observed is the cause of such problem.

Regarding the optical simulations, it was proven that the scanning objective lenses $LSM02-BB$, $LSM03-BB$ and $LSM04-BB$ are able to image the rat's retina. However, additional optical elements were included on the optical layout to enable its correct operation. The image quality achieved was far from being satisfactory, where the correction of the optical system spherical aberration will be the key to obtain better results.

The following steps to meet the final project goal are the balancing of the dispersion in both arms of the interferometer, in order to improve the system axial resolution, and to achieve a constant axial resolution over a wider depth range. There are two possible solutions that can be applied. First, the implementation of dispersion compensation by software, where signal phase shifts can be corrected [8], which is my personal recommendation, since it ensures greater adaptability to the system. Secondly, the inclusion of new elements on the OCT system, in order to balance the dispersion. However, we already tried to apply a dispersion compensator, which did not work. There is also the system alignment, which is much more difficult for this kind of solution.

Another step to be developed in future works is the continuation of the optical simulations on Zemax. I strongly advise the simulation of aspheric lenses instead of the lenses used on my simulations. However, would be very interesting to image the rat's retina for the current SS-OCT setup, applying one of my best simulations. It should be possible to obtain an image, besides its predictable poor quality. As a last resource option, adaptive optics could be implemented, but I would strongly advise against this option, since the system complexity would greatly increase.

At last, I think all the objectives proposed for this master thesis were accomplished.

Bibliography

[1] Eugene Hecht, **Óptica**, Fundação Calouste Gulbenkian, 3º edição, (2012).

[2] Wojtkowski, M., Leitgeb, R., Kowalczyk, A., Bajraszewski, T., Fercher, A. F., **In vivo human retinal imaging by Fourier domain optical coherence tomography.** Journal of Biomedical Optics, 7(3), 457–463, (2002).

[3] Brezinski, M., **Optical Coherence Tomography Principles and Applications.** Academic Press, 1st edition, (2006).

[4] Duguay, M. a, et al., **Ultrahigh speed photography of picosecond light pulses and echoes**, Applied Optics, 10(9), 2162–2170, (1971).

[5] Fujimoto, J.G. et al., **Femtosecond optical ranging in biological systems**, Optics letters, 11(3), p.150, (1986).

[6] Huang, D. et al., **Optical coherence tomography. Science**, 254(5035), pp.1178–1181, (1991).

[7] Fercher, a F., Mengedoht, K., Werner, W., **Eye-length measurement by interferometry with partially coherent light**, Optics letters, 13(3), pp.186–188, (1988).

[8] Fujimoto, J.G., Drexler, W., **Optical Coherence Tomography - Technology and Applications**, Springer.

[9] Tomlins, P.H., Wang, R.K., **Theory, developments and applications of optical coherence tomography**, Journal of Physics D: Applied Physics, 38(15), pp.2519–2535, (2005).

[10] Drexler, W., Liu, M., Kumar, A., Kamali, T., Unterhuber, A., Leitgeb, R. a., **Optical coherence tomography today: speed, contrast, and multimodality.** Journal of Biomedical Optics, 19(7), 71412, (2014).

[11] Marschall, S., Sander, B., Mogensen, M., Jørgensen, T. M., Andersen, P. E., **Optical coherence tomography-current technology and applications in clinical and biomedical research**, Analytical and Bioanalytical Chemistry, 400(9), 2699–2720, (2011).

[12] Chinn, S. R., Swanson, E. a, Fujimoto, J. G., **Optical coherence tomography using a frequency-tunable optical source.** Optics Letters, 22(5), 340–342, (1997).

[13] Wojtkowski, M., **High-speed optical coherence tomography: basics and applications**, Applied optics, 49(16), pp.D30–D61, (2010).

[14] Popescu, D. P., Choo-Smith, L. P. I., Flueraru, C., Mao, Y., Chang, S., Disano, J., Sowa, M. G., **Optical coherence tomography: Fundamental principles, instrumental designs and biomedical applications.** Biophysical Reviews, 3(3), 155–169, (2011).

[15] Choma, M. A., Sarunic, M. V, Yang, C., Izatt, J. A., **Sensitivity advantage of swept source and Fourier domain optical coherence tomography.** 11(18), 2183–2189, (2003).

[16] Podoleanu, a G., **Optical coherence tomography.** The British Journal of Radiology, 78(935), 976–988, (2005).

[17] Potsaid, B., Baumann, B., Huang, D., Barry, S., Cable, A. E., Schuman, J. S., Fujimoto, J. G., **Ultrahigh speed 1050nm swept source/Fourier domain OCT retinal and anterior segment imaging at 100,000 to 400,000 axial scans per second.** Optics Express, 18(19), 20029–20048, (2010).

[18] Bouma, B., Tearney, G., **Handbook of optical coherence tomography.** CRC Press, 1st edition, (2001).

[19] Huber, R., Wojtkowski, M., Fujimoto, J. G., Jiang, J. Y., Cable, a E., **Three-dimensional and C-mode OCT imaging with a compact, frequency**

swept laser source at 1300 nm. Optics Express, 13(26), 10523–10538, (2005).

[20] Wieser, W., Biedermann, B. R., Klein, T., Eigenwillig, C. M., Huber, R., **Multi-megahertz OCT: High quality 3D imaging at 20 million A-scans and 4.5 GVoxels per second.** Optics Express, 18(14), 14685–14704, (2010).

[21] Potsaid, B., Gorczynska, I., Srinivasan, V. J., Chen, Y., Liu, J., Jiang, J., Fujimoto, J. G., **Ultrahigh speed spectral/Fourier domain ophthalmic OCT.** Society of Photo-optical Instrumentation Engineers, 716307–716307–12, (2009).

[22] Drexler, W., Fujimoto, J. G., **State-of-the-art retinal optical coherence tomography.** Progress in Retinal and Eye Research, 27(1), 45–88, (2008).

[23] Shin, S., Sharma, U., Tu, H., Jung, W., Boppart, S. A., **Characterization and Analysis of Relative Intensity Noise in Broadband Optical Sources for Optical Coherence Tomography.** IEEE Photonics Technology Letters : A Publication of the IEEE Laser and Electro-Optics Society, 22(14), 1057–1059, (2010).

[24] **Axsun OCT Swept Source Engine Operators' Manual** (Rev. 09). Axsun Technologies, Inc., Massachusetts , USA, (2010).

[25] Tsai, T.-H., Zhou, C., Adler, D., Fujimoto, J. G., **Frequency Comb Swept Lasers for Optical Coherence Tomography.** Ooher, 75541E–75541E–10, (2010).

[26] Thorlabs Inc. https://www.thorlabs.de/
Online at 7 August 2015.

[27] **Balanced Amplified Photodetectors - PDB47xC - Operation Manual** (Version 1.1). Thorlabs, Inc., (2014).

[28] **Scanning Galvo Systems - User Guide**. Thorlabs,Inc.

[29] **X5-400M User's Manual** (Rev. 1.01). Innovative Integration, California, USA, (2011).

[30] **NI 6010 Specifications**. National Instruments Corporation, (2005).

[31] Grulkowski, I., Gora, M., Szkulmowski, M., Gorczynska, I., Szlag, D., Marcos, S., Wojtkowski, M., **Anterior segment imaging with Spectral OCT system using a high-speed CMOS camera**. Optics Express, 17(6), 4842–4858, (2009).

[32] Jian, Y., Zawadzki, R. J., Sarunic, M. V., **Adaptive optics optical coherence tomography for in vivo mouse retinal imaging**. Journal of Biomedical Optics, 18(5), 56007, (2013).

[33] The MathWorks, Inc.
http://www.mathworks.com/matlabcentral/fileexchange/33775-lorentzfit-x-y-varargin-
Online at 12 August 2015.

[34] The MathWorks, Inc.
http://www.mathworks.com/matlabcentral/fileexchange/10590-fwhm/content/fwhm.m
Online at 12 August 2015.

[35] Hughes, A., **A schematic eye for the rat.** Vision Research, 19(5), 569–588, (1979).

[36] Fernández, E. J., Považay, B., Hermann, B., Unterhuber, A., Sattmann, H., Prieto, P. M., Drexler, W., **Three-dimensional adaptive optics ultrahigh-resolution optical coherence tomography using a liquid crystal spatial light modulator.** Vision Research, 45(28), 3432–3444, (2015).

[37] Hermann, B., Fernández, E. J., Unterhuber, a, Sattmann, H., Fercher, a F., Drexler, W., Artal, P., **Adaptive-optics ultrahigh-resolution optical coherence tomography.** Optics Letters, 29(18), 2142–2144, (2004).